MECHANICAL PROPERTY DETERMINATION FOR FLEXIBLE MATERIAL SYSTEMS

A Thesis
Presented to
The Academic Faculty

by

Jeremy Lee Hill

In Partial Fulfillment
of the Requirements for the Degree
Doctor of Philosophy in the
Daniel Guggenheim School of Aerospace Engineering

Georgia Institute of Technology
May 2016

MECHANICAL PROPERTY DETERMINATION FOR FLEXIBLE MATERIAL SYSTEMS

Approved by:

Dr. Robert D. Braun, Advisor
Daniel Guggenheim School of
Aerospace Engineering
Georgia Institute of Technology

Dr. Julian J. Rimoli
Daniel Guggenheim School of
Aerospace Engineering
Georgia Institute of Technology

Dr. Graeme J. Kennedy
Daniel Guggenheim School of
Aerospace Engineering
Georgia Institute of Technology

Dr. Christopher L. Tanner
Entry, Descent, and Landing and
Formulation Group
NASA Jet Propulsion Laboratory

Dr. Anthony M. Calomino
Atmospheric Flight and Entry
Systems Branch
NASA Langley Research Center

Date Approved: 16 March 2016

ACKNOWLEDGEMENTS

I have been fortunate in life to be surrounded by individuals who provide unlimited amounts of support and encouragement. Without those individuals, this work may have not come to fruition. I would first like to thank my advisor, Robert Braun, for providing constructive criticisms and insightful comments at different stages of my research. He taught me to focus my ideas and to convey the broader context of my work. His leadership and dedication will continue to inspire me in the future. I would also like to thank Ian Clark for guiding my early graduate work during his two years at Georgia Tech as a visiting professor. I wish to thank the other members of my committee, Anthony Calomino, Christopher Tanner, Graeme Kennedy, and Julian Rimoli whose guidance have been invaluable and greatly appreciated.

This research was completed with the assistance of multiple individuals throughout the aerospace community both in person during summer internships and remotely during my time on the Georgia Tech campus. I am very grateful to Joe Welch and Ben Tutt for all I learned from them regarding finite element analysis and for their time to discuss aspects of my research.

This work is possible because of the exceptional graduate level education I received at Georgia Tech. I am grateful to the faculty and staff of the Daniel Guggenheim School of Aerospace Engineering for that. My colleagues in the Space Systems Design Laboratory, who provided a great deal of entertainment and support during the countless hours in the lab, also deserve my thanks for their valuable thoughts and feedback.

I thank my parents, Patrick and Sherry, for their love and sacrifice throughout my life. From them, I gained a relentless drive and refusal to quit when times are hard. I

am very grateful to my brothers, Dino and PJ, for their love and friendship. Finally, and most importantly, I would like to thank my wife, Lindsey, and son, Noah, for being supportive and understanding of the long hours and weekends spent working on this manuscript. My wife's encouragement and unwavering love were undeniably the bedrock upon which the past several years of my life have been built.

TABLE OF CONTENTS

LIST OF TABLES

LIST OF FIGURES

NOMENCLATURE

Abbreviations

ANOVA Analysis of Variance

CFD   Computational Fluid Dynamics

DGB   Disk-Gap-Band

DOE   Design of Experiments

DOF   Degrees of Freedom

EDL   Entry, Descent, and Landing

EPI   Ends Per Inch

FEA   Finite Element Analysis

FSI   Fluid-Structure Interaction

GSA   Global Sensitivity Analysis

HIAD   Hypersonic Inflatable Aerodynamic Decelerator

IAD   Inflatable Aerodynamic Decelerator

IRVE   Inflatable Reentry Vehicle Experiment

LaRC   Langley Research Center

LDSD   Low Density Supersonic Decelerator

LSR   Least Squares Residual

ME   Margin of Error

MSE	Mean Square Error
MSMM	Materials, Structures, Mechanical Systems, and Manufacturing
PAIDAE	Program to Advance Inflatable-Decelerators for Atmospheric Entry
PBC	Periodic Boundary Conditions
PKII	2nd Piola-Kirchhoff
PPI	Picks Per Inch
PSE	Pseudo Standard Error
RMS	Root Mean Square
SIAD	Supersonic Inflatable Aerodynamic Decelerator
SRSM	Sequential Response Surface Methodology
STR	Space Technology Roadmap
TA	Technology Area
TPI	Threads Per Inch
YDR	Yarn Density Ratio

Subscripts

f	weft or fill
k	Subcell
N	Iso-Strain Components
S	Iso-Stress Components
w	warp

Symbols

β	Undulation Angle
δ	Displacement
$\Delta\phi$	Infinitesimal Twist Angle
Δx	Infinitesimal Cylinder Length
ϵ	Cauchy Strain
γ	Engineering Shear Strain
λ	Stretch Ratio
μ	Discount Factor
ν	Poisson's Ratio
ϕ	Frame Half Angle
σ	Cauchy Stress
$\mathbf{F}$	Deformation Gradient
$\mathbf{T}$	Strain Transformation Matrix
θ	Braid Angle
$\vec{q}$	Unit Direction Vector
C	Crimp Ratio
D	Yarn Diameter
D_R	Reorientation Damping Coefficient
E	Elastic Modulus

E_f	Fabric Elastic Modulus
E_{total}	Total Structure Energy
EI	Bending Stiffness
G	Shear Modulus
H	Hysteresis Parameter
h	Crimp Height
I	Area Moment of Inertia
J	Polar Moment of Intertia
l	Yarn Length
m	Mass
M_w	Wrinkling Moment
P	Absolute Pressure
p	Yarn Spacing
R	Air Gas Constant
r	Cylinder Radius
RL	Reloading Parameter
T	Applied Torque
T	Temperature
t	Thickness
U_f	Total Fabric Strain Energy

V Volume

W_{air} Work Done by Air Compression

W_{ext} Work Done by External Forces

L_{fabric} Length of Fabric in Yarn Direction

L_{yarn} Length of Extracted and Straightened Yarn

$\mathbf{C}$ Stiffness Matrix

SUMMARY

Inflatable Aerodynamic Decelerators (IADs) are a candidate technology NASA began investigating in the late 1960s. Compared to supersonic parachutes, IADs represent a decelerator option capable of operating at higher Mach numbers and dynamic pressures. IADs have seen a resurgence in interest from the Entry, Descent, and Landing (EDL) community in recent years. The 2015 NASA Space Technology Roadmap (STR) highlights EDL systems, as well as, Materials, Structures, Mechanical Systems, and Manufacturing (MSMM) as key Technology Areas for development in the future; recognizing deployable decelerators, flexible material systems, and computational design of materials as essential disciplines for development. This investigation develops a multi-scale flexible material modeling approach that enables efficient high-fidelity IAD design and a critical understanding of the new materials required for robust and cost effective qualification methods. The approach combines understanding of the fabric architecture, analytical modeling, numerical simulations, and experimental data. This work identifies a simple and fast method for determining IAD material characteristics while not utilizing complicated or expensive research equipment. This investigation also recontextualizes an existing mesomechanical model through validation for structures pertaining to the analysis of IADs. In addition, corroboration and elaboration of this model is carried out by evaluating the effects of varying input parameters. Finally, the present investigation presents a novel method for numerically determining mechanical properties. A sub-scale section that captures the periodic pattern in the material (unit cell) is built. With the unit cell, various numerical tests are performed. The effective nonlinear mechanical stiffness matrix is obtained as a

function of elemental strains through correlating the unit cell force-displacement results with a four node membrane element of the same size. Numerically determined properties are validated for relevant structures. Optical microscopy is used to capture the undeformed geometry of the individual yarns.

CHAPTER I

LITERATURE REVIEW AND MOTIVATION

1.1   Background

Future Mars missions will require the landing of more massive payloads on the surface. As vehicles grow in mass, it becomes more difficult to dissipate all the kinetic energy necessary to meet desired end conditions. Currently, the operating Mach numbers and dynamic pressures of Mars supersonic parachutes limit the available payload mass and thereby constrain future mission design. Inflatable Aerodynamic Decelerators (IADs) are a candidate technology NASA began investigating in the late 1960s. Compared to supersonic parachutes, IADs are capable of operating at higher Mach numbers and dynamic pressures [1]. IADs have seen a resurgence in interest from the Entry, Descent, and Landing (EDL) community in recent years [2]. Technology investments in the last decade have significantly advanced three IAD design classes: attached isotensoid, tension cone, and stacked toroid [3, 4, 5].

Materials are enabling or critical technologies for most aerospace vehicle systems. Material properties and capabilities provide the form and function to structures, sensors, thermal, and many other systems. Vehicle mass is always of importance, and thus materials need to have the desired functionality coupled with low overall mass. Developing materials with improved properties directly aimed at upcoming mission needs is critical to the success of future missions.

Flexible materials allow large systems to be stored in minimal space and deployed or inflated as needed. Such systems have challenges with stowage and deployment strategies, material properties, damage resistance, and mass. The focus of flexible material systems research is the identification of soft goods or flexible systems that

enable the assembly of expandable structures from a small volume to a larger volume through the combined use of rigid linkages and joints with soft thin shells or membranes. The objective of this technology is to offer an increased volume, lower mass solution than rigid metal or composite structures through a reliance on the ability to minimize weight and stowed volume without sacrificing operational functionality and reliability. Technology solutions require low-density flexible materials for efficient stowage with deployed systems possessing high strength and stiffness for applications ranging from satellite booms and solar arrays to the construction of temporary shelters and inflatable thermal protection systems.

Design and certification methods are necessary for development of any structural system. The current development approach to design and certify flexible material systems is based on a building block sequence of structural components from very small material coupon samples to large, full scale assemblies or components. The structural response and failure modes are interrogated at each scale to provide a statistically significant data set for design and certification. This is a highly empirical, heritage approach with basis in early aircraft design. However, from a time or economic point of view, this approach not well suited to space hardware requiring only a few replicate production runs.

The NASA Space Technology Roadmap (STR) highlights EDL systems, as well as, Materials, Structures, Mechanical Systems, and Manufacturing (MSMM) as key Technology Areas (TAs) for development in the future; recognizing deployable decelerators, flexible material systems, and computational design of materials as essential disciplines for development [6, 7]. New techniques for the computational design of flexible material systems used on deployable decelerators address multiple capabilities in TA09 and TA12 of the STR.

1.2 Inflatable Aerodynamic Decelerators

1.2.1 Tested Configurations

While only a few IADs have been flight tested, several geometries have been tested in wind tunnels and even more have been analyzed as part of system studies. Smith et al describes the development history of the IAD from the 1960s to 2010 [8]. Many IAD configurations have been studied, but recent technology investments in the Isotensoid, Tension Cone, and Stacked Toroid configurations have progressed the understanding of these three configurations far beyond others. As a result, these IADs have the highest probability of being utilized in future missions and discussion in the following sections is limited to these three configurations.

1.2.1.1 Isotensoid

In 1964, Houtz presented a decelerator design with uniaxially loaded meridional cords encompassing a biaxially-stressed envelope [9]. The theory behind the Isotensoid design provides for equal stresses in principal directions of the envelope, as well as, being constant across the surface in the absense of aerodynamic loads. In addition, tensile loads in the cords are constant along their length. These properties hold except near discontinuities created by inlets and other structures. In reality, additional lobing on the envelope is created in between the cords due to the orthotropic material properties that causes stress deviations from the developed theory. An analytic expression for stresses in a lobed isotensoid as a function of the design stress, internal pressure, number of gores, and material bias was presented by Barton [10]. Static structural tests of 1.5m isotensoid models included shape verification, inflation, and material strength testing. From those tests, the limitations of using linear theory are seen in lower than predicted experimental loads [10, 11, 12].

1.2.1.2 Tension Cone

In 1965, Anderson presented a decelerator design with a surface of revolution that exhibits only tensile stresses in both principle directions (tension shell) and a hooped shaped support that carries compressive loads [13]. An inflated torus is usually incorporated as the support member for the tension shell. Required internal pressure, minor diameter, and material properties are determined from buckling loads using linear membrane theory [14]. Limitations in fabrication techniques have generally driven the tension shell and torus be created in multiple segments. The resulting non-circular shape differs from the ideal. As a result, a different state of stress occurs in both the shell and torus. While static structural tests on both the continuous and segmented tension cone design have not been conducted, wind tunnel data has been gathered for validation and verification purposes [15]. The use of advanced fabrication techniques and materials have potential to decrease required inflation pressure, and therefore mass, beyond that of linear predictions [16].

1.2.1.3 Stacked Toroid

The Stacked Toroid configuration is typically created by stacking a series of concentric toroidal members (connected by load bearing straps) and wrapping them with a cover, potentially also serving as the thermal protection system (TPS) [17]. While the aerodynamic pressure distribution is not directly used to design the shape of the stacked toroid, aerodynamic loads still affect required inflation pressures, material properties, and thus system mass. Compared to the Tension Cone and Isotensoid designs, the stacked toroid is usually a more complicated system to analyze with a higher mass. The complexity of the Stacked Toroid (e.g. variable boundary conditions, uneven strap loading, load sharing among tori, etc.) makes it difficult to analyze analytically; often requiring numerical or empirical models [18, 19]. As an example, the IRVE-3 toroids consist of a urethane bladder, a Kevlar® braided tube

coated with urethane, radial straps, and axial cords adhered within the braid [20].

1.2.2 Development History

NASA Langley Research Center (LaRC) first proposed the use of inflatable reentry vehicles in the 1960s [21]. During the Viking, Pioneer Venus, and Galileo mission planning phases of the 1970s, IADs were considered. At the same time, the Disk-Gap-Band (DGB) parachute was being developed as a deployable decelerator. IADs were shown to be capable of operating at Mach numbers and dynamic pressures at which the DGB exhibited undesirable behaviors. However, the Viking mission did not require decelerator deployment outside of the DGBs performance capabilities [22]. As a result, IAD development was halted in the late 1970s, leaving many issues unaddressed.

Interest in IADs has renewed in recent years and led to substantial technology investments. The Program to Advance Inflatable-Decelerators for Atmospheric Entry (PAIDAE) brought attention to hypersonic IAD technology with a successful flight test of the Inflatable Reentry Vehicle Experiment (IRVE) stacked toroid IAD in 2009 [23]. In the supersonic regime, viable IAD geometries and materials were also assessed. NASA LaRC, ILC Dover Inc., and the Georgia Institute of Technology carried out a series of wind tunnel tests to explore aerodynamic and structural performance characteristics of two different supersonic IAD configurations. Clark performed conceptual studies, wind tunnel testing, and computational aerodynamic analyses to advance the state of supersonic tension cone IAD [14]. The inflatable tension cone model is shown in Figure 1.

Tanner performed subsonic and transonic wind tunnel tests using attached isotensoid and tension cone models. In addition, Tanner developed a Fluid-Structure Interaction (FSI) framework for the static aeroelastic analysis of IADs [15]. The Hypersonic Inflatable Aerodynamic Decelerator (HIAD) and Low Density Supersonic
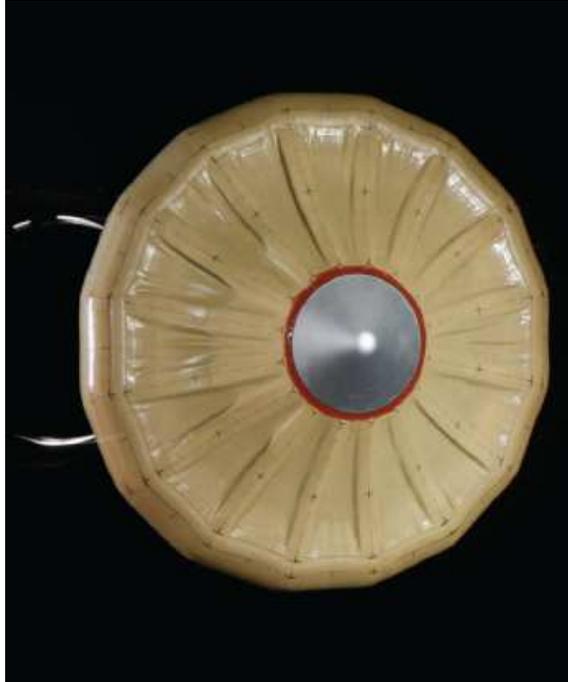
Figure 1: Inflatable Tension Cone Model (Front View) [15]

Decelerator (LDSD) Programs conducted ground and flight tests to develop design, analysis, manufacturing, and assembly techniques for IADs [3, 5].

1.2.3 Structural Analysis and Testing

When designing an IAD, it is often difficult to create a shape that is simultaneously loaded in tension in both principle directions. Wrinkling in a membrane will be initiated as soon as in-plane tension is lost (or in other words, the lowest principle in-plane stress becomes zero). At this condition, unpredictable behavior is introduced that can create stress concentrations and undesirable aerodynamic performance. Linear theory has thus been used in the design of IADs to determine the shape necessary to maintain a tensile load state under a known aerodynamic load [2].

In the 1960s, it was necessary to design and analyze IADs using analytical theories; however, scientific computing has enabled Finite Element Analysis (FEA) of large complex structures and Computational Fluid Dynamics (CFD) analysis of flow

fields around rigid bodies. FSI frameworks couple FEA and CFD together to investigate how a flow field will change a structure and visa-versa. Rohrschneider, Tanner, and others have coupled two independent FEA and CFD codes together to analyze IADs [15, 24]. Currently, FSI analysis suffers from long run times and lack of quantitative validation data. Tanner's validation efforts relied on qualitative comparisons against images obtained during wind tunnel testing. As IAD development continues, more emphasis is being placed on in-situ measurement of displacements and forces. Typical strain measurement techniques such as strain gauges locally stiffen the inflatable structures; thus non-invasive techniques, like photogrammetry, show promise for acquiring validation data. Only recently have these techniques been used in IAD wind tunnel experiments [5].

Flight like loading conditions are desirable for structural testing of IADs; however, the cost of flight testing limits its use. Aerodynamically deformed shapes can be achieved inside wind tunnels but, in the case a Mars environment, proper test conditions will be difficult to achieve as IADs grow beyond the size limits of wind tunnel test sections. Static structural testing will also become more important as IADs continue to develop.

1.2.4 Materials

During the supersonic IAD development of the 1960s, work focused on materials with high strength and high temperature capability. Since most of a supersonic IADs (SIAD) deceleration occurs at high dynamic pressures, material strength is more of a concern. Additionally, SIAD deceleration occurs below Mach 5, so aeroheating is not a large concern. For a SIAD, high strength woven materials with good thermal characteristics such as Kevlar®, Vectran®, Nomex®, and , Technora® have emerged as popular materials [25, 3, 26]. Silicon or urethane coatings are often applied to the materials to reduce porosity and add abrasion resistance. LDSDs SIAD-E is

constructed from a braided Technora® coated with silicon capable of withstanding supersonic deployment temperatures [3].

A hypersonic IAD (HIAD) undergoes exo-atmospheric inflation and significant heat loads during entry due to the high operating Mach numbers, thus requiring a TPS. The materials must have low porosity, high heat resistance, strength retention, and chemical stability in the oxidizing environment. Recent HIAD developments have used several different material layers for the most effective and lightweight design. For example, the IRVE-3 stacked toroid TPS is made up of two outer layers of Nextel™ that serve an aerodynamic surface, two layers of Pyrogel® insulation, a Kapton® coated Kevlar® which provides a gas barrier, and load carrying Kevlar® webbing incorporated into the TPS in a radial pattern. As the number and complexity of materials utilized for IADs grows, so does the difficulty in analyzing the structure.

Predicting the response of such materials under aerodynamic loads is difficult even with FEA given the lack of textile material property knowledge. To aid in the finite element modeling of IADs, Hutchings utilized several experimental test methods to obtain material property data for candidate IAD orthotropic materials [26]. The material data obtained from this testing was utilized in Tanner's FSI work. Similar test methods were used in a combined effort between NASA and ILC Dover to carry out an experimental program to better characterize the stiffness of coated woven fabrics [25]. The results of this activity were intended to support a ground test campaign for inflatable decelerators. The work from the Hutchings and ILC Dover testing resulted in linear elastic and shear moduli, which are reasonable estimates for early design studies. However, data obtained from uniaxial tensile testing does not accurately represent the biaxial loading seen in flight. In addition, the shear modulus obtained from cylinder biaxial testing provides data at only one state of stress. Tanner and Hutchings both acknowledge the benefit of a more detailed characterization of woven fabric material properties as the limitations of the experimental studies provide

an incomplete picture. Researchers at the University of Maine have experimentally quantified the effective inflation pressure dependent constitutive properties of several coated, woven and braided textiles using tension/torsion tests on pressurized fabric beams to achieve various states of stress. The effective material properties obtained from those experiments were used in finite element models to validate four-point bending tests on inflated airbeams [27].

1.3 Air-Inflated Fabric Structures

Air inflated structures are tensioned structures that possess unique advantages in their use over traditional structures. Light weight designs, rapid and self-erecting deployment, enhanced mobility, large stowed-to-deployed volume ratios, fail-safe collapse, and possible rigidification are among these advantages.

The majority of R&D pursued in air-inflated structures can be traced to commercial, recreational, marine, military, and space applications. Examples include: Air Ships, Weather Balloons, Inflatable Antennas, Temporary Shelters, Pneumatic Actuators, Inflatable Boats, Temporary Bridges, and Automotive Air Bags.

However, the modern day advances in high performance fibers combined with continuous textile manufacturing processes has enabled a next generation of air-inflated structures. These air-inflated structures can be designed as viable alternatives to conventional structures.

Because these structures combine both textile and structural engineering disciplines, the following section will provide an introduction to the terminology used in textile materials and their manufacturing processes. Reference [28] provides additional insight. In addition, Reference [29] provides a more in depth look into air-inflated structures.

1.3.1 Basic Architecture

Air-inflated fabric structures are constructed on fabric shells that enclose a volume of pressurized air. The textile architectures that are most often used are shown in Figure 2. With selection of architecture comes its own design, manufacturing, tooling, and cost implications. These architectures behave different structurally when subjected to loads.

The plain-weave architecture utilizes orthogonal yarn placement that enables extensional stiffness along the two yarn axes. Unfortunately, it lacks shear stiffness for off-axis loads. The braided architecture, on the other hand, provides the fabric with shear stiffness due to the non-orthogonality of the yarns but lacks extensional stiffness. The angle between the braid axis and the yarns, θ, is often referred to as the braid angle or bias angle. Both triaxial braided and axial strap-reinforced braid architectures provide extensional and shear stiffnesses.
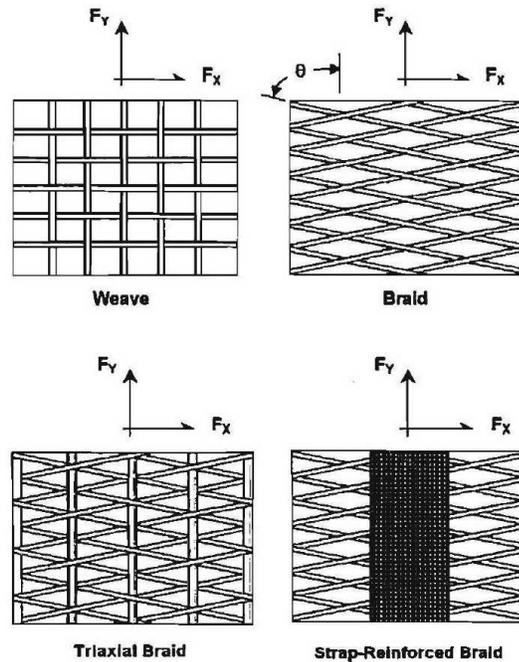
Figure 2: Example Fabric Architectures used in Air-Inflated Structures [29]

The air pressure develops a biaxial pre-tensioning state of stress through the fabric.

10

This enables the structure to generate the intended shape, while providing stiffness to resist deflections and stability against collapse from external loads. The fabric materials can often be modeled as tension-only or membrane materials, meaning their in-plane compressive and bending moduli are negligible, for design purposes.

Inflation pressure is a major variable when considering the stiffness of the structure. As inflation pressure increases, the stresses related to pre-tensioning of the fabric increase and, as a result, stiffen the structure. A complete redistribution of stress occurs due to the change in inflation pressure. This redistribution balances the loads and keeps the structure in a state of static equilibrium. Depending on the type of air-inflated structure and the applied loads (i.e., tension, compression, shear, torsion, etc.), the redistribution of stresses can either increase or decrease the net tensile stresses in the fabric. As long as no regions of the fabric experience a net loss in tension, the stability of the structure can be ensured. However, if the stresses from the applied loads begin to drive the tension to zero, the onset of wrinkling is said to have occurred within the structure. Wrinkling of the fabric decreases the structure's load carrying capability and with continued loading, buckling or collapse will occur.

Possibly, the two most significant advantages air-inflated structures have over conventional structures are that collapse is reversible and often visually detectable. Upon an overload condition, a collapse of the structure does not necessarily damage the membrane. As the overload condition is removed, the structure generally restores itself to its design load configuration. Since wrinkling can be visually detected, it can serve as a warning indicator before the collapse.

1.3.2 Fiber Materials and Yarn Constructions

In the design of air-inflated fabric structures, proper selection of fiber materials and yarn constructions are important factors. These should be simultaneously optimized to achieve desired performance characteristics at the fabric and structural levels.

Modern air-inflated fabric structures use high performance continuous fibers such as: Vectran® - thermoplastic liquid crystal polymer, PEN® - polyethylene naphthalate, DSP® - dimensionally stable polyester, Kevlar® - Para-Aramid, and Technora® - Aramid.

These fibers provide improved structural performance (high strength, low elongation, fatigue, flexibility, cyclic loadings, creep, etc.) and environmental resistance (ultraviolet rays, heat, humidity, moisture, abrasion, chemicals, etc.).

Yarns are constructed from fibers that are either aligned unidirectionally or in twisted bundles. Twist, which is measured in turns per unit yarn length, affects the yarn tensile properties. The twist is used primarily to protect the yarns during handling in textile processing. For discontinuous fibers, twist can increase the yarn breaking strength due to the internal forces at the fiber ends transferring to neighboring fibers via inter-fiber shear forces. Hearle, however, showed that twist in continuous fibers can reduce the yarn breaking strength [30]. Therefore, in the case of continuous fibers, it is often desired to have the minimum amount of twist to provide adequate handling protection.

Hearle also experimentally investigated the effects of twist on the tensile behavior of several continuous fiber yarns [30]. The results showed that yarn tenacity (tensile strength in grams-force per denier or grams-force per tex) decreased with increasing twist for three prescribed tensions used during twist formation. Overall, the yarn modulus decreased with increasing twist, yarn elongation at break increased with increasing twist, and yarn elongation decreased with increasing yarn tension. A difference in the load-extension behavior of twisted and non-twisted yarns is that a twisted yarn, when subjected to tension, will undergo compaction of its cross section through movement of its fibers and develop greater inter-fiber frictional forces than a non-twisted yarn. Similar to fabrics, the architecture and processing can be tailored to affect the structural performance of yarns.

The "as-processed" fabric structure can often behave differently than expected from the "as-designed" fabric structure. Once the fabric is constructed, it is recommended that tensile tests be carried out on sample yarns to be compared to the design requirements. Cavallaro measured the tensile properties of continuous-fiber, non-twisted yarns, that were removed from a plain-woven fabric airbeam, using an Instron® machine [31]. The experimental setup was similar to that shown in Figure 3. The cross-sectional areas of the yarns were estimated using the fiber diameter and quantity. The results showed that the average breaking stress of the weft yarns was approximately 20% less than that of the warp yarns. This reduction was attributed to fiber damage caused by the application of higher tension forces in those yarns during the weaving process.
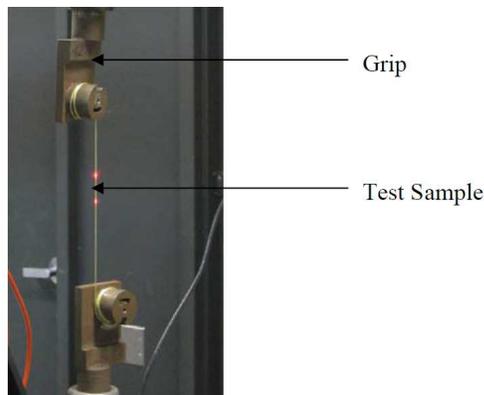
Figure 3: Yarn Tensile Testing using Instron®

1.3.3 Effects of Fabric Construction on Structural Behavior

Fabric materials are built from yarns that cross over and under each other in a repetitive, undulating pattern. The undulations shown in the geometrical model of a fabric as illustrated in Figure 4 are referred to as crimp. A full discussion of the geometrical model and its applications to practical problems of woven fabric design has been given by Peirce and Hearle [32, 33]. The warp (w) and weft (f) yarns, which are perpendicular straight lines in the ideal form of the fabric, become curved

under stress and form a natural system of curvilinear coordinates for the description of its deformed state. The basic parameters consist of two values of yarn length, (l), two crimp heights, (h), two yarn spacings, (p), and the sum of the diameters of the two yarns, (D). Given any four of these, the other three can be calculated from the model. There are three basic relationships among these parameters as shown in Equations (1) to (3). The definitions of the parameters set in the structural model are denoted as follows:

$$h = (l - D\theta)sin\theta + D(1 - cos\theta) \tag{1}$$

$$p = (l - D\theta)cos\theta + Dsin\theta \tag{2}$$

$$h_w + h_f = D \tag{3}$$
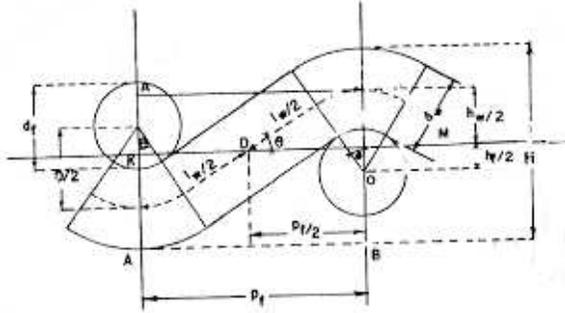
Figure 4: Fabric Geometric Model [33]

These equations are based on an idealized geometry and assumptions such as circular yarn cross sections and ignoring force or stiffness effects.

Braided fabrics will behave differently under load compared to plain-woven fabrics because their yarns are usually aligned at different angles. Braided fabrics have a $+\theta/-\theta$ yarn placement with respect to the braid axis, where θ is commonly referred to as the bias angle. In contrast, plain-woven fabrics have a nearly orthogonal yarn placement of warp and weft (or fill) yarns. By most textile definitions, warp yarns are those yarns running parallel to the selvage (a self-finished edge of the fabric that

14

is created by the weft thread looping back at the end of each row) and are virtually unlimited in length. The weft yarns are perpendicular to the selvage and are limited in length by the width of the weaving equipment.

The stress-strain behavior of plain-woven fabrics is initially dominated by crimp interchange rather than yarn elasticity. It is not uncommon for the factors of safety for air-inflated structures to be between 4-6 and as a result the operating stresses are low in comparison to the fabric strength. Therefore, the influence of crimp interchange must be considered when addressing the structural performance of fabrics. In addition, the relative yarn motions (slip and rotation) also affect the stiffness properties. The crimp ratio, (C), is defined, as in Equation (4), as the waviness of a yarn and is calculated by measuring the length of the fabric in the yarn direction, (L_{fabric}), and the length of the yarn after it has been extracted and straightened out, (L_{yarn}). This can be done for both the warp and weft yarns.

$$C = \frac{L_{yarn} - L_{fabric}}{L_{fabric}} \tag{4}$$

Using Equations (1) to (4), Equations (5) and (6) to relate crimp height and ratio:

$$C = \frac{l}{p} - 1 \tag{5}$$

$$\frac{h}{p} = \frac{4}{3}C^{\frac{1}{2}} \tag{6}$$

Consider a plain woven fabric subjected to a uniaxial tension along one yarn direction. The yarns under load will begin to straighten which decreases their crimp heights and elongates their effective lengths. As a result, the perpendicular family are forced to increase their crimp heights and decrease their effective lengths. This change in crimp height is referred to as crimp interchange and is often compared to the Poisson's effect from continuum mechanics. In uniaxial tension tests on plain

woven fabrics, crimp interchange can visibly reduce the width of the specimen.

As the biaxial tension increases for a given load ratio, yarn kinematics (slip at the cross over points) cease and the spacing between the yarns start to converge to minimum values. Backer describes this phenomenon as the extensional jamming point, which can prevent a family of yarns from straightening and as a result, not achieve it at full strength [33]. Crimp interchange is a function of the ratio of initial crimp between the yarn axes and the ratio of stress between yarn axes, not the stress level themselves. Crimp interchange is a source of nonlinear load-extension behavior for fabrics.

Next, consider the plain-woven fabric subjected to shearing through the application of a uniaxial load at $\pm 45°$ to either yarn direction. The yarns will rotate at the crossover points with respect to each other and become increasingly skewed as the angle between the yarns changes. The change in the angle between the yarns is referred to as the shear angle. As the shear angle increases, the available space between the yarns decreases and rotational jamming (locking or shear jamming) occurs. The angle at which the yarns become jammed is the locking or jamming angle. The locking angle decreases with increasing yarn density ratio and can be estimated from Peirce's model or calculated from experimental trellising or bias-extension tests. Loading beyond the onset of locking will produce wrinkles leading to localized out-of-plane deformations. It is important to determine extensional and shear jamming points for structural stiffness concerns.

1.3.4   Improved Damage Tolerance Methods

Various methods have been used to increase the reliability of air-inflated fabric structures against several damage mechanisms. Damage associated with punctures, impacts, tears, and abrasion can be mitigated by using high density weaves, rip-stop

fabrics and coatings. High density weaves are less susceptible to punctures and provide greater protection for bladders. Rip-stop fabrics have periodic high tenacity yarns woven in to prevent fractures of the basic yarns from propagating. The breaking strength of a yarn is referred to as tenacity which is defined in units of grams-force per denier. Denier is a mass per unit length measure given as the mass in grams of a nine thousand meter long yarn.

Coatings protect the fabric against environmental exposure (i.e., ultraviolet rays, moisture, fire, chemicals, etc.). Coatings such as urethane, silicone, PVC (polyvinyl chloride), neoprene, EPDM (ethylene propylene diene monomer) are commonly used. Coatings can be applied in two stages. First, coatings can be applied to the yarns prior to forming the fabric via a liquid bath immersion. This provides the best treatment to the fibers. Alternatively, coatings can be applied by spraying, painting, or laminating directly to the fabric after forming. This bridges the gaps formed between adjacent yarns. For maximum protection, both stages are often utilized. However, protective coatings have been shown to increase the stiffness of the fabric due to the restricting of relative yarn motion. The flexibility and packing efficiency advantages are not negatively affected by the coatings though.

1.3.5 Continuous Manufacturing and Seamless Fabrics

Before the development of continuous circular weaving and braiding processes, air-inflated fabric structures were constructed using piece cut manufacturing methods involving bonding segments using adhesives. These methods were limited to low pressures due to failures and air leakage at the seams. Continuous weaving and braiding techniques minimize or even eliminate the number of seams resulting in increased reliability, pressure capacities, and structural load carrying capability. In many circumstances, seams cannot be avoided and the structure should be designed such that failure occurs in the surrounding fabric rather than at the seams. Factors

of safety of appropriate magnitude for burst and seam failures should be prescribed for the safe and reliable utilization of these structures. As an example, a minimum factor of safety of four to six is often used on yarn strength.

Similar to more traditional composite materials, fabrics can be tailored to meet desired structural performance requirements. Fiber placement can be optimized for air-inflated fabric structures by varying the yarn denier (mass in grams of a nine thousand meter length yarn) and yarn counts along each direction. Consider a inflated fabric cylinder with a 2:1 ratio of hoop stress per unit length to axial stress per unit circumference. Equal factors of safety can be ensured against yarn failure in both directions by weaving twice as many weft yarns per unit length of the air beam than the number of warp yarns per unit circumference. As an alternative, the same goal can be accomplished by doubling the denier of weft yarns with respect to the denier of warp yarns.

1.3.6 Air Beams

Air beams are an example of air-inflated structural elements that are capable of supporting several types of loads similar to conventional beams. To date, seamless air beams, with diameters up to 42 inches, have been built with continuous manufacturing methods. An outer fabric skin surrounds an internal bladder usually made from an elastomer material. The purpose of the bladder is to contain the air, prevent leakage, and transfer the pressure load to the fabric. Air beams have cylindrical cross-sections with lengths that can be tailored to be straight or curve to form an arch or torus. A variety of termination methods have been used to close the ends such as bonding, stitching, and mechanical clamps. The selection of termination method depends on the inflation pressure, loading requirements, and desired shape. Clamping methods have the advantages of permitting assembly, repair, and replacement of the bladder and fabric layers.

A pressurized air beam pretensions the fabric and provides the air beam with axial, bending, shear, and torsional stiffnesses. As shown in Figure 5, the ratio of cylindrical (hoop) stress per unit length of an inflated air beam to the longitudinal stress per unit circumference is 2:1.
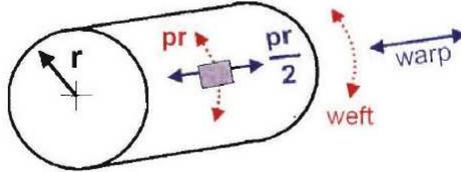
Figure 5: Plain-Woven Fabric Cylinder Yarn Tensions

The weft yarn tension per unit length of cylinder is equal to the internal pressure multiplied by the radius of the cylinder. The warp yarn tension per unit circumference is half the weft yarn tension. Equation (7) expresses the yarn density ratio (YDR) as a ratio of the number weft to warp yarns.

$$Yarn\ Density\ Ratio\ (YDR) = \frac{\#\ weft\ yarns\ per\ unit\ length\ of\ cylinder}{\#\ warp\ yarns\ per\ unit\ circumference} \quad (7)$$

The warp yarns of plain-woven air beams are aligned parallel to the longitudinal axis of the air beam and resist axial and bending loads. The weft yarns spiral through the weave and are located at approximately 90° to the warp axis and lie along the hoop axis of the air beam.

In the case of braided air beams, the braid axis runs along the longitudinal axis of the air beam. Assuming the ends of the braided air beam are unconstrained from moving in the longitudinal direction, the yarns will rotate exhibiting a scissoring effect that causes the length of the beam to length or shorten with pressure depending on the selection of braid angle. Eventually, the yarns will reach a maximum rotation angle and become jammed. This phenomenon can be explained by applying netting theory [34]. The bias angle can be adjusted to allow either contraction or expansion of

the air beam during inflation. In order for an unconstrained braided air beam to resist axial tension, longitudinal reinforcements must be incorporated, such as as distributed axial yarns (triaxial braid) or axial straps attached around the circumference. Brayley tested the bending response of inflatable, braided beams and arches with external reinforcing straps [35]. The work focused on experimentally determining the constitutive properties of the constituent materials, and quantifying the load-deformation behavior of beams and arches with full scale laboratory tests. The straps were tested in pure tension to obtain accurate tensile modulus. The braided material was tested in torsion to obtain shear modulus as a function of inflation pressure.

The bending stiffness, (EI), for beams normally has units of force x distance^2 and is written as the product of the elastic modulus, (E), and the area moment of inertia, (I). For air inflated fabric structures, the fabric elastic modulus, (E_f), is commonly expressed in units of force per unit length. Thus, $E_f I$ is in units of force x distance^3. Fabric strengths are also typically expressed in units of force per unit length.

Next, consider an air beam under transverse loads. The pre-tension and bending stresses algebraically add. The compressive bending stresses relax or subtract from the pre-tension on the compressive surface of the beam, while the tensile bending stresses add to the pre-tension on the tensile surface. If any point on the air beam develops a net zero longitudinal tensile stress, the onset of wrinkling is said to have occurred in the structure. The corresponding bending moment is referred to as the wrinkling moment, (M_w). Prior to wrinkling, the moment-curvature relationship is linear, assuming there are no material nonlinearities or significant changes in pressure or volume. A stress balance based on classic strength of materials theory is generally used to calculate, M_w. Once the onset of wrinkling has begun, the air beam moment-curvature relationship is nonlinear because with further loading, the cross-section loses bending stiffness and the neutral axis moves away from the centroidal axis of the cross-section and eventually the beam collapses. The wrinkling spreads around

the circumference of the beam in a similar manner to the flow of plasticity in metal beams under bending loads. Loading beyond the onset of wrinkling will decrease the beam's volume and as a result will increase the internal pressure. In addition, the work done on the air will affect the post-wrinkled bending stiffness and the response becomes nonlinear. Figure 6 shows the superposition of the pressure and bending induced forces for three air beam architectures.
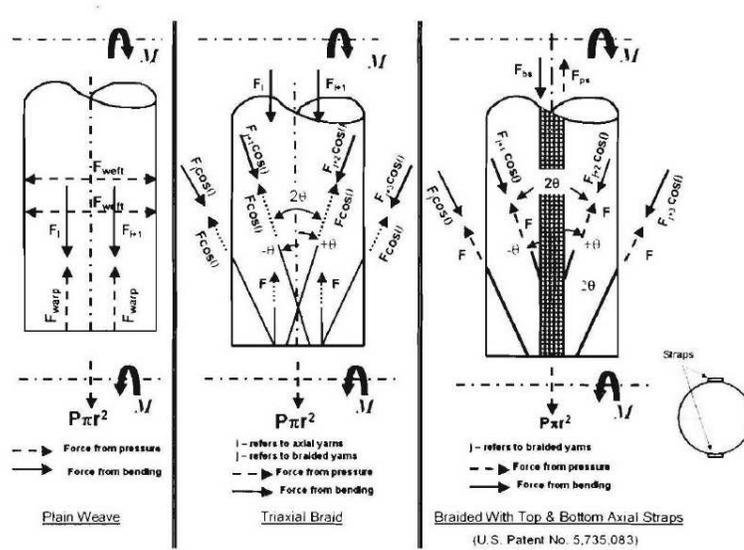
Figure 6: Superposition of Pressure and Bending Loads in Plain-Woven, Triaxial Braided, and an Axial Strap Reinforced Braided Air Beams [29]

Inflatable braided, strapped beams were tested at the University of Maine in the 2009. The beams were provided fully assembled by Vertigo, Inc. of Lake Elsinore, CA. The beams were constructed with an internal urethane bladder, a braided fabric at a 75° bias, and four external reinforcing straps as shown in Figure 7. The beams were coated for protection from abrasion. Strap material and inflation pressure were varied to determine the effect on the load-deflection response and ultimately obtain load-deflection data for model validation and calibration [35].

Tests were conducted at inflation pressures of 69, 138, 207, 276, and 345 kPa. Beams were tested in a three and four-point bend configuration. Figure 8 shows the layout of the four-point bend test setup.
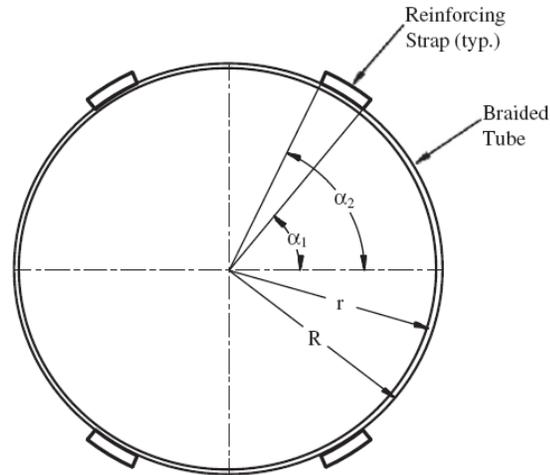
Figure 7: Cross-Section of Braided Member with External Reinforcing Straps [35]
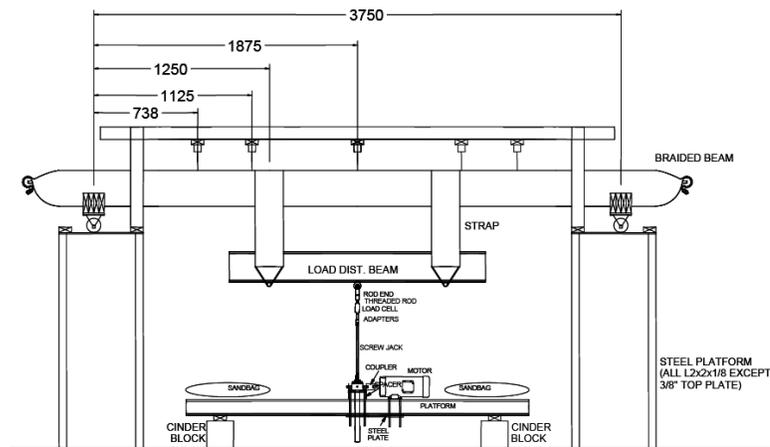
Figure 8: Air Beam Four-Point Bend Test Diagram [35]

A beam finite element model that accounts for braid angle and strap stiffness was developed to model the bending response of the inflatable, braided strapped beams and arches. Quasi-static load-deformation tests of arches and beams were performed to provide data for model validation. The FE model effectively predicted the load-deformation response of the members to and beyond the point of fabric wrinkling as shown in Figure 9.
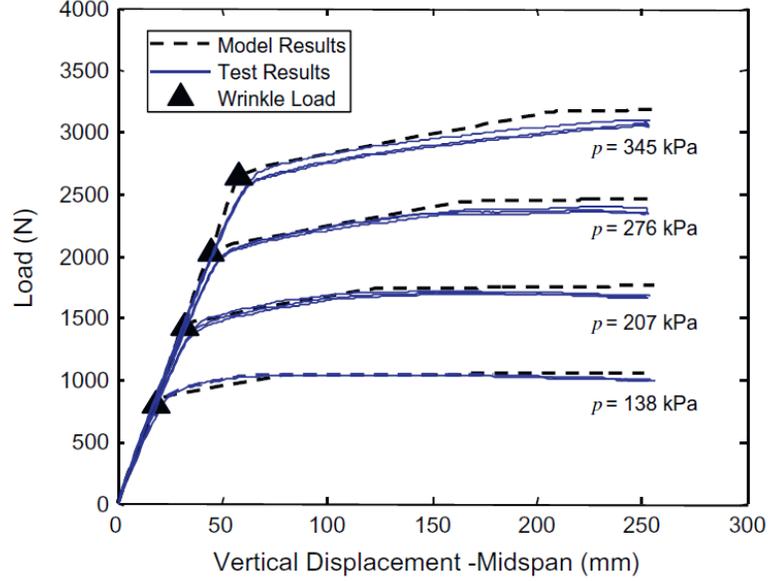
Figure 9: Air Beam Four-Point Bend Test Results [35]

1.3.7 Effects of Air Compressibility on Structural Stiffness

In addition to the initial inflation pressure, the load-deflection response of air-inflated fabric structures may have other stiffening sources. Sources include nonlinearities in the fabric stress-strain response and the work done on the air by external forces. If appreciable changes in pressure or volume occur during loading, work is performed on the air compression which stiffens the structure. From thermodynamic principles, the Ideal Gas Law shown in Equation (8) models the air compressibility using absolute pressure (P), volume (V), mass (m), air gas constant (R), and temperature (T).

$$PV = mRT \tag{8}$$

Assuming a quasi-static isothermal process, the work done on the air by compression is as shown in Equation (9).

$$W_{air} = \int_{V_1}^{V_2} P dV = \int_{V_1}^{V_2} \frac{mRT}{V} dV = mRT \ln \frac{V_2}{V_1} \tag{9}$$

The total energy of the structure, (E_{total}), shown in Equation (10) is the work

done by all external forces, (W_{ext}) which is equal to the total strain energy of the fabric, (U_f), plus (W_{air}), from Equation (9).

$$E_{total} = W_{ext} = U_f + W_{air} \qquad (10)$$

In the case of homogeneous membranes, the elastic and shear moduli are determined from standardized tests. However, for the case of plain-woven and braided fabrics, the elastic and shear moduli vary not only as a function of pressure but also with fabric architecture, external loads, and coatings (if present).

1.4 Fabric Material Property Determination

It has been shown that fabric material properties are a function of applied loading: mechanical and thermal. Theoretical analysis of fabrics can become quite complicated and relies on validation from experimental testing. A great deal of work has been done to better determine the mechanical properties of fabrics experimentally. Basset et al. reviews several experimental methods for determining fabric elastic and shear moduli [36]. Uniaxial and biaxial tension, trellis-frame, and bias-extension are performed to measure one of the fabrics mechanical properties while keeping the others constant. Combined load testing like the inflated cylinder test, utilize hydrostatic pressure, axial force, and torsion to simultaneously vary the state of stress.

Generally, there are three stress-strain behaviors of interest that are obtained from an experimental test: Normal stress vs. strain in the warp and weft directions, transverse contraction vs. axial strain, and shear stress vs. shear strain. Due to the nature of fabrics, these three relationships are coupled. As an example, a highly tensioned fabric will have a different shear modulus than the same fabric will have under lower tension. For most applications, the fabric thickness is usually much less than the other two dimensions. Therefore, the bending properties are assumed to have a negligible effect and only in-plane properties are considered. Viscoelastic effects

24

and friction have received considerable attention in the past [37, 38], but sufficient information for including frictional and viscoelastic effects in an analysis involving multiple independent and dependent variables is currently lacking and therefore often neglected.

1.4.1 Separate Test Methods

Hearle categorizes three regions of stiffness for tensile loading of a plain-woven fabric as shown in Figure 10 [33]. Initially, the yarns slide with resistance due to friction. As the load increases, crimp interchange occurs before leading to elastic behavior. In practice, air-inflated fabric structures are designed to operate in the inter-fiber friction and decrimping regions. This ensures that the yarns are loaded well below their breaking strength.
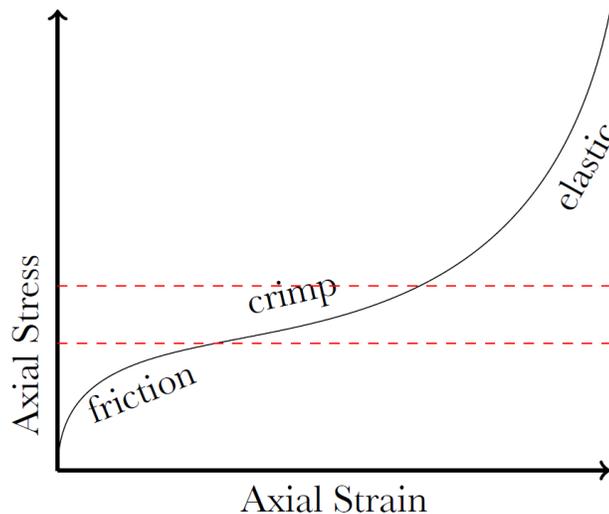
Figure 10: Idealized Uncoated Response [39]

Uniaxial and biaxial tension tests are the most common methods to determine tensile moduli in the warp and weft directions. The presence of transverse loading has been shown to have a large effect on the apparent stiffness of the fabric due to decrimping and significantly affects the effective Poissons ratio (ν); historically, however, uniaxial tests have been used most often due to available test apparatuses.

Many testing methods have been developed for evaluating the mechanical properties of yarns and fabrics including ASTM standards, Kawabata Evaluation System, MIL-Spec, and British Standards. It is recommended that an engineer become familiar with the applicability of these standards to the design and testing of fabric materials as applicable to air-inflated fabric structures. Recently, many researchers have used the methodology for uniaxial testing for fabrics that is standardized by ASTM D-5035-0641 [26, 25, 40]. Typically elongation, which is used to compute strain, is tracked with an optical method, an attached extensometer, or crosshead extension. Figure 11 shows examples of uniaxial and biaxial testers found in literature.
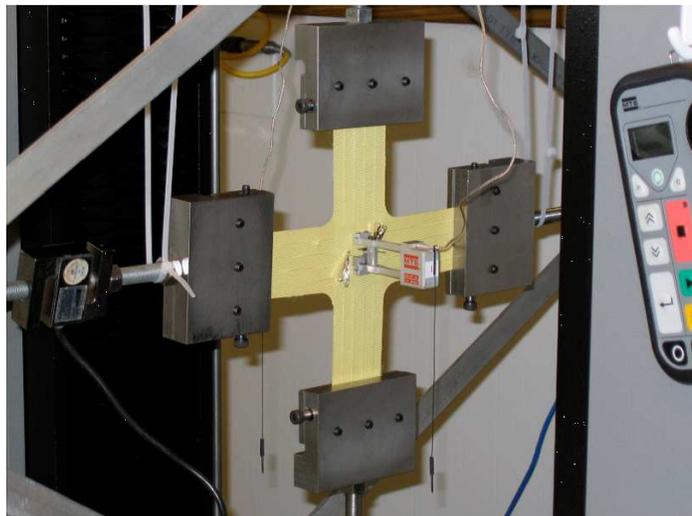
(a) Uniaxial Tension   (b) Biaxial Tension

Figure 11: Uniaxial and Biaxial Tension Test Methods [26, 40]

Once the fabric is biaxially stressed and subjected to an in-plane shear stress, the yarns will shear (rotate) with respect to their original orientations. The shear stiffness (resistance to yarn rotations) results from inter-yarn friction and compaction at the crossover points. Therefore, the shear modulus is actually a system property rather than a constitutive (material) property. As the shear rotations increase, an upper limit is reached when then yarns in both directions become locked or jammed.

Farboodmanesh et al conducted shear tests on a rubber coated plain woven fabric [41]. The results showed that the initial shear response was dominated by the coating and with increased shearing, the behavior transitioned to that of an uncoated fabric. The idealized shear stress-strain behavior of a coated woven fabric is presented in Figure 12. A rubber sheet demonstrates a plastic response, while woven fabrics typically have a hyperelastic response. The response of a coated woven fabric is typically a composite of these patterns, with the rubberized sheet dominating at low strain, and the woven fabric at higher strain.
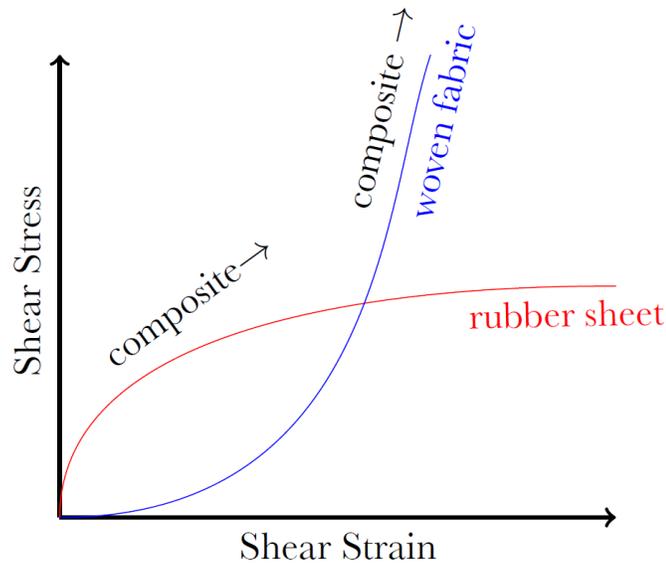
Figure 12: Idealized Coated Response [39]

As discussed earlier, shear behavior generally consists of several phases, such as deformation when the shearing forces at yarn intersections are too small to overcome friction, slippage of the yarns once that friction is overcome, and elastic deformation after yarn locking. While the shear modulus is usually much less than the elastic modulus for plain-woven fabrics in the warp and weft directions, it has a significant effect on the effective moduli of orientations not aligned with the warp and weft directions. Two common tests to determine shear behavior are the trellis frame and bias extension tests, as shown in Figure 13 [25].

27
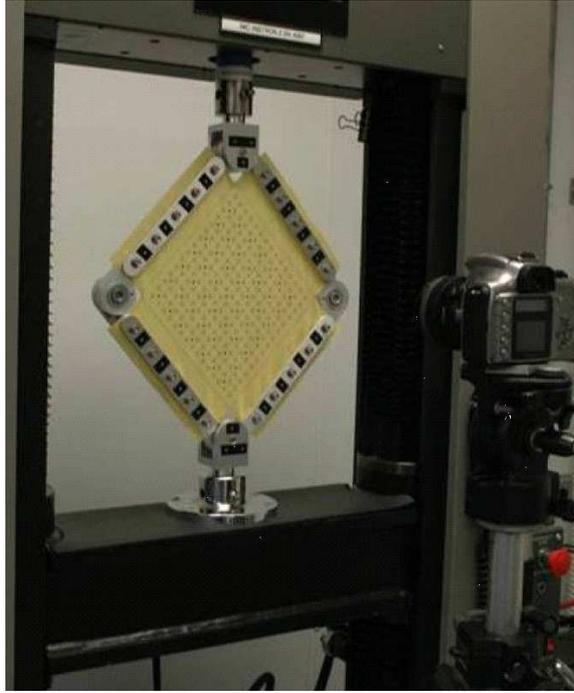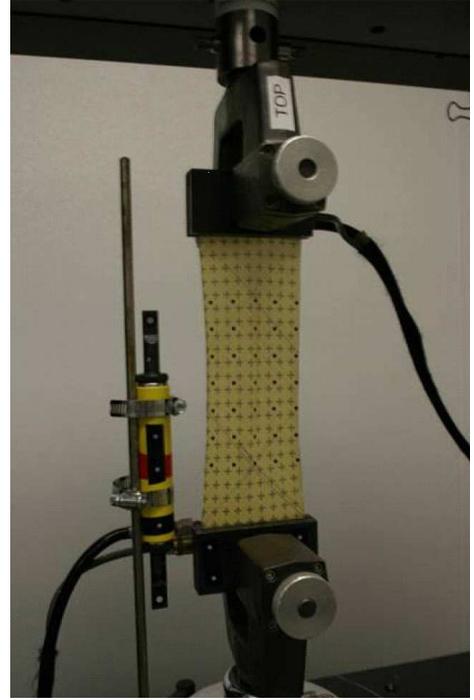
(a) Trellis Frame   (b) Bias Extension

Figure 13: Shear Test Methods [25]

The Bias-Extension test method can be combined with uniaxial tension tests in the warp and weft directions to estimate the shear modulus, (G), using Equation (11) [42].

$$G_{12} = \left(\frac{4}{E_{45}} - \frac{1}{E_1} - \frac{1}{E_2} + \frac{\nu_{21}}{E_1} + \frac{\nu_{12}}{E_2} \right)^{-1} \tag{11}$$

While this equation is a linear approximation, a nonlinear solution can be obtained using theory from large deformation continuum mechanics. Using the deformation gradient for two line elements, one originally aligned with the warp yarns and the other with the fill yarns, the Green-Lagrange strain tensor can be derived. In practice, line markings are made on the sample and tracked over time using photogrammetry. For each photo, the length of each line element is used to determine the stretch and orientation.

28

1.4.2 Combined Test Methods

Biaxial inflated cylinder tests use internal pressure to create a 2:1 stress ratio in the material. Additional tension and/or torsion can be applied to change the axial and shear stresses. Hutchings carried out biaxial cylinder tests on several IAD fabrics; however, only shear modulus at one state of stress could be obtained as the test apparatus did not have the capability to apply tensile loads [26]. Hutchings points out that cylinder testing is important for structural fabrics because stiffness, which is dependent on the internal pressure, is generally more important than the strength in inflatable applications.

Kabche et al experimentally applied tension and torsion loads to inflated beams to obtain effective material properties as a function of internal pressure [43]. The test setups used by Hutchings and Kabche et al are shown in Figure 14. Pressure dependent material properties were used in a beam based finite element model to predict the response of the beam in bending. It was shown that the effective elastic and shear moduli of the fabric varied as a function of inflation pressure, material properties of the fibers, and the structure of the weave. These are very useful observations, but required large amounts of testing and the quantitative results are only applicable to the specific fabrics in their study.

Cavallaro et al utilized a novel test fixture for experimental testing of fabrics subjected to combined biaxial tension and shear loads as shown in Figure 15 [44]. Through a combination of analysis and experimentation, the work addressed changes in fabric architecture and the combined effects of biaxial tension, shear, and crimp interchange on the global behavior of woven fabrics. The fixture was designed for use with conventional tension-torsion machines to characterize the elastic and shear moduli of fabrics as a function of biaxial loads. It utilizes a standard cruciform shaped specimen and was designed to evaluate both strength and stiffness properties of various fabric architectures subjected to biaxial loads, shear loads or combined

29

(a) Torsion Only   (b) Tension-Torsion

Figure 14: Inflated Cylinder Test Methods [26, 43]

loads. For fabrics constructed of two principal fiber directions, the fixture utilizes two rhombus-shaped frames connected with rotary joints. Cavallaro notes that for triaxial braided fabrics, the fixture has a third rhombus-shaped frame with additional rotary joints.

Lastly, full field strain measurement, while avoiding any mechanical interference with the specimen, is of great interest to researchers of inflatable structures [5]. Photogrammetry is a measurement technique used to estimate the 3-dimensional coordinates of points on an object. Post processing of the photogrammetry data provides the trajectory of a discrete set of material points as load is applied. This discrete set of points corresponds to the locations where the targets were attached to the fabric. With the kinematics known at these discrete points, the calculation of the displacement vector is possible. When the photogrammetry targets are laid out in a grid, the spatial derivatives of the displacement vector can be approximated. The displacement vector data can be interpolated to finer resolution grids to result in more

(a) Biaxial Tension   (b) In-Plane Shear
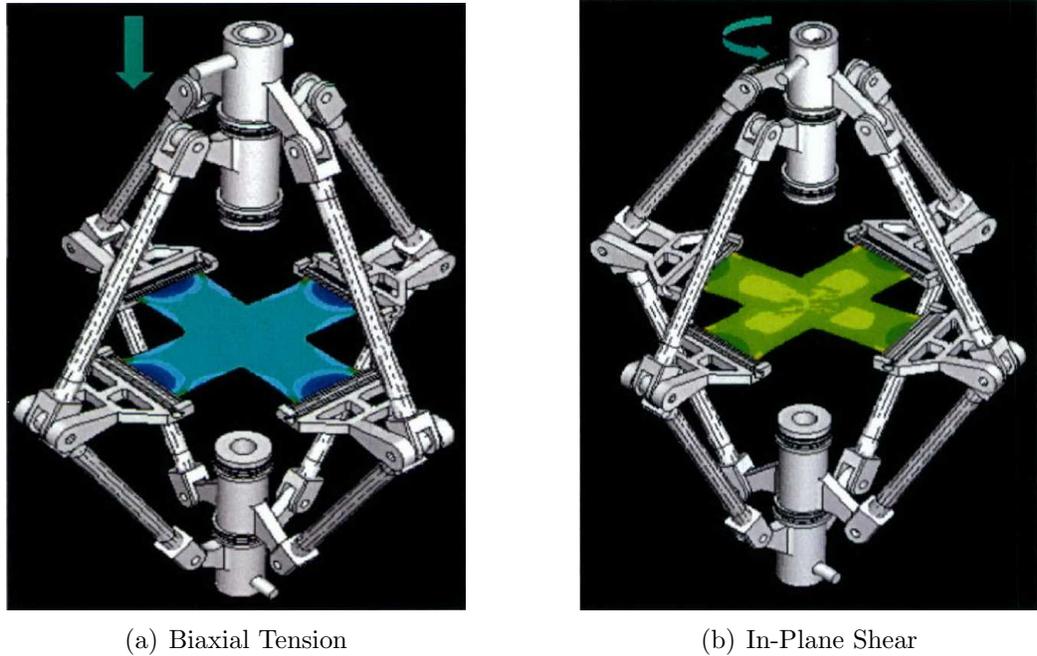
Figure 15: Combined Biaxial Tension and In-Plane Shear Test Methods [44]

accurate derivative approximations. In either case, the Lagrangian strain tensor is computed with the displacement vector spatial derivatives. Obtaining additional data for comparison and correlation between test methods, aids in determining which are best suited for validation efforts.

1.5 Analytical and Numerical Models

Early mechanical modeling of woven fabrics date back to the 1930s. This work was analytical and focused on tensile and shear of fabrics based on the weave geometry of a unit cell [33, 32, 45, 46]. Work has shifted to computational modeling in recent years, where more complicated fabric architectures and loadings can be considered. The computer graphics and composites industries have pioneered much of the latter computational modeling. Most of the computer graphics work focused on visual applications rather than mechanical behavior [47], while the composites industry has focused on manufacturing processes. Several approaches have been developed to

simulate the macroscopic behavior of woven fabrics, such as yarn models, particle-spring models, and continuum models. Particular emphasis is placed on continuum models as much of the recent work has been focused large scale simulations.

1.5.1 Yarn Models

Analytical models for yarns have built on the work of Peirce, who set the standard for plain woven yarn geometry, shown in Figure 16 [45]. These models capture the behavior of woven fabrics by defining a unit cell or the smallest repeating pattern in the fabric and studying the yarns interactions in the weave. Tensile, shear, and contact forces acting on yarns are determined from extensions and rotations of the yarns. After the forces on the yarns are calculated, the number of ends or picks per unit length is used to calculate the force per unit length of the fabric. An analytical solution for the initial elastic moduli of a plain woven fabric due to decrimping was derived by Grosberg and Kedia [46]. The work assumed an inextensible thin beam model for the yarns in the decrimping region. The shape of the yarns between intersection points is determined from the reaction forces, initial geometry and yarn material properties.
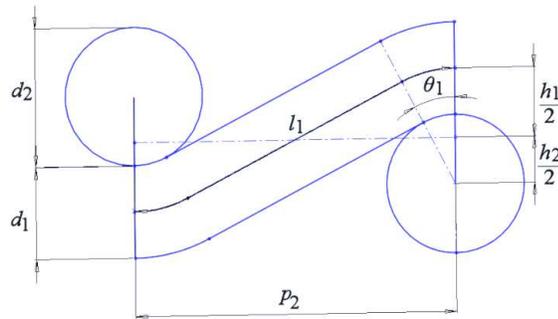
Figure 16: Peirce's Basic Plain Weave Yarn Geometry [45]

Later, Kawabata et al studied the deformation of fabrics subjected to biaxial, uniaxial, and shear loading [48, 49, 50]. The theory assumed elastic, but not necessarily linear behavior. The biaxial model is a function of several parameters, including:

yarn material properties, densities, crimp, spacing in warp and weft directions, angle defined by the yarn and out-of-plane axes, unit cell yarn length, undeformed distance between the neutral line and the yarn axis along the out-of-plane axis, and the deflection of the yarn along the out-of-plane axis in the deformed state. Using information from the original and deformed geometries, Kawabata et al developed a procedure to find the tensile forces in the warp weft yarns, as well as, the contact forces at the intersection points from the stretch ratios in each yarn direction, as shown in Figure 17.
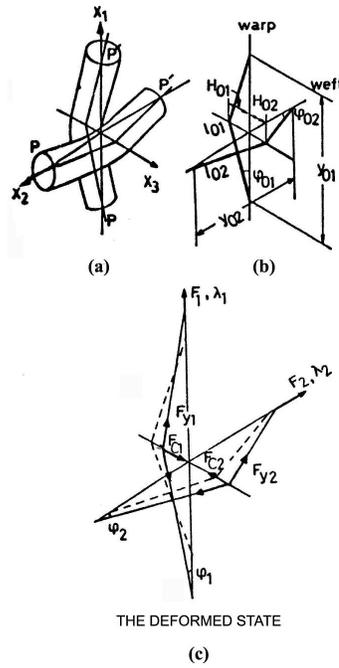
Figure 17: Kawabata's Basic Plain Weave Yarn Geometry [48]

Later models were modified to include changes in the yarn cross-section. Verification of the model included comparison of theoretical results with experimental results for two loading conditions: uniform biaxial loading ($\lambda_1 = \lambda_2$) and strip biaxial loading ($\lambda_1 \neq \lambda_2$) . The stretch ratio, (λ), is defined in Equation (12).

$$\lambda = \frac{deformed\ length}{undeformed\ length} = strain + 1 \tag{12}$$

In the case of uniaxial tension, the biaxial theory has to be adjusted, as the tensile

force in the transverse direction being zero would result in the contact force also being zero; which does not align with experimental results [49]. Modifying biaxial theory to include a first order approximation for contact force based on material and geometric information, the contact force at an intersection point is shown to be the summation of normal and shearing forces. Since the shear term can be positive or negative depending on a state of loading or unloading, the model can capture the hysteresis seen in experimental data.

Finally, the theory was extended to include shear deformation [50]. Using linear approximations and contact forces, an estimate can be made for the moments required to change the yarn intersection angle by a prescribed angle. Along with the yarn extensions, moments were used to calculate shear forces. Again, experimental data was compared to theoretical results. Overall, the models developed by Kawabata et al provide realistic results for biaxial, uniaxial, and shear deformation that include nonlinearity and hysteresis. However, the models are not conducive for large scale or complex fabric simulations due to the necessary computations. Furthermore, the number and type of input parameters are cumbersome to obtain.

In addition to analytical models, unit cell finite element analysis has been implemented to obtain effective material properties. Cavallaro experimentally and analytically tested the bending response of an inflated beam [31]. In addition, the micro and meso mechanical effects were studied through finite element modeling. It was observed that a full-scale beam model which included each warp and weft yarns, as well as, their interactions was too computationally expensive. A unit cell of the fabric was built to extract material properties that were then implemented in a model of the inflated air beam. The results showed that the finite element model was stiffer than the experimental results. This was due to finite element model employing constant elastic and shear moduli, while the experimental material properties varied during loading [31]. Figure 18 shows the 4-point bending setup and sub-scale sections.
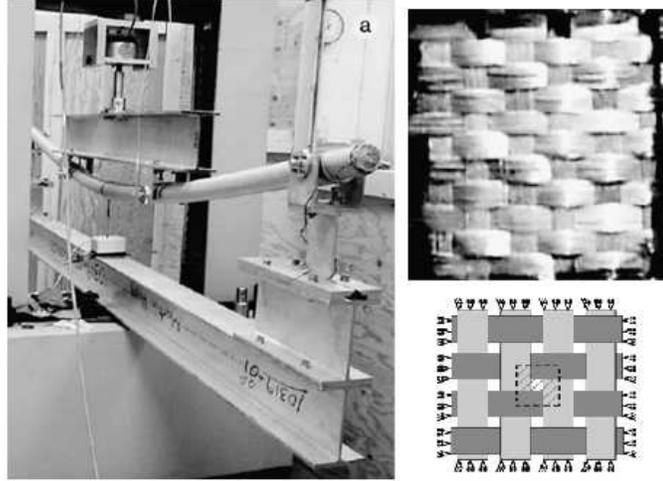
Figure 18: 4-Point Beam Bending and Fabric Sections

Peng and Cao utilized a novel approach for predicting the effective nonlinear elastic moduli of a textile fabric [51]. A unit cell as shown in Figure 19 was built and various numerical tests, like uniaxial tension testing and shear testing were carried out. Force vs. displacement curves were obtained from the unit cell and an iterative procedure was employed to transfer effective material properties to a four node shell element that could be applied to large scale model [51].
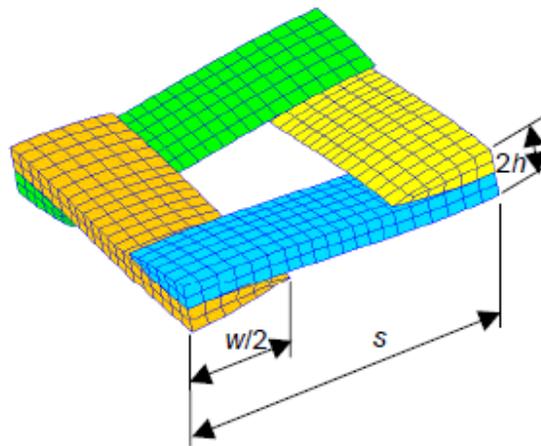
Figure 19: Plain Woven Fabric Unit Cell [51]

Komeili and Milani observed that the meso level finite element modeling of fabrics had mostly been based on individual axial tension and shear modes [52]. They

presented a general unit cell model modified from that of Badel [53]. The effect of combined loading on the response of a fabric unit cell was studied under different combined axial-shear loading modes. Axial loading was induced through controlled displacement along the yarns and shear loading was applied through controlled rotations on the boundaries of the unit cell. Results showed a high level of nonlinear interactions between the material response in the axial tension and shear modes. Interestingly, it was found that under combined loading, the crimp changes due to each loading mode affected the reaction from the other mode. In a subsequent study, geometrical and material related uncertainty factors were studied using two-level factorial designs. Through the obtained half-normal probability plots as well as main and interaction effects, the most significant parameters were identified and discussed [54].

1.5.2 Particle-Spring Models

The efforts in computational modeling of fabrics at the macroscopic level have focused on two areas since the 1990's: Particle-Spring Models and Continuum Models. Particle-Spring methods, pioneered by Breen [55], are derived from yarn geometry and treat the intersections of warp and weft yarns as point masses or particles that are connected to other particles by springs and dashpots as shown in Figure 20 that can account for the stretching, shearing, and bending of fabric.
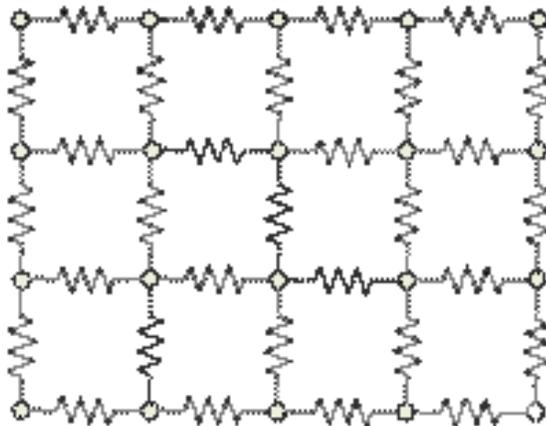
Figure 20: Example Particle-Spring Mesh [55]

36

With respect to macroscopic deformation, particle-spring models are able to accurately predict fabric behavior by tuning the spring and dashpot parameters to match experimental data. Broubaker et al studied yarn interactions and their effect on fabrics using particle-spring models [56, 57, 58]. Recently, Zhou et al used particle-spring models to predict out-of-plane buckling using in-plane shear loads [59]. While this method has been used extensively in computer graphics simulations due to the ease of implementation and visual realism, the input parameters are not tied directly to the material and are difficult to obtain when loading is unexpected.

1.5.3   Continuum Models

Currently, researchers most often utilize FEA to simulate loading of woven fabrics. As stated before, woven fabrics are actually discontinuous and heterogeneous systems composed of individual yarns and fibers. Continuum models, however, homogenize these systems into a thin continuous medium. Because the fabric thickness is usually much less than the in-plane dimensions, plane stress orthotropic material models are often developed for shell or membrane elements.

Peng and Cao developed a continuum mechanics-based constitutive model for woven fabrics. The model allowed for non-orthogonal unit vectors that correspond to the local orientation of the warp and weft yarns [60]. A coordinate system that coincided with the warp and weft yarns was used in a shell element. Experimental tension tests showed three regions of load-deformation behavior: a region with small tensile modulus due the decrimping of yarns, a larger approximately linear tensile modulus, and a final region with a non-linear modulus resulting from damage to the fabric. Experimental shear tests showed two regions: an initial decrimping and yarn rotation region followed be a stiffer region due to the locking of yarns. Material properties were obtained by curve fitting the experimental tensile and bias-extension data. Numerical results were validated with experimental results from bias extension

and shear testing.

Ruiz and Gonzalez implemented various hyperelastic strain energy functions that were expressed as a function of the strain tensor to model fabrics [61]. Two cases were considered: one with only uniaxial tension data and another with uniaxial tension, biaxial tension, and shear data. The methodology involved selecting a hyperelastic model, introducing experimental data, determining model coefficients through a non-linear regression technique, and finally utilizing FEA to solve a test case. In the case of uniaxial tension only, the Mooney-Rivlin, Yeoh, and Arruda-Boyce models fit the experimental data best. In the other case, the Mooney-Rivlin fit the data well. However, only the uniaxial tension cases with Yeoh or Arruda-Boyce models were able to reach convergence.

Multiscale analysis is an extension of continuum models. In the multiscale approach, the fabric is considered a continuum that is subjected to macroscopic loads and boundary conditions. To serve as an input to a unit cell analysis, the deformation gradient at integration points is calculated using a combination of continuum mechanics and finite element methods. From this, yarn modeling or particle-spring methods are used to calculate forces acting on yarns. Forces are then averaged and used to calculated continuum scale stresses. King et al and Nadler et al performed work in this area [62, 63]. Ivanov and Tabiei presented a computational material model for plain woven fabrics for use in FEA [64]. The model utilized a combination of the mesomechanical approach and the homogenization technique. The mesomechancial model is made efficient and suitable for large-scale analyses by breaking the unit cell into four subcells as shown in Figure 21 and using symmetry to reduce computations.

This model accounts for the reorientation of yarns and the fabric architecture. The behavior of the fabric is achieved by discounting the shear moduli of the material in the free state. The model was implemented in the LS-DYNA nonlinear finite element analysis code. The developed model has been validated using experimental
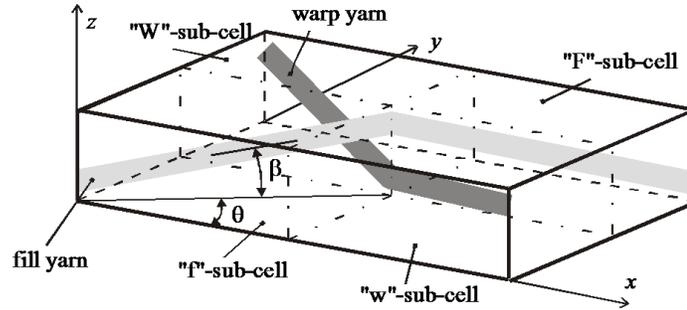
Figure 21: Tabiei and Ivanov Representative Volume Cell [64]

ballistic impact test data on Kevlar® fabric. By combining the advantages of yarn and continuum models, a multiscale approach shows promise to predict the effective nonlinear elastic material properties of fabrics.

1.6   Motivation

Three important insights are taken from the literature. The first is that previous IAD structural analyses have approximated the fabric as a homogeneous material and utilized only macroscopic models of the effective mechanical behavior. These models have relied on constitutive relationships that do not capture actual fabric behavior. Micromechanical structural analysis of the fabric is possible using a model of the individual fibers; however, this is computationally intensive and not practical in the conceptual or preliminary design stage with current resources. Mesomechanical models, which treat the yarns as a continuum, are able to capture yarn reorientation and fabric architecture and are more suitable for large scale analysis. For a multiscale approach to be useful, new methods will need to be defined to accurately model the yarns and their interactions. In addition, validation of mesomechanical models against experimental data will be required.

The second insight is that experimental determination of IAD material properties has provided an incomplete picture of the load-deformation behavior. References present some uniaxial tensile stress and shear stress data, but lack data at several states of stress and from different test equipment. Due to the cost and time required

for complete experimental investigation, researchers have utilized equipment that is readily available. The modeling of fabric structures would benefit from the publication of additional macro and meso level material data. In addition, there are several experimental methods for obtaining fabric material properties, but no comparison has been made between the methods.

Lastly, there have been several efforts to numerically determine the effective material properties of fabrics [31, 51, 52]. Approaches include the homogenization method, the finite element method, as well as both analytical and experimental approaches. It is impractical to experimentally obtain material characterizations for all the possible composite materials and fabric geometries. Furthermore, new testing is required when any changes are made to the fabric. It can be difficult to apply analytical methods when the fabric geometry becomes complex. While the homogenization method works well for predicting material properties, it comes with a large computational cost. By combining the advantages of the finite element method with the homogenization method, a procedure can be developed for predicting the effective nonlinear elastic moduli of fabrics. Though the textile industry has proposed this methodology for rigid composite applications, no evidence has been found for application of this technique to inflatable structures.

1.7 Contributions

This investigation proposes the development of a multi-scale flexible material modeling approach that enables efficient high-fidelity IAD design and a critical understanding of the new materials required for robust and cost effective qualification methods. The approach combines knowledge of the fabric architecture, analytical modeling, numerical simulations, and experimental data to build a physics-based understanding necessary to rapidly develop new materials that are optimized for an intended use. Rather than relying solely on experimental data, the initial goal is to shift toward

the prediction of material behavior based on first principles, backed up by experimentation. The ultimate goal is to eventually reduce the cost and time to develop and certify flight systems. Three objectives are described below to reach this goal.

Application of Parameter Identification to Current Experimental Mechanical Property Determination Methods. Based on the above-mentioned elements, this work aims to identify an efficient method that is as simple and as fast as possible for determining IAD material characteristics that does not utilize complicated or expensive research equipment. Starting from the uniaxial tensile test on the warp and weft directions and on the bias test, it is sought to determine the mechanical property data needed for introduction into a complex IAD simulation. The material characteristics of the fabric material are obtained by applying an established parameter identification methodology. The analysis imposes a decrease in the mismatch between the force-displacement curves obtained numerically and experimentally, respectively, for both directions (weft and warp) as well as the decrease in that of the extension curve for the Bias-Extension test. This methodology can be applied immediately to existing material models without the utilization of complicated or expensive research equipment.

Application of Parameter Identification to a Mesomechanical Material Model. Structural analysis codes such as ABAQUS, ANSYS, and LS-DYNA have been investigated for IAD applications; with LS-DYNA producing the most consistent answers. The fabric material model in LS-DYNA was originally developed for the airbag industry. The model is a variant of a nonlinear orthotropic material model and is valid for 3 or 4 node membrane elements. This model has been used by the IAD industry, but has required excessive augmentation to model inputs in order to recover realistic deformations. A second (higher fidelity) fabric material model in LS-DYNA was developed for ballistic impact applications in 2001. This model considers a mesomechanical approach to model the response of dry plain woven fabrics, but

requires information not typically tested for in standard methods regarding behavior of the yarns themselves. The present investigation will recontextualize this existing mesomechanical model through validation for structures pertaining to the analysis of IADs. In addition, corroboration and elaboration of this model is carried out by evaluating the effects of changing input parameters, as well as, providing guidance for obtaining relevant model inputs. Finally, an established parameter identification methodology is applied to demonstrate feasibility for estimating input parameters. The experimental data used to evaluate this higher fidelity material model are taken from a series of previous tests to measure and characterize the normal and shear stress-strain behavior of textile fabrics relevant to IADs.

Numerical Determination of Mechanical Properties for Flexible Material Systems. Material property data for IAD finite element simulations has historically been obtained experimentally. Data at several states of stress are absent in the current literature. The present investigation presents a novel method for numerically determining mechanical properties. Based on the properties of the individual fibers, data from literature is used to estimate the effective elastic constants of the yarn. A sub-scale section that captures the characteristic periodic pattern in the fabric (unit cell) is built. With the unit cell, various numerical tests can be performed. The effective nonlinear mechanical stiffness matrix can be obtained as a function of elemental strains through correlating the force-displacement results for a unit cell with a four node membrane element of the same size. The effective nonlinear elastic moduli can be incorporated into a traditional or a user defined material model associated with membrane elements for greater control of the input parameters. Numerically determined properties are validated for structures pertaining to the analysis of IADs.

CHAPTER II

APPLICATION OF PARAMETER IDENTIFICATION TO CURRENT EXPERIMENTAL MECHANICAL PROPERTY DETERMINATION METHODS

2.1   Introduction

Most engineering problems are posed for direct analysis, where a physical phenomenon is studied using an analytical model. Model parameters and boundary conditions are known and the goal is to compute the system response or model outputs. In the case of 4-point air beam bending response modeling, the loading boundary conditions are known from experimentation and the parameters and material properties defining the material model are also known. The goal of 4-point air beam bending response modeling is to predict the load-deformation response by calculating variables such as wrinkling load and maximum applied load. This is an example of a direct problem.

If measurements of a systems response are available, the problem can be approached in an inverse fashion. For these problems, the objective is to estimate the model parameters or boundary conditions from measured outputs. In the case of 4-point air beam bending response modeling, measurement of applied loads and displacement in a few locations is available, and the goal is to accurately estimate model parameters and boundary conditions that result in a predicted system response that closely matches the data. In a broad range of engineering applications, this approach is referred to as inverse analysis.

For complex problems where parameters contribute to the uncertainty, a comprehensive framework is necessary to yield an accurate multi-parameter estimation. The results of the inverse estimation depend strongly on the range of measurements used

in the analysis, as well as the input parameters being estimated. It is vital that the measurement and parameter selections are performed intelligently prior to the inverse estimation. The framework developed here proposes guidelines on how to conduct the parameter estimation via three steps: Nominal Analysis, Sensitivity Analysis, and Inverse Analysis.

Nominal analysis examines the quality of the data and provides a comparison between the data and model predictions. This is analogous to the direct approaches historically used by the IAD community. The range of reliable measurements for inverse analysis is identified. Sensitivity analysis starts with a complete list of material and system parameters and down select to a smaller subset containing parameters of most importance. Sensitivity analysis is particularity important with the number of input parameters and computational cost are high. These steps provide a list of parameters to be estimated and the range of data is to be used in the estimation process. The final step is apply an inverse method to estimate the selected parameters from the given data.

This chapter utilizes LS-OPT and LS-DYNA within the parameter identification methodology. LS-OPT is a standalone design optimization package with an interface to LS-DYNA [65]. The analysis code LS-DYNA is a nonlinear finite element solver developed by the Livermore Software Technology Corporation that has been extensively used by industry and government entities to analyze textile structures such as airbags, pressure stabilized beams, and parachutes [66].

2.1.1 Nominal Analysis

Nominal analysis can be thought of as a direct analysis. The goal is to examine the quality of the data and perform a direct comparison between the data and nominal model predictions before proceeding with inverse analysis. Model and measurement errors can lead to inaccurate solution of the inverse problem and introduction of bias

errors in the estimated parameters. Nominal analysis is performed to identify such errors and determine the range of measurements that are reliable for inverse analysis by examining the test data and performing a direct comparison of predictions to test data. The objectives and steps of the nominal analysis are as follows:

- Examine the data quality to identity measurement errors, anomalies or sensor problems.

- Correct for measurement errors, if possible. If not, determine the appropriate range of the reliable data for inverse analysis.

- Compare the data to the predictions from the physical model based on nominal parameters.

- Examine the model fidelity by identifying where the data trends are fundamentally different from model predictions.

- Select the measurement range that will be used in the inverse analysis.

2.1.2 Sensitivity Analysis

Sensitivity analysis aims to describe how much model output values are affected by changes in model input values. As discussed earlier, both geometrical and material factors in woven fabrics can potentially affect the material response at macro level and have a contribution on test non-repeatability. The approach employed to accomplish these goals is probabilistic, and is accomplished with full factorial designs. The objective is to start with a complete list of material and system parameters and down select to a smaller subset containing parameters of most importance.

As an example, Komeili and Milani studied geometrical and material related uncertainty factors using two-level factorial designs [54]. In a two-level factorial design, each factor is allowed to take two levels (an upper and lower limit within its range of variation). Then all possible combinations of the factor levels are analyzed to find

the sensitivity of a pre-defined response to the factors and their interactions [67]. As an example, if the number of factors for a geometric sensitivity analysis is, n, 2^n finite element runs would be performed for the sensitivity analysis.

The individual effect of each factor (main effect) is defined as the change in the response by a change in the level of a factor. In two-level factorial designs, a main effect is calculated by the difference between average responses measured under two different levels of a given factor. It should be noted that the variation caused by the factor levels may be affected by the levels of other factors. In this case, it means there is an interaction between factors. The approach for calculating effects from interactions depends on the level of interactions (i.e., interaction between 3 or 4 factors) [67].

Two-level factorial design results are generally presented in the form of half-normal probability plots. The half-normal probability plot is a graphical technique used in full-factorial design of experiments (DOE) to differentiate between two groups of significant (important) and insignificant (unimportant) factors. In such plots, the absolute values of factor effects (defined for each factor as the absolute value of the difference between the average response at the upper level and the lower level of that factor) are plotted against expected values from a half-normal distribution. In some cases, the effects are adjusted using their standard errors to arrive at the Standardized Effects metric. Significant factors tend to be on the right side of the graph whereas insignificant factors almost lie on a straight line on the left side. Data on the horizontal axis are sorted by their magnitudes from left to right. In a practical sense, this means the factors falling on the left side of the graph cannot be used to vary the average response. From a theoretical standpoint, their low contributions could be on the same order as random noises in the given system or experiment. Thus, they follow a normal distribution near zero. It has been shown that using a half normal plot as opposed to a standard normal plot provides a more sensitive scale for detection of significant

factors [67].

Half-normal probability plots are a graphical technique and thus a subjective form of screening. From a quantitative point of view, for the interpretation of absolute values of main/interaction effects, the Lenth's Criterion is used to identify the significant factors in single-replication factorial designs [68]. The criterion is based on two metrics: the Margin of Error (ME), in Equation (13), and Pseudo Standard Error (PSE) as shown in Equation (14).

The following is a brief description of Lenth's method. Suppose there are m effects from factors and interactions (contrasts) in a factorial design and are referred to as $c_1,c_2,...,c_m$. Therefore, for a 2^k full factorial design, m = 2^k - 1. Lenth's method begins with an estimation of the variance of the smallest contrast.

$$ME = t_{\frac{\alpha}{2},d}PSE \tag{13}$$

where $t_{\frac{\alpha}{2},d}$ is the t-distribution with a significance level of α. In this case, α=0.05 and d=m/3 is the degree of freedom.

$$PSE = 1.5 \times median\big(|c_j|: |c_i| < 2.5s_0\big) \tag{14}$$

and

$$s_0 = 1.5 \times median\big(|c_j|\big) \tag{15}$$

Lenth showed that PSE can be used as a reasonable estimation of contrast variance when there are not many active (significant) effects. PSE can then be used to judge the significance of factors by comparing each factor effect to the margin of error (ME). Quantitatively, a factor is significant if the absolute value of its effect is larger than ME.

While the Analysis of Variance (ANOVA)) technique is a very popular method to assess the contribution of different regression terms, Sobol's Global Sensitivity

Analysis (GSA) is widely used to study the importance of different variables for higher order models [65]. The Sobol's indices are a generally applicable non-linear sensitivity measure. The determination is computationally expensive because many sampling points are required. To overcome this problem, the indices can be based on metamodels. In LS-OPT, the metamodels give an approximation of the response function attributed to the variables.

In this method, a function is decomposed into sub-functions of different variables such that the mean of each sub-function is zero and each variable contribution only appears once. Then, the variance of each sub-region represents the variance of the function with respect to that variable contribution. Based on the evaluation of the metamodels, the Sobol's indice, S_i, of variable v_i is computed as shown in Equation (16).

$$S_i = \frac{variance\ caused\ by\ v_i}{total\ variance\ of\ response} \tag{16}$$

As shown in Equation (17), the sum of all Sobol's indices of one response is 1:

$$\sum_{i=1}^{n} S_i = 1 \tag{17}$$

where n is the number of variables. The theory of Sobol's GSA method is described in more detail in [65].

2.1.3 Inverse Analysis

Parameter and system identification or estimation has been applied in many fields. More narrowly, material identification has been used by various researchers to characterize materials used in structural analysis. Different optimization methods have been applied to minimize the resulting non-linear distance function. Yao et al. uses a genetic algorithm to minimize the residual in a nonlinear Parameter Estimation via Genetic Algorithm (PEGA) approach [69]. Seibert et al. use a modified random

search algorithm in the identification of viscoplastic material models [70]. Li and Roberts have applied Extended Kalman filters to the problem [71, 72]. Rikards et al. employ experimental design techniques to identify the plastic properties of polymers and the elastic properties of laminated composites [73, 74, 75]. Kok et al. applied the BFGS algorithm with design sensitivity analysis (DSA) gradients to identify the parameters of a temperature and rate-dependent viscoplastic polycrystal model [76]. Mullerschn et al applied the response surface methodology to the optimization of material parameters for rate dependent foam materials [77]. LS-OPT was also used in that study.
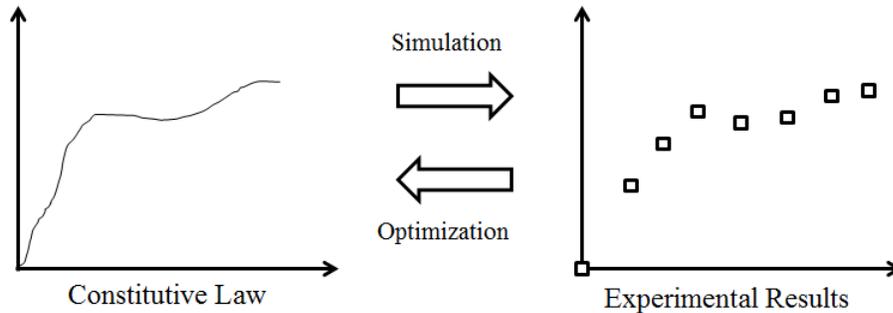
Figure 22: Material Identification Process

The process is shown schematically in Figure 22. The material constitutive relationship on the left typically involves different quantities than the experimental results on the right. The material constitutive law is a point-wise relationship valid at all points in the structural continuum while the experimental results are discrete values of response quantities, typically as a function of time or deformation. The arrows represent both simulation (forward) and optimization (backward) processes to be performed to match the two curve sets. Multiple load configurations or geometries, involving the same material, can be introduced resulting in the multiple cases being defined for the same optimization run.

The diagram in Figure 23 shows the methodology for deriving material properties from experimental results in LS-OPT. Definitions are required for each of the

steps in the flowchart. **Setup** refers to the setting of initial input parameter values and ranges. **Sampling** refers to selection of metamodel type and point selection method. **Analysis** refers to the finite element simulation using selected input parameters. **Metamodels** refers to the building of a response surface using the simulation results. **Composites** refers to the comparison between response surfaces and test data to construct the objective function. **Global Sensitivties** assesses the contribution of different regression terms to variance of the response. **Optimization** refers to the optimization of the objective function with respect to the input parameters. **Termination Criteria** is defined to assess model convergence. **Domain Reduction** is employed to accelerate convergence. If termination criteria is satisfied using metamodel results, a **Verification** simulation assesses metamodel accuracy.

To summarize the above definitions: A set of designs are selected from the set of input parameters. The simulation results obtained for the selected designs are used to build a response surface. The response surface is compared to the experimental data and the composite is used as the objective function to be minimized. If defined termination criteria are met, a verification simulation is carried out using the optimal set of designs from the metamodel. If not, the domain may or may not be reduced in size or shifted for the next iteration.

2.1.4 Mean Square Error

Depending on the application for which the material identification is required, the formulation used in the optimization is adjusted accordingly. The two best known approaches are the minimization of the maximum residual and the minimization of a residual norm constructed from the Least Squares Residual (LSR) or RMS error. The formulation utilized in this work, shown in Equation (18), is a variation of the second called the Mean Square Error (MSE) approach:
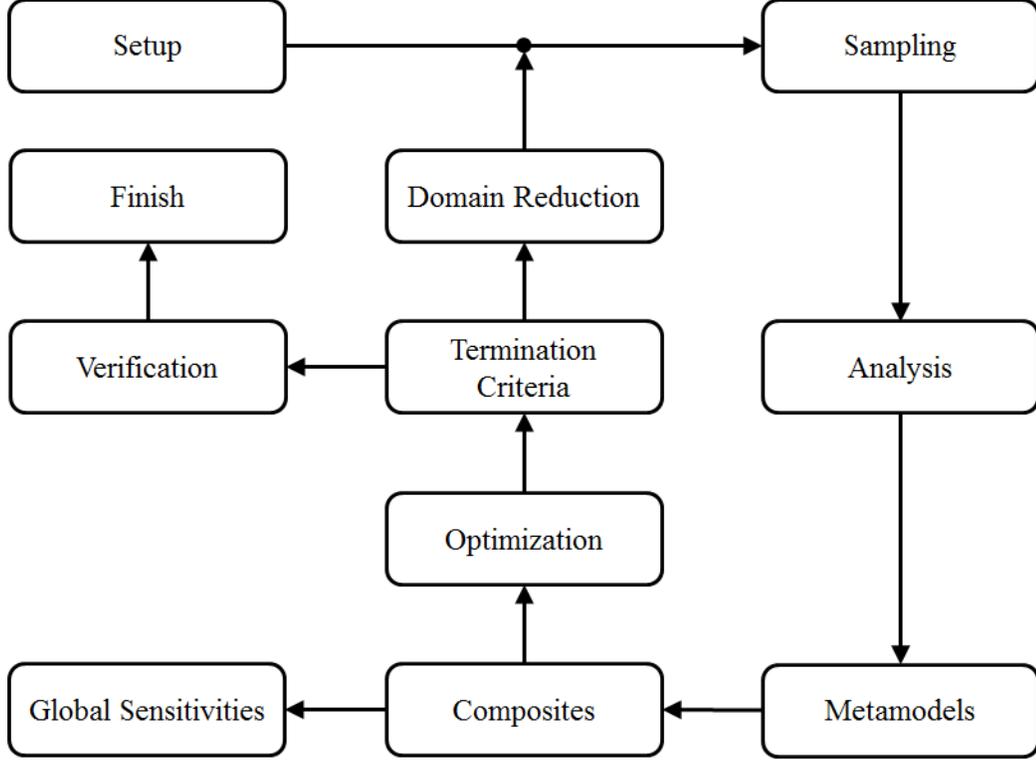
Figure 23: Single Case Parameter Identification Process Flowchart

$$MSE(\bar{x}) = \frac{1}{P} \sum_{i=1}^{P} W_i \left[\frac{f_i(\bar{x}) - G_i}{s_i} \right]^2 \rightarrow \min \qquad (18)$$

where P represents the number of responses constituting the residual, W_i and s_i are scaling factors required for weighting and normalization of each response respectively. $f_i(x)$ and G_i are the simulated response curve of variable vector x and the target curve, respectively. Figure 24 shows a graph containing the curve $f(x, z)$ and points $G_i(z)$. The points can be connected together to form a curve $G(z)$. As stated above, f is a computed response curve at a point x in the parameter space. System or material constants are typical parameters used in constructing finite element models. The independent state variable z can represent time, but also may represent any response type such as strain or deformation. The target curve G is constant with respect to x and most often represents test results.

In this work, the residual is constructed as a composite, using a response surface
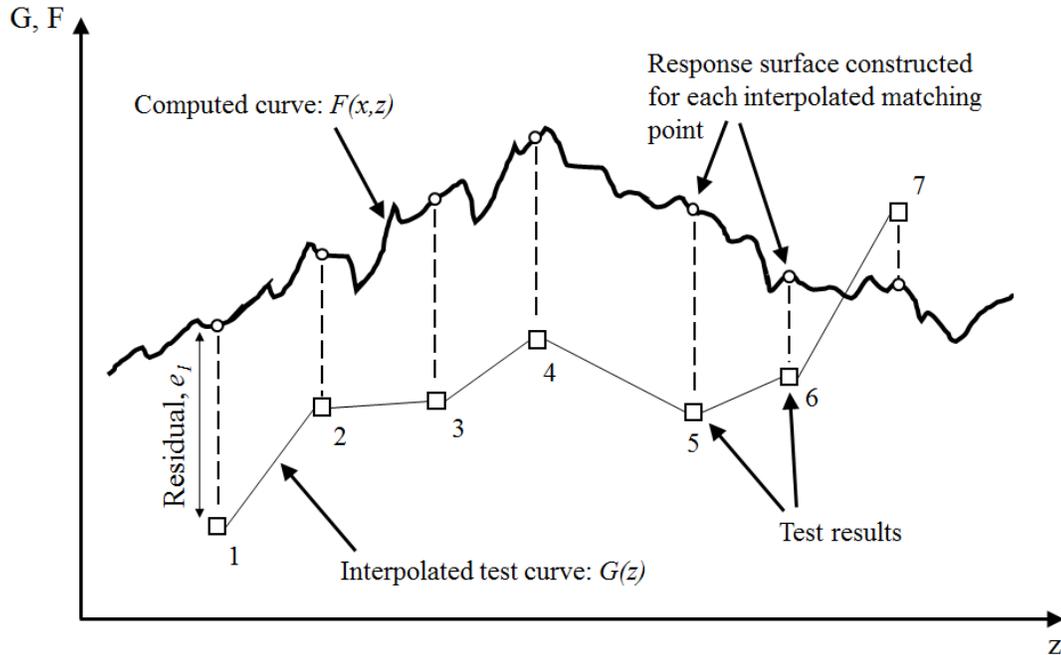
Figure 24: Components of Mean Square Error Formulation

for each $f_i(x)$. For the MSE approach an unconstrained minimization problem can be solved unless other constraints related to e.g. monotonicity in the curves to be matched are prescribed. Stander et al adds these constraints where optimization was used for airbag system identification [78].

2.1.5 Curve Mapping

A major difficulty in the use of ordinate-based curve matching is that steep parts of the curve are often difficult to match. Failure models typically have steep declines in the stress-strain curve toward the end, while most of the leading part of the curve is linear. This presents a strong case for the incorporation of abscissa into the curve matching metric.

Another problem with ordinate-based matching is that some points of the computed and target curves do not coincide horizontally such that some of the points are ignored. It is even possible that in portions of the optimization there is not a single vertical line which can will cross both the computed and target curves. This type of

problem can cause instabilities in the computation because its impossible to quantify the error.

Hysteretic curves (curves with more than one possible y value for some of the x values) cannot be quantified due to the non-uniqueness of the ordinate values of the computed cure with respect to the target curve. A logical approach for comparison of the two curves is to map one of the curves onto the other. The questions of how to scale the curves and how to match two curves of unequal length immediately arise. Scaling can be particularly important since scale changes have an effect on the distances between the two curves. In many cases, such as stress vs. strain, there may be several orders of magnitude difference between the values on the abscissa and ordinate.

As stated above, this work utilizes the MSE approach as a curve matching metric. The above comments should be considered however when setting up future problems. For a more detailed discussing on the use of curve mapping for parameter identification, refer to the work of Witowski and Stander [79].

2.2 *Silicone Coated Plain Woven Kevlar® Test Case*

There have been several recent efforts to characterize the mechanical properties of a variety of coated woven fabrics intended for IAD systems [15, 25, 26]. The results have provided a large database of experimental results from which to extract trends. The current work focuses on a silicone coated plain weave Kevlar® fabric from Lin et al. [25], which was selected as a good example. The details of the Kevlar® sample are provided in Tables 1 and 2.

The material used is this work is a 200 denier Plain Woven Silicone coated Kevlar®. The Kevlar® material was the same type used on the IRVE II flight article in the structural bladder skin. The following sections discuss details of the fabric architecture as well as the test methods used to characterize material. Discussion

related to the test methods includes observations regarding the trends in experimental data and analytical relations commonly used to convert load-deformation into stress-strain data. A more detailed discussion regarding the uniaxial tension and trellis-frame test data reduction is presented in Appendix B.

2.2.1 Material Description

The Kevlar® material is a plain woven fabric that is 200 denier. As discussed earlier, denier is the weight in grams of a 9000 meter length of fiber. The thread count or threads per inch (TPI) is a measure of the coarseness or fineness of a fabric. It is measured by counting the number of threads contained in on square inch of fabric, including both the warp and weft yarns. The terms ends per inch (EPI) and picks per inch (PPI) refer to the warp and weft threads per inch of woven fabric, respectively. The Kevlar® material was primed with a silicone infused solution to promote adhesion and then calendared with a Dow Corning Silicone Rubber. The calendaring process presses the rubber into the fabric filling the discontinuities under extreme load. A summary of the fabric properties before and after coating is provided in Table 1

Table 1: Properties of Silicone Coated Plain Woven Kevlar® Fabric

Denier	TPI	Uncoated Areal Density (oz/yd^2)	Coated Areal Density (oz/yd^2)	Uncoated Thickness (in)	Coated Thickness (in)
200	40 x 40	2.1	8.0	0.005	0.008

For modeling purposes, it is necessary to know the density of the fabric and not just that of the fiber. Density calculation for all samples were made using a Mettler Density Determination Kit, ME-33360 [25]. The process is essentially density measurement by hydrostatic weighing. Reference [25] a more detailed explanation of the density determination process as well as a summary of all fabric densities for the materials characterized in that study. A summary of fiber and fabric densities for all the 200 denier kevlar® fabric is provided in Table 2. As would be expected, the fabric

density which includes the coating and discontinuities is less than the fiber density.

Table 2: Silicone Coated Plain Woven Kevlar® Fabric Density

Fiber Density (g/cm^3)	Yarn Density $(yarns/in)$	Coating Add-on (oz/yd^2)	Mean Fabric Density (g/cm^3)
1.44	40 x 40	5.9	1.1099

2.2.2 Test Methods

The experimental test program discussed in Reference [25] used four different test methods to measure and characterize the normal stress-strain and shear stress-strain behavior of textile materials for IADs. Two of the test methods, specifically the uniaxial and biaxial cylinder tests, were used in Hutchings work [26]. ILC added the capability of photogrammetry to capture additional data for comparison and correlation. In addition, the trellis-frame and bias extension tests for shear behavior were modified to include photogrammetry capability for comparison and correlation with the biaxial cylinder test method. The purpose of using multiple test methods to gather shear stress-strain behavior was to aid in the determination of which method is best suited for future wind tunnel test correlation.

The uniaxial, trellis-frame, bias-extension tests were performed using an Instron test machine, model number 1125. Calibration data showed the machine results to be within ±0.2%. Extensometers were used during testing, but data is not used in this work as only the load cell and crosshead extension data is necessary. For more detailed information regarding the specifics related to the test procedures, the reader is referred to the ILC paper and the ASTM standards that work references.

This work utilizes test data from all of the available normal and shear methods reported in Reference [25], however the trellis-frame test will not be modeled. The uniaxial and bias extension tests are modeled and used in the parameter identification methodology. The inflated cylinder test is modeled for purposes of comparing

55

the material properties obtained from parameter identification to the experimental inflated cylinder data at multiple inflation pressures.

2.2.3 Normal Stress-Strain

The uniaxial tension test is one of the most common test methods for determining the normal stress-strain characteristics of textile materials. Reference [25] utilizes the Strip Method as described by ASTM D5035-06. In the strip tensile test, a narrow strip of fabric, 3 in wide by 6 in long, is used. Since the stress-strain behavior of a textile are usually different in the orthogonal warp and weft fiber directions, two sets of test samples were prepared for the test method. One set of samples has the warp fibers running parallel to the axis of load application, while the second set of samples has the weft fibers running parallel to the axis of load application as shown in Figure 25.
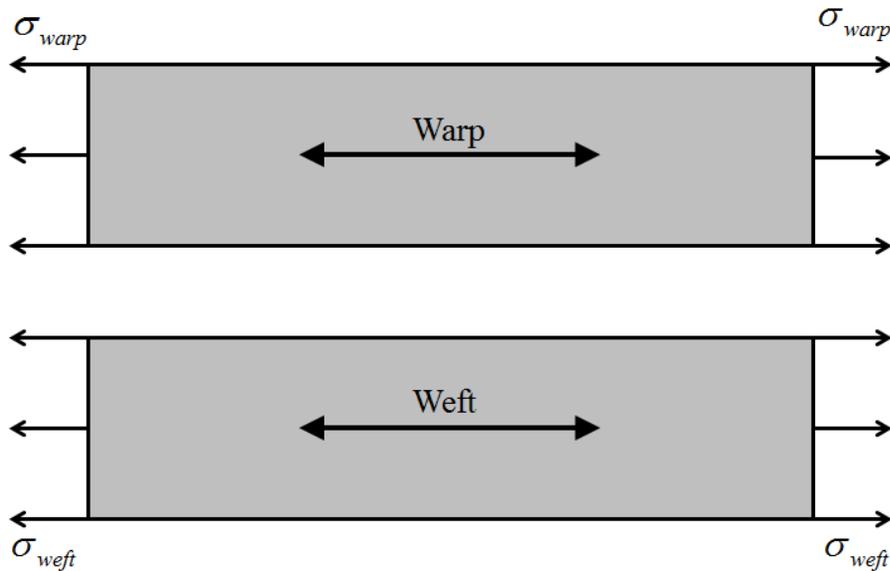
Figure 25: Textile Uniaxial Stress-Strain

The uniaxial tension tests in the 200 denier Kevlar® warp and weft directions measured load-deformation for the load interval [0,2500 N]. That data was used to calculate normal stress-strain for the stress interval [0,32.2 N/mm]. Units of stress

were reported in units of load per unit length. The fabric thickness was removed from the calculation. It is typical for fabric experimental data to be reported in these units. The thickness for the 200 denier fabric is reported in Table 2. The experimental data from uniaxial loading over ten cycles exhibit appreciable hysteresis, as well as, a wandering or strain set between cycles. The amount of wandering between cycles appears to decrease as the cycle number increases. The strain set was observed to be approximately 20% of the strain maximum for the first load cycle. Neglecting the impact of strain set, the slopes for the tenth load cycle were very similar to those of the first. Figure 26 shows all ten warp and weft direction load vs extension cycles for one of the samples tested.
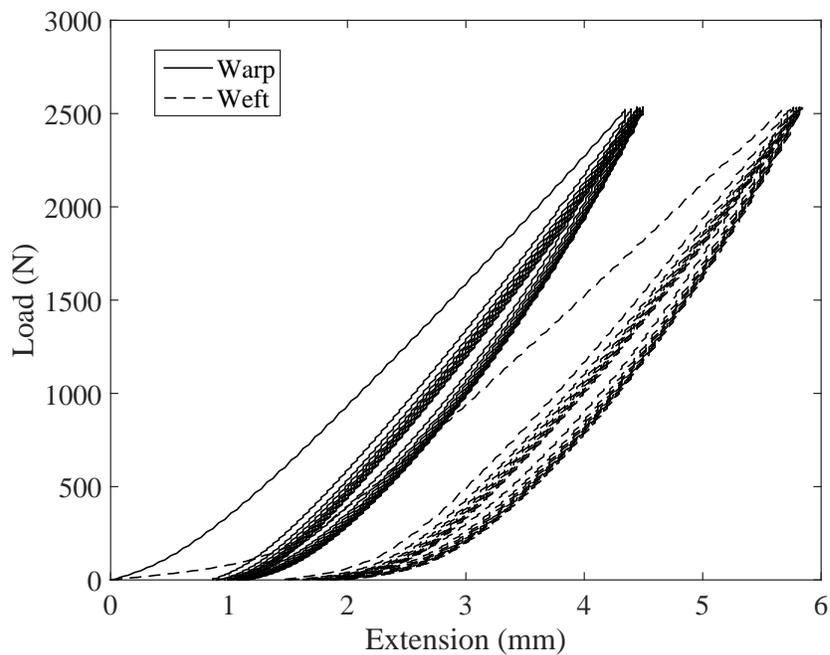
Figure 26: 200 Denier Kevlar® Warp and Weft Uniaxial Tension Test - All Ten Cycles

Consider an idealized uniaxial loading hysteresis cycle as shown in Figure 27. At the peak of the load cycle, the crosshead is held fixed for a brief period of time. During this period, the stress of fabric relaxes without minimal changes in strain. At the bottom of the load cycle, the residual strain in the fabric relaxes with minimal

changes in stress. Thus, the observed hysteresis is caused by this relaxation process. If the timescale of the relaxation process is greater than that of the pause at the peaks of the load and unload cycles, there is an observed wandering of the response.
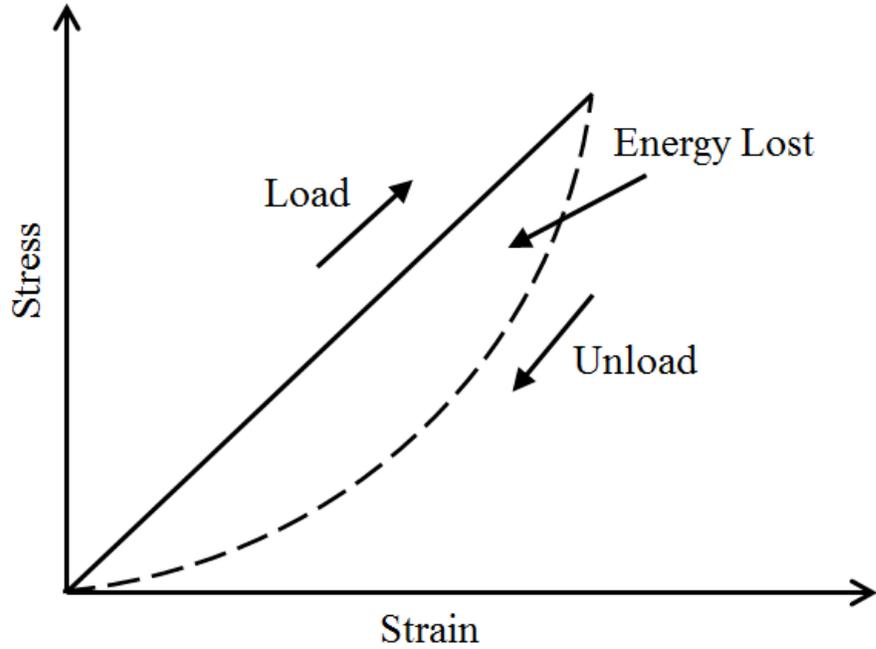
Figure 27: Idealized Uniaxial Loading Hysteresis Cycle

Hysteresis has been modeled using rate dependent damping terms in past studies. However, the low crosshead speed used for experimental testing prevents the replication of the observed hysteresis using plausible values of damping coefficient. It is difficult to model hysteresis using a modification to stiffness or damping matrices as there is no increment in strain (or strain rate) present to alter the stress during load relaxation. Murman et al. implemented an inertial lag technique that is consistent with the physics of the fabric [39]. In solid specimens, the load is essentially transferred instantaneously throughout the entire specimen. In fabrics, the loading in the different regions can lead or lag due to local yarn and coating stretching. Murmans technique was implemented as a user defined forcing function in LS-DYNA and scaled with sample size, thus implying that the hysteresis would be present at flight scale.

Williams modeled hysteresis using a method that considered energy dissipation and residual friction [80]. As discussed earlier, the initial load-deformation behavior results from inter-fiber friction, inter-yarn friction, and yarn decrimping which results in relatively high elongation and small tensile stress. After the yarn lock occurs, the rest of the behavior is dominated by the mechanical properties of the constituents. The recovery of the fabric as it is unloaded exhibits hysteresis due to energy dissipation and residual friction between fibers and yarns. In this context, hysteresis is defined as the permanent strain set resulting from the loading history.

The MAT_FABRIC material model within LS-DYNA includes the capability to model hysteresis. The model allows the input of load curves that define stress vs uniaxial strain along both fiber directions. Optional unload and reload curves are available for specific element formulations. An optional reloading parameter (RL) may be defined with values between 0 (reloading on the unload curve) and 1 (reloading on a minimum linear slope between unloading curve and loading curve). In addition, an optional hysteresis parameter (H) defines the fraction of dissipated energy during a load cycle in terms of the maximum possible dissipated energy. The normalized hysteresis parameter can also be varied between 0 and 1. Varying these parameters until the finite element model matches experimental data provides a means of modeling hysteresis.

The scope of this work has been defined around air inflated fabric structures and specifically IADs. As discussed in Chapter 1, many IAD designs contain purely biaxially loaded structures, such as inflated toroids and pre-tensioned gores that are not largely cyclically load. In these cases, it is possible to simplify the modeling approach to neglect the nonlinear crimp interchange region. With most modeling approaches assigning the cause of hysteretic behavior to the yarn decrimping and friction, it is assumed that hysteresis is not a significant factor within the scope of this work and is neglected.

2.2.4 Shear Stress-Strain

Several approaches have been developed and used by industry and academia to characterize the shear stress-strain behavior of textile materials. This section provides a detailed description of the bias-extension, trellis frame, inflated cylinder test methods. Underlying theories and experimental test data are discussed.

2.2.4.1 Bias-Extension

As load is applied to the sample, three distinct zones occur that contain different deformation modes as shown in Figure 28 [42]. At the top and bottom in zone A, near the grips, little to no deformation occurs. Zone B, which surrounds the center region, is a transition zone where a mixture of shearing and extension occurs. Zone C, contains mainly shear deformation. This is the zone from which the measurements are taken.
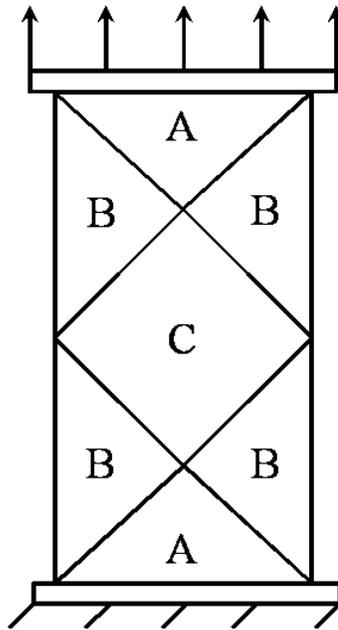
Figure 28: Bias Extension Deformation Zones

Kilby provides an empirical equation using the bias-extension test, uniaxial tension tests in the warp and weft directions, and Poisson's ratios to estimate the shear

60

modulus using Equation (11) [42], but this linear approximation has yet to be verified over multiple data sets. The data reported for the Bias Extension test is usually load and crosshead extension rather than shear stress and strain. The cross head is converted to shear strain by taking advantage of the pure shear that occurs in the sample shown in Figure 28. The shear angle, (γ), is defined in Equation (19).

$$\gamma = \frac{\pi}{2} - 2\phi = \frac{\pi}{2} - 2cos^{-1}\left[cos\phi_0 + \frac{\delta}{2cos\phi_0(H - W)}\right] \tag{19}$$

In the Equation (19), H = sample height, W = sample width, δ = displacement, and ϕ_0 is the initial half angle that the top corner Zone C makes with the vertical. ϕ_0 is usually assumed to equal 45°.

2.2.4.2   Trellis Frame

The objective of the trellis-frame test, shown in Figures 13 and 29, is to measure the in-plane shear stress-strain response by using a trellis-frame or picture frame apparatus actuated by an Instron testing machine.
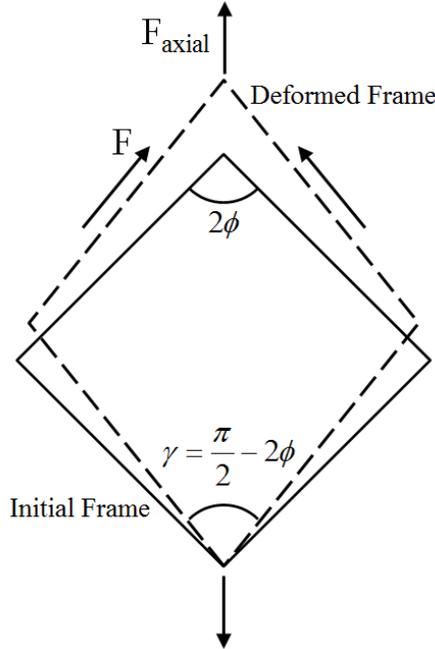
Figure 29: Trellis Frame - Shear Modulus Estimation

The trellis-frame consists of four pinned corners and four clamped edges. The clamped edges secure the cross shaped fabric in the frame without slippage. During the testing process, the distance between the top and bottom corners of the frame is changed by the Instron machine. This change reorients the yarns in the samples in a shearing motion. The Instron load cell and cross-head displacement measurements were recorded for several cycles and photogrammetry pictures were taken at specified conditions. A discussion of the trellis-frame test data reduction is presented in Appendix B.

2.2.4.3 Inflated Cylinder

In the inflated cylinder torsion test, the torque vs. twist angle is measured for an inflated cylinder as shown in Figure 30. One end cap has a free rotational degree of freedom and the other end cap has a free axial degree of freedom.
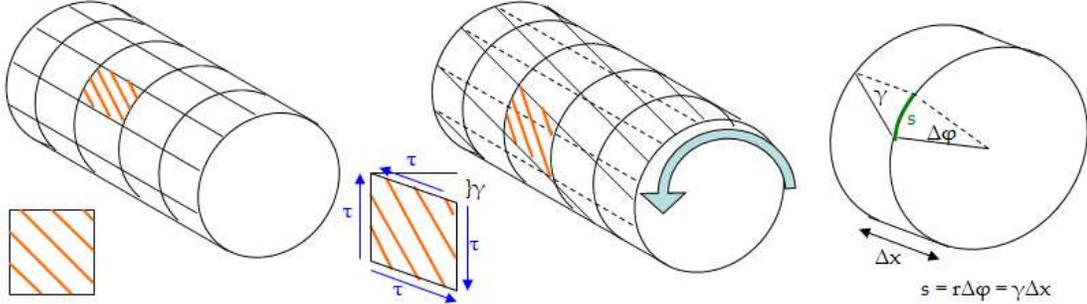
Figure 30: Inflated Cylinder - Shear Modulus Estimation [26]

Using well known relations from mechanics of materials, the applied torque is converted to the resulting shear stress and the twist angle is converted into shear strain. Applied torque is converted into shear stress using Equation (20).

$$\tau = \frac{Tr}{J} \tag{20}$$

where T is the applied torque, r is the radius of the cylinder, and J is the polar moment of inertia. J is calculated using Equation (21) with t being the thickness of

the material.

$$J = 2\pi r^3 t \tag{21}$$

End cap rotation is converted into engineering shear strain using measurements of the cylinder circumference and length. The engineering shear strain was calculated using Equation (22).

$$\gamma = \frac{r\Delta\phi}{\Delta x} \tag{22}$$

where r is the radius of the cylinder, $\Delta\phi$ is the twist angle, and Δx is the length of the cylinder. This relation makes a small angle approximation. The shear modulus in Equation (23) is calculated by dividing the shear stress by the shear strain.

$$G = \frac{\tau}{\gamma} \tag{23}$$

2.3 Nominal Analysis

Nominal analysis can be thought of as direct analysis. The data quality is assessed by comparing the experimental test data directly with the nominal model predictions before proceeding to the inverse analysis. The following describes the geometric and material models, boundary and loading conditions, as well as nominal results.

2.3.1 Geometric Modeling

This section provides descriptions for the uniaxial and bias-extension finite element models. The samples tested experimentally are simply rectangular strips of fabric that are clamped on two ends and stretched to predetermined load levels. The first step in modeling the experimental testing is to build appropriate geometric models. Table 3 restates the full model dimensions for both the uniaxial tension and bias-extension cases.

Table 3: Uniaxial and Bias Extension Full Model Dimensions

Model	Length (mm)	Width (mm)	Thickness (mm)
Uniaxial	152.4	76.2	0.202
Bias-Extension	218.4	88.9	0.202

The diagram in Figure 31 shows the boundary conditions applied to a full model. Boundary conditions are the specified values of field variables (or related variables such as derivatives) on the boundaries of the field. In this case, these are displacement boundary conditions that constrain the model in such a manner as to be representative of the experimental set up. The geometric model is meshed with 4 node membrane elements. A mesh convergence study is presented later in this chapter. All of the nodes at the base or left of the model have displacement degrees of freedom (DOF) that are fixed or set to one. This approximates the clamping of the fabric at the base. At the other end of the model, the nodes are allowed to translate along the longitudinal or y-axis and fixed in the other two dofs. This approximates the clamping of the fabric on the right, while allowing for load to be applied in the y-axis. All rotational dofs are left free at both ends of the model.
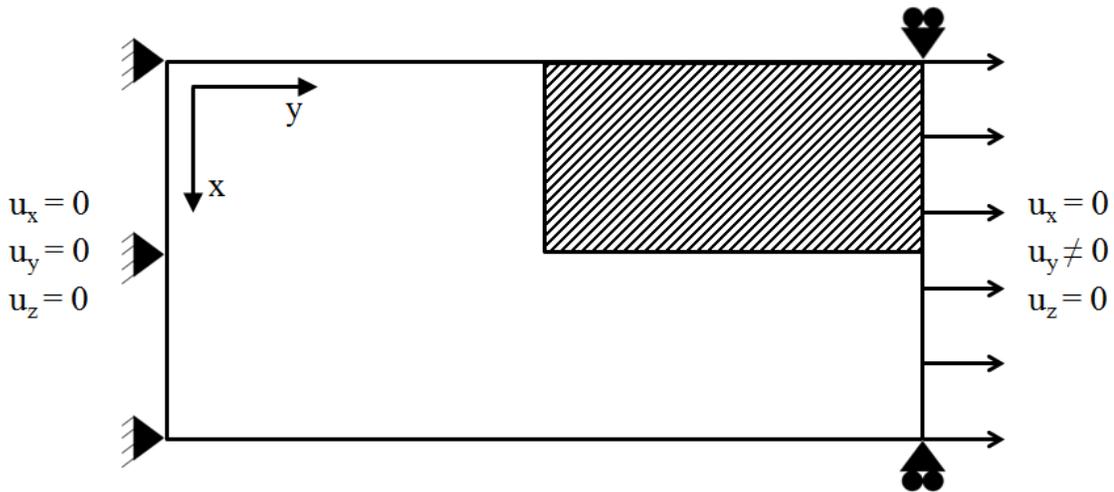
Figure 31: Full Model - Representative of Uniaxial Tension and Bias-Extension Tests

One method of efficiently using finite element modeling is to exploit the planes of symmetry of anti-symmetry. When symmetry is exploited, only a portion of the

actual structure is modeled in order to reduce the analysis run time and memory required. The lines or planes of symmetry or anti-symmetry in an FE model can be simulated by providing proper restraints to the symmetrical faces or edges. To model symmetry or anti-symmetry, the geometry and the restraints must be symmetric about a plane. The loads must be either symmetric or anti-symmetric.

For both the uniaxial tension and bias extension cases, there exists two planes of symmetry. Thus, only a quarter of the structure needs to be modeled and additional boundary conditions are added to simulated the symmetry planes. As shown by the shaded portion in Figure 31, a quarter section of the sample is modeled.

2.3.2 Material Modeling

All of the finite element analyses in this research use one of LS-DYNA's fabric material models (MAT_FABRIC or MAT_MICROMECHANICS_DRY_FABRIC). This section utilizes MAT_FABRIC and the latter will be discussed in the next chapter. MAT_FABRIC is built option a layered orthotropic composite material model and is valid for 3 and 4 node shell elements only. The model obtains membrane behavior by eliminating bending stiffness and permitting the elimination of compressive stresses in the element. An optional liner, which acts as a separate isotropic linear elastic material, helps stabilize discontinuous behavior near zero stress conditions. The liner helps prevent collapsed elements and enhances the membrane's stability. The liner is not necessary for these types of tensile only analyses. The model invokes a special membrane element formulation that uses only one through thickness integration point, does not hourglass, and only experiences strain in two dimensions.

The fabric can be modeled as either isotropic or orthotropic with arbitrary fiber angles. This work utilizes the orthotropic material definition. Appendix B provides an explanation of how the experimental data were reduced to obtain an appropriate set of material properties. These material properties are restated in Table 4 for

convenience. This set of material properties was used for all nominal analysis within this chapter.

Table 4: Linear Elastic Orthotropic Material Properties

Property	Symbol	Value	Units
Density	ρ	1.101×10^{-9}	ton/mm^3
Thickness	h	0.202	mm
Young's Modulus, warp direction	E_a	8409.8	MPa
Young's Modulus, weft direction	E_b	7673.4	MPa
Poisson's Ratio	ν_{ab}	0.3	
Shear Modulus	G_{ab}	0.898	MPa

Only a summary of the MAT_FABRIC material model was provided. The reader is referred to the LS-DYNA material model user manual for a more thorough explanation of model theory and capabilities [66].

2.3.3 Boundary and Loading Conditions

A quarter symmetry model is used to model both the uniaxial tension and bias-extension tests. Different boundary and loading conditions must applied when choosing to model only a quarter of the model. As shown in Figure 32, the nodes on base or left of the quarter model are constrained to have zero displacement in the y and z directions. The x dof remains free to allow for any lateral contraction the may occur in the model. Along the boundary defined by the vertical symmetry plane (or bottom), all nodes are constrained to have zero displacement in the x and z directions. The constraint on the x direction maintains symmetry along that face. The constraint on the z direction is not necessary to achieve an accurate solution, but does help prevent unnecessary out of plane motion from occurring.

To simulate the load applied on the model, a prescribed nodal displacement is imposed on the top right side of the model. The displacement dofs are fixed in the x and z directions, but the y dof remains free. The prescribed nodal displacement of the nodes on the right are in the y direction. LS-DYNA calculates the required force to displace these nodes by the defined amount. When comparing the reaction
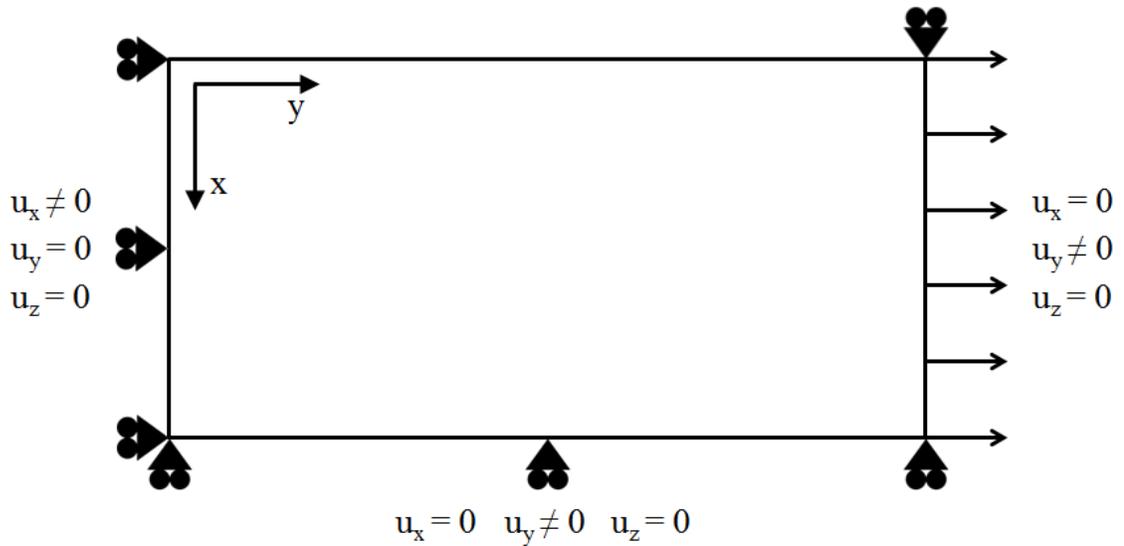
Figure 32: Quarter Symmetry Model - Representative of Uniaxial Tension and Bias-Extension Tests

forces from the quarter symmetry model to the experimentally obtained loads, the experimental loads must be divided by two to account for the symmetry conditions. All rotational dofs are left free along the boundaries of the model.

2.3.4 Convergence Study

In finite element modeling, a finer mesh often results in a more accurate solution. However, as the mesh is made finer, the computation time increases. It is then desirable to find a balance between accuracy and computational expense. One way to accomplish this goal is to perform a mesh convergence study.

The formal method of achieving mesh convergence requires a curve of a critical parameter in a specific location to be plotted against some measure of mesh density. It is common practice for at least three convergence runs to be required in order to generate a plot which can be used to indicate when convergence is achieved or how far off the most refined mesh is from full convergence. However, if two runs of different mesh density give the same result, convergence is typically assumed and no convergence curve is necessary.

As discussed in a previous section, when an idealized test sample shown in Figure 28 undergoes bias extension deformation, the sample can be divided into three regions of deformation. In Region A, the warp and weft have free yarn ends resulting in pure shear deformation in this zone. In Region B, one yarn direction is clamped at one end, the other direction is free at both ends. This region has half the shear deformation (half the shear angle) as compared to Region A. In Region C, the warp and weft yarns have clamped ends and there is no shear deformation in this zone. The complex deformation behavior of the bias-extension test requires a more refined finite element model mesh as compared to the uniaxial extension test. The following describes the bias-extension mesh convergence study and provides the selected mesh size for the remainder of the analyses.
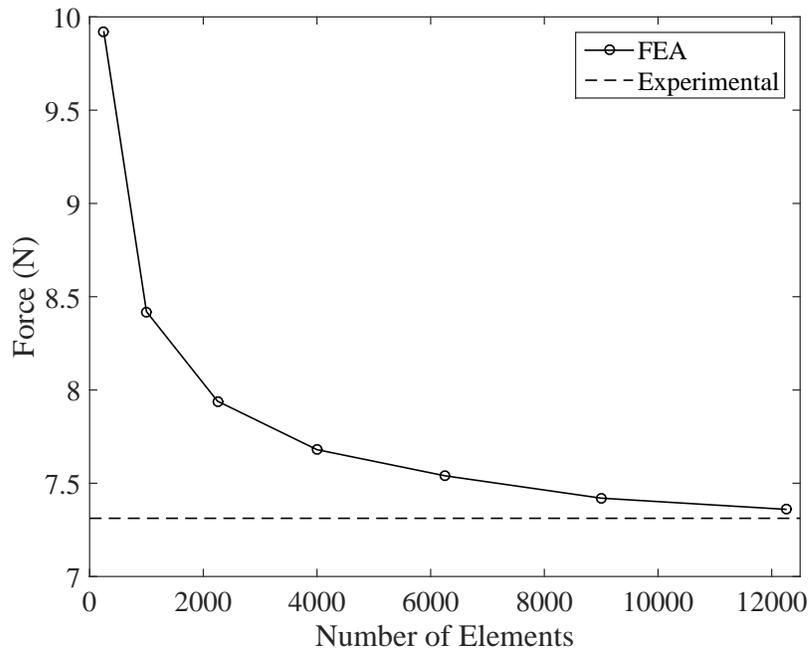
Figure 33: Applied Load (N) Vs Number of Elements

Two metrics were selected to assess the mesh convergence of the bias-extension model. The first metric is the resultant reaction forces at the boundary containing all the nodes fully constrained in translational dofs. This resultant force is compared

to experimental load cell force that has been divided by two. The model meshes were varied from a coarse 250 elements to a much finer 12250 elements. Figure 33 shows the convergence of the resulting reaction force as a function of the number of elements. The simulation is converging to the experimental value of approximately 7.3 N. Note that this value has been divided by two from the actual experimental value.

Quantifying what amount of error is allowable is beyond the scope of this work. With these simulations being unusually simple in the context of typical IAD finite element simulations, even the finest mesh of 12250 elements is only mildly computationally intensive. Table 5 shows the percent difference in the simulation and experimental forces as a function of element number. Over 99% of the reaction force is recovered using the highest number of elements. With approximately 33% the amount of elements, still 95% of the reaction can be recovered.

Table 5: Convergence Study, Bias Extension - Percent Difference in Reaction Force and Engineering Shear Strain

Element Number	Percent Difference Reaction Force	Percent Difference Engineering Shear Strain
250	35.7%	23.5%
4000	5.0%	10.9%
12250	0.7%	2.1%

The second metric is the engineering shear strain in the pure shear region of the model. Figure 34 shows the engineering shear strain along the centerline of the model for varying number of elements. The engineering shear strain in the elements bordering the y axis symmetry plane is plotted as a function of the element's position on along the length of the model. The simulation data is plotted along with two bounding regions, B_A and B_B. Region B_A defines the theoretical size of the full pure shear region. Region B_B defines a subset of B_A that does not border other surrounding regions. In reality, the deformation regions blend over into one another.

The shear strain of approximately 13.2^o calculated in these regions was obtained using experimental displacement measurements and Equation (19). It can be seen that the simulations are converging to the experimental data as the number of elements increases. In addition, the model is more accurate further away from the boundary conditions.
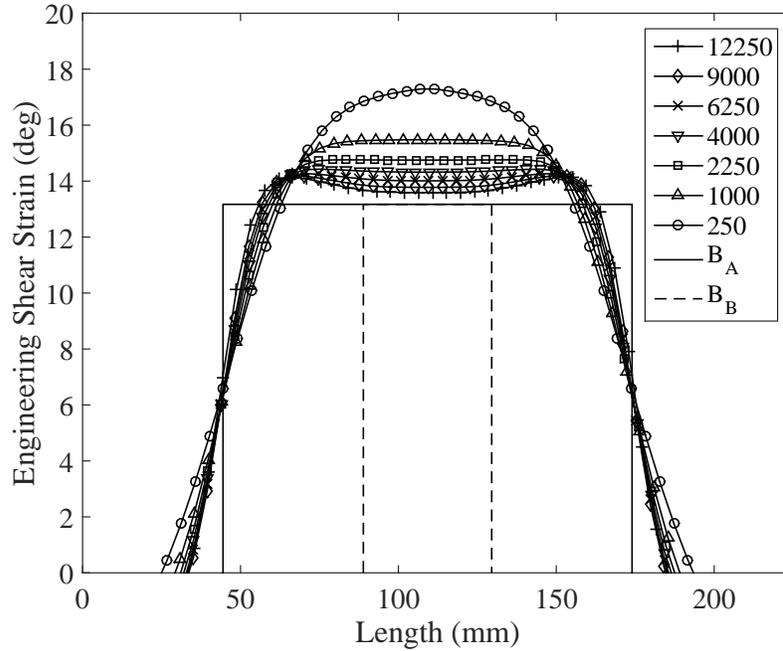
Figure 34: Engineering Shear Strain (deg) Vs Sample Length (mm)

The remaining simulations in this chapter use models containing 12250 four node membrane elements. The complex deformation behavior of the bias-extension test requires a more refined finite element model mesh as compared to the uniaxial extension test. As such, the bias-extension mesh size requirements are more strict that the uniaxial case. The same mesh size is used for all models, but it is noted that there is significant room to decrease the number of elements in the unaxial case. If 5% and 10.9% difference in loads and strain respectively are deemed acceptable in future work, a model with approximately 33% the number of elements could be used for the bias-extension case.

2.4 Inverse Analysis

The purpose of inverse analysis is to provide a better match between the data and LS-DYNA simulations through the estimation of certain input parameters. This is accomplished by minimizing the MSE objective function using the metamodel-based optimization method discussed in Chapter A. The parameter identification results will be compared with experimental results from the uniaxial tension and trellis-frame tests.

The set of parameters to be estimated for MAT_FABRIC is relatively small. From the discussion preceding the nominal analysis, E_a, E_b, ν_{ab}, and G_{ab} are selected. There are many options for the range of the data to be used in the parameter identification process and the variables that should be estimated. Since the list of variables is small in this case, all will be carried throughout the remaining analyses.

It is advantageous to find a method for setting initial parameter ranges that does not rely on a prori knowledge of the load-deformation behavior of the fabric. An estimate of the elastic modulus of a fabric can be estimated using the volume fraction of the fibers in the fabric for a given yarn direction as shown in Equation (24) [30]. This can be used as a quick reality check for measured values. This estimate has been shown to consistently over estimate the actual values due to the exclusion of yarn crimp from the equation and thus provides a good estimate for the upper bound on the design space for elastic modulus when the longitudinal tensile modulus of the fiber is used in the equation. An estimate for the lower bound on the design space can be found be using the transverse tensile modulus of the fiber in the equation. The mechanical properties of the Kevlar® 29 fiber used to construct the 200 denier fabric are not available so representative estimates are utilized. Estimates for the mechanical properties of Kevlar® 29 fibers were obtained from an online educational database.

$$E_{fabric} \simeq \frac{V_{fiber}}{V_{fabric}} E_{fiber} \tag{24}$$

Of the test data available for the 200 denier Kevlar® fabric, fiber volume fraction was not measured. However, the density (mass per unit volume) and areal density (mass per unit area) of the fibers, coating, and fabric were measured and can be used to estimate volume fraction as shown in Equation (25). As the mass ratio between the fiber and fabric was not available, the areal density is used to approximate that ratio by assuming that the fibers and fabric occupy equal areas. This approximation improves when there is less coating in between individual yarns as well as when the yarns are tightly packed.

$$\frac{V_{fiber}}{V_{fabric}} \simeq \left(\frac{\rho_{fabric}}{\rho_{fiber}} \right) \left(\frac{\rho_{Afiber}}{\rho_{Afiber} + \rho_{Acoating}} \right) \tag{25}$$

As discussed in Section 1.4.1, the initial shear response of a coated plain woven fabric is dominated by the coating and with increased shearing, the behavior transitions to that of an uncoated fabric. Since this analysis utilizes a linear elastic shear modulus, the shear load-deformation data is limited to the lower strain values dominated by the coating. The data in this region is approximately linear as shown in Appendix B. The mechanical properties of the silicone rubber used to coat the 200 denier fabric are not available so representative estimates are utilized. The upper and lower bounds on the design space are estimated based on ranges for shear modulus of the silicone rubber coating referenced in an online educational database.

During uniaxial loading, lateral contraction of the fabric is observed that is similar to the Poisson effect from solid mechanics. The ratio of lateral to axial strain, ν_{ab}, was measured for the 200 denier Kevlar® fabric in both the warp and weft directions [25]. The observed value of effective Poisson's ratio from these tests exceed unity, which is inconsistent with typical isotropic and orthotropic material models. For numerical stability reasons in orthotropic models, it is common in practice to limit Poisson's

ratio to significantly lower values than unity. Murman showed that the complete lateral contraction response under uniaxial loading cannot be replicated using a homogeneous FEM approximation [39]. As discussed earlier, the lateral contraction in the fabric is caused by the crimp interchange seen at the low load levels in uniaxial tension. It has also been noted that crimp interchange can be neglected in cases of biaxial loading like that of air inflated fabric structures. Therefore, it is appropriate to assume that $\nu_{ab} \approx 0$. To investigate this however, ν_{ab} is left as a parameter in this study and upper and lower bounds are set to a reasonable range of $[0,0.4]$.

Table 6: Initial Values and Lower and Upper Design Space Bounds for Parameters

Name	Starting	Minimum	Maximum
E_a	6596	850	12342
E_b	6596	850	12342
ν_{ab}	0.2	0	0.4
G_{ab}	1.65	0.3	3.0

Table 6 lists the initial values for each variable as well as the upper and lower bounds for the initial design space. The sources for estimates on the ranges for all parameters was discussed above. The initial values were obtained by taking the average of the upper and lower bounds on the design space.

The diagram in Figure 35 shows the parameter identification methodology with three separate cases to be optimized simultaneously. A set of designs are selected from the set of input parameters. The simulation results obtained for the selected designs are used to build response surfaces. The response surfaces are compared to the experimental data and the composite MSE is used as the objective function to be minimized. If defined termination criteria are met, a verification simulation is carried out using the optimal set of designs from the metamodel. If not, the domain may or may not be reduced in size or shifted for the next iteration.

After the initial parameter values and ranges are defined, polynomials are selected to construct the metamodels. Experimental design is the selection procedure for
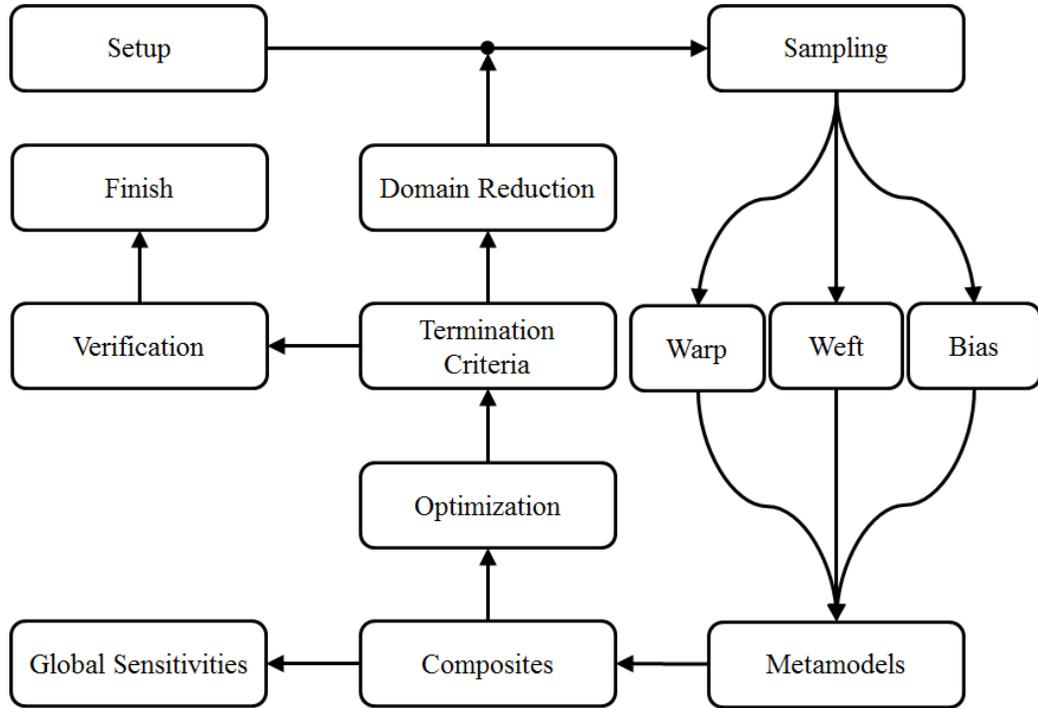
Figure 35: Multiple Case Parameter Identification Process Flowchart

finding the points in the design space that are to be analyzed. The D-optimal method is utilized. The experiments are selected within a sub-region in the design space thought to contain the optimum. For the 4 parameters to be estimated, the number of D-optimal designs is 8 per iteration per case.

Three separate LS-DYNA simulations are run simultaneously. The number and type of parameters that can be estimated are based on available data. The differences in the simulations are in the geometry and material axes orientations. The 1st simulation corresponds to the bias-extension model which has different dimensions than the models for the the remaining two simulations. The 2nd and 3rd simulations correspond to loading in the warp and weft directions. The material axes are rotated about the element normal to achieve the desired orientation. The material coordinate system is defined by specifying an angle, β, relative to the local element coordinate system. The material axes are rotated by [-45°,45°] from the local element coordinate system for the bias-extension model, [0°,90°] for the weft model, and [90°,0°] for the

warp model. Appendix B discusses the specifics of how the material axes are rotated.

The computed and interpolated test curves are used to calculate the MSE. Experimental force-displacement curves are input into the simulation with pre-processing to account for the use of symmetry in the finite element models. In order to construct the corresponding simulation force-displacement curves, the $SECFORC$ and $NODOUT$ database keywords are implemented for each model. The $SECFORC$ card is setup to output the sum of resultant forces for all the nodes at the fully constrained end of the model. The $NODOUT$ card is setup to output the y component of the displacement vector for a defined node at the opposite end in each model.

In this work, the residual is constructed as a composite, using a response surface for each $f_i(x)$. For the MSE approach an unconstrained minimization problem can be solved. The objective function is defined in Equation (26) as the mean square error for each of the three cases.

$$MSE(\bar{x})_{total} = MSE(\bar{x})_{warp} + MSE(\bar{x})_{weft} + MSE(\bar{x})_{bias} \qquad (26)$$

In LS-OPT, global sensitivities are evaluated on the metamodels, Therefore the accuracy depends on the quality of the metamodel. Unless a subregion is specified, the sensitivities are calculated for the global bounds of the variables. Sampling constraints are not considered while calculating the sensitivities. The composite expressions and subregion sensitivities are always evaluated using the Monte-Carlo simulations. The typical number of sampling points for Monte-Carlo simulations is 10,000. This number can be increased for better accuracy of sensitivity coefficients.

Depending on the optimization task and strategy, the LS-OPT allows the user to specify tolerances on the design change (Δx_i) and the objective function change (Δf_i). The user can specify if one or both termination criteria are to be met. The design change criteria termination shown in Equation (27) becomes active if,

$$\frac{||x^k - x^{k-1}||}{||d||} < \epsilon_x \tag{27}$$

where x refers to the vector of design variables and d is the size of the design space. The objective function termination criteria shown in Equation (28) becomes active if,

$$\left|\frac{f^k - f^{k-1}}{f^{k-1}}\right| < \epsilon_f \tag{28}$$

where f denotes the value of the objective function, (k) and $(k-1)$ refer to two successive iteration numbers. The termination criteria shown in Table 7 also includes a maximum number of optimization iterations. If the termination criteria described above are reached first, LS-OPT will terminate and not perform the maximum number of iterations.

Table 7: Termination Criteria and Domain Reduction Parameters

Description	Value
Design Change Tolerance	0.01
Objective Function Tolerance	0.01
Maximum Iteration Number	5
Proximity Zoom	0.6
Oscillation Contraction	0.6
Panning Contraction	1

To automate the successive sub-domain reduction scheme for the Sequential Response Surface Methodology (SRSM), the size of the region of interest (as defined by the range of each variable) is adapted based on the accuracy of the previous optimum as well as the occurrence of oscillation. The accuracy is estimated using the proximity of the predicted optimum of the current iteration to the starting (previous) design. The smaller the distance between the starting point and optimum designs, the more rapidly the region of interest will diminish in size. If the solution is on the bound of the region of interest, the optimal point is estimated to be beyond the region. Therefore, a new subregion, which is centered on the current point, does not change size. This is

called *panning*. If the optimum point coincides with the previous one, the subregion is stationary, but reduces in size by *zooming*. Both panning and zooming may occur simultaneously if there is partial movement. A *zoom parameter* is defined in LS-OPT by the user and is typically set to 0.6. Panning, zooming, and combinations of both are shown in Section A.2.2.2 in Figure A.1. A contraction parameter is determined based on whether the current and previous designs are on the opposite or same side of the region of interest. The *contraction parameter* is a function of two parameters and an *oscillation indicator*. The oscillation indicator is a function of the range of and distance between current and previous designs. The *oscillation parameter* and *panning parameter* are defined in LS-OPT by the user and are typically set to 0.6 and 1 respectively. A summary of the parameters discussed above is provided in Table 7.

After the last full iteration, a verification run of the predicted optimal design is executed. If only the predicted optimum from the metamodel is of interest, the verification run can be omitted.
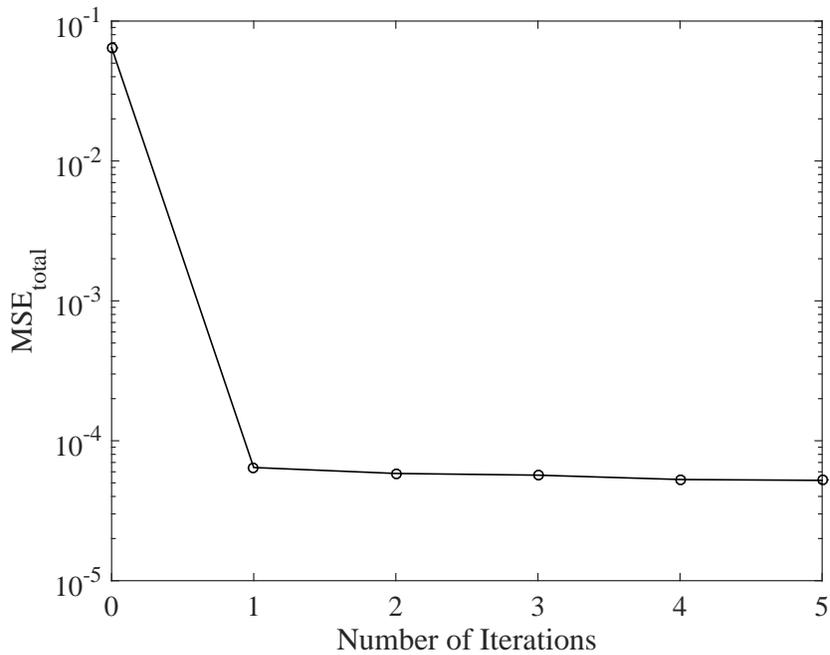
Figure 36: Total Mean Square Error Vs. Number of Iterations

As shown in Figure 36, the majority of the reduction in the objective function or MSE occurs during the first iteration. The objective function decreases by 99.9% after the first iteration and only 9.3% after the second iteration. Figure 36 shows the combined MSE for all three cases as the number of iterations progresses. The objective function changes on the order 1E-5 after the first iteration indicating that the default termination criteria of objective function changes less than 0.1 was set too high and should be set closer to 1E-6. Table 8 shows the optimization histories for all five iterations.

Table 8: Multi-Case Optimization Histories

Iteration	E_a	E_b	G_{ab}	ν_{ab}	MSE_{total}
0	6596.00	6596.00	1.65	0.20	6.460E-2
1	8410.74	7953.57	0.890	0.00	6.439E-5
2	8415.82	7965.36	0.887	0.00	5.839E-5
3	8424.59	7986.18	0.883	0.00	5.678E-5
4	8426.12	7985.61	0.878	0.00	5.286E-5
5	8426.15	7985.20	0.876	0.00	5.211E-5

Table 9 provides the 95% confidence intervals for individual optimal parameters. The larger confidence interval and low correlation of ν_{ab} to MSE can be explained by the insignificance of that parameter on the objective function. The final values are from the verification run and explains why they differ from those in Table 8.

Table 9: 95% Confidence Intervals for Individual Optimal Parameters

Name	Final	Lower	Upper
E_a	8403.4	7249.8	9557.0
E_b	7967.1	6860.1	9074.1
ν_{ab}	1.28e-6	-1.996	1.996
G_{ab}	0.886	0.744	1.028

Examining Table 10 provides insights about the effect of each input variable on the MSE and also the degree of correlation between the input parameters. There is high correlation between each input parameter and the corresponding MSE. This is expected as these experimental tests were design to isolate their respective material

input parameter. It should be noted that the correlation trends observed here are case dependent and the analysis has to be repeated for other applications. As an example, if the material is an uncoated plain woven fabric and subjected to larger shear deformations, the shear behavior will be greatly influenced by yarns and will have higher correlation with the two elastic moduli.

Table 10: Correlation Coefficients Showing Linear Dependency Between Parameters and Composites

	E_a	E_b	ν_{ab}	G_{ab}	MSE_{bias}	MSE_{warp}	MSE_{weft}
E_a	1	0.30	0.16	0.30	0.22	**0.91**	0.35
E_b		1	0.28	0.34	0.43	0.39	**0.91**
G_{ab}			1	0.14	**0.85**	0.12	0.32
ν_{ab}				1	0.30	0.40	0.45
MSE_{bias}					1	0.26	0.55
MSE_{warp}						1	0.47
MSE_{weft}							1

Finally, it is worth making a comparison as shown in Table 11 between a few of the methods described thus far for estimating in-plane shear modulus. The trellis-frame test compares well with the results from LS-OPT and the bias-extension test. This is expected as the trellis-frame test has been a widely accepted method. Kilby's relationship shown in Equation (11) over-estimates the shear modulus. This equation is a linear approximation and has not be validated against several fabric architectures and coatings.

Table 11: Comparison of Three Methods for Estimating Shear Modulus

LS-OPT	Trellis-Frame	Kilby
0.886	0.898	1.461

2.5 Validation

In this study, an experimental data set from the inflated cylinder torsion test method to characterize the shear stress-strain behavior of textile materials is used to validate the above methodology for air-inflated structures. In the inflated cylinder torsion

79

test, torque versus twist angle is measured for an inflated cylinder where one end cap has a free rotational degree of freedom and the other end cap has a free axial degree of freedom. Using the well known relations from engineering mechanics discussed in Section 2.2.4.3, the applied torque can be converted to the resulting shear stress and the twist angle to shear strain.
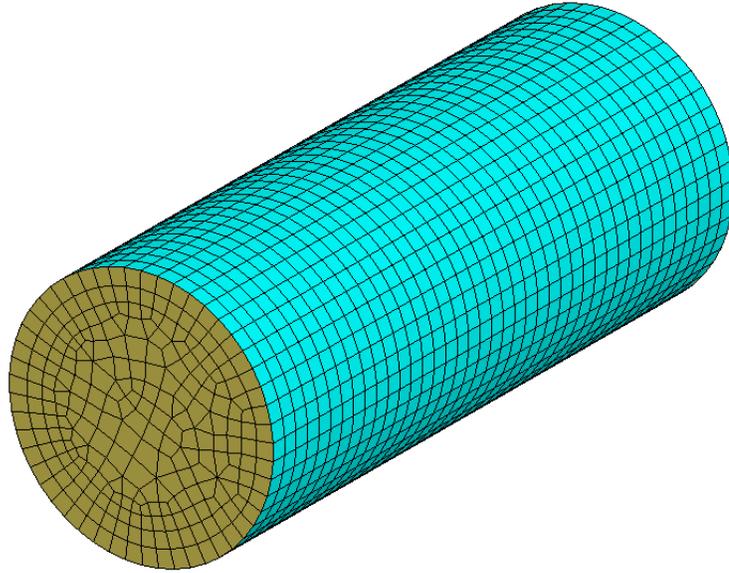
Figure 37: Inflated Cylinder Finite Element Model

A finite element analysis was completed in LS-DYNA using the MAT_FABRIC material model. The inflated cylinder model has a radius of 97.7 mm, a length of 497 mm, and thickness of 0.202 mm. The model is meshed with membrane elements; of which 2000 membrane elements were dedicated to the fabric portion of the model. Linear moduli from Table 9 were used for E_a, E_b, ν_{ab}, and G_{ab}. The end caps were modeled as steel with isotropic material properties.

The nodes at one end cap were constrained to have only a free rotational degree of freedom about the longitudinal axis. This end cap had a prescribed rotation $(40°)$ applied consistent with that in the experimental testing. The opposite end cap was constrained to have only a free axial degree of freedom. Inflation pressure is

applied using a simple airbag model to capture the effects of air compressibility on the structures stiffness. The inflation pressures were tested at 1 *psi* and 7 *psi*. The model was allow to inflate to the prescribed inflation pressure and then the prescribed rotation was applied. After the model reached a steady state, the resulting torque was measured at the nodes that were constrained from rotating about the longitudinal axis.
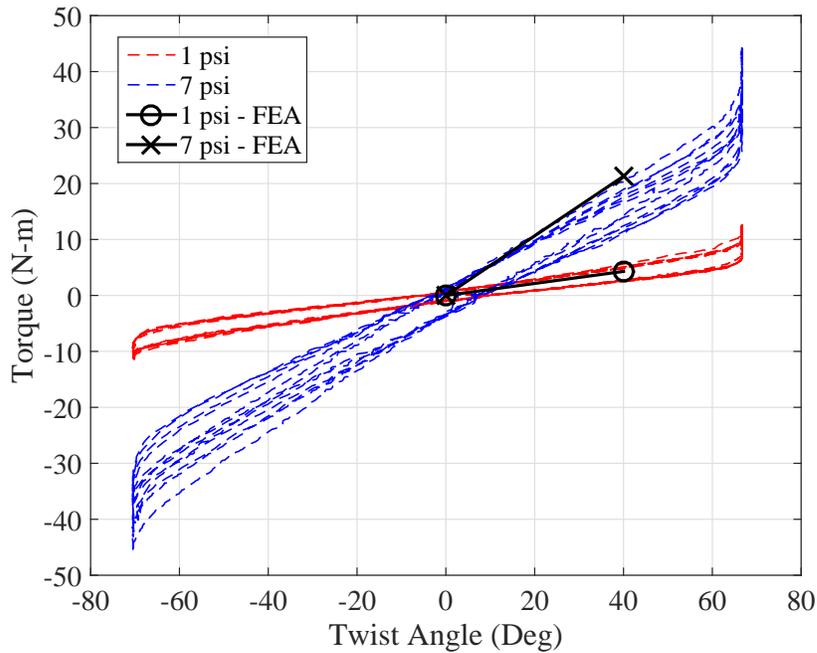
Figure 38: Applied Torque versus Twist Angle Comparison between Model and Data Cylinder of Urethane Coated Kevlar® at Three Inflation Pressures

Figure 38 provides a comparison between the experimental data and simulation results. The plot shows only a the final torque-rotation values from the simulation, with a line connecting them to the origin. This should not imply that the simulation results were linear. The torque-rotation values are compared because the important trends do not require the conversion to stress-strain.

The simulation results trend well with the experimental data. As the pressure increases the stiffness in the model increases. This is consistent with previous analysis and testing [43, 35, 27]. While the stiffness of the inflated cylinder increases with

increasing pressure, the same material shear modulus was used for all three models. This distinction is important because estimating shear modulus from the inflated cylinder test method and applying it to model of an air-inflated structure as shown above will likely result in an overly stiff structure.

2.6   Summary

In this chapter, the developed parameter identification methodology is applied to a set of bias-extension and uniaxial tension experimental test data. The parameter identification methodology is introduced. Mean Square Error is defined as the objective function to be minimized in the methodology. Multiple analyses are performed in preparation for the inverse analysis. These steps provide the prerequisite information required in a successful inverse analysis. In the nominal analysis, the nominal predictions are compared to the data through a direct analysis to identify where the model is fundamentally different than the experimental data. The nominal analysis describes the geometric and material models used in the finite element simulation as well as the specified loading and boundary conditions. A convergence study shows that the mesh size is set based on a balance between accuracy and computational expense. The strain distribution in the converged finite element model is shown to be consistent with theory.

Finally, an inverse analysis is performed to obtain an accurate match between the model predictions and the data through estimation of input parameters. The majority of the reduction in the objective function occurred during the first iteration. Poisson's ratio was shown to be an insignificant contribution to the objective function. This finding is consistent with the empirical knowledge of air-inflated structures. A high degree of correlation was shown between the three remaining parameters and the simulation of the test used to obtain them experimentally. The resulting estimate of shear modulus compares well with the experimental data from the trellis-frame test.

CHAPTER III

APPLICATION OF PARAMETER IDENTIFICATION TO
A MESOMECHANICAL MATERIAL MODEL

3.1   Introduction

Rohrschneider investigated structural analysis codes ABAQUS, ANSYS, and LS-DYNA for use on IAD models. In that work, LS-DYNA performed the best and produced consistent answers. [24]. Rohrschneider utilized several element formulations and material models with LS-DYNA in buckling simulations of an inflated column and torus as well.

The LS-DYNA fabric material model (MAT_FABRIC) discussed in Chapter 2 and originally developed for the airbag industry, was shown to provide solutions closest to the experimental data. The model is a variant of a nonlinear orthotropic material model and is valid for 3 or 4 node membrane elements. This model has been used extensively by the aerospace industry, but has required excessive and repetitive material testing for mechanical property inputs in order to recover realistic deformations.

A higher fidelity fabric material model (MAT_235) in LS-DYNA was developed for ballistic impact applications in 2001 [64]. This model considers a mesomechanical approach to provide the response of dry plain woven fabrics, but requires information not typically tested for in standard methods regarding behavior of the yarns themselves.

The present investigation will validate a mesomechanical model for structures pertaining to the analysis of IADs, as well as, provide guidance for obtaining required model inputs. The experimental data used to evaluate this higher fidelity material

model are taken from a series of previous tests to measure and characterize the normal and shear stress-strain behavior of textile fabrics relevant to IADs [25]. While a specific LS-DYNA material model is discussed in this chapter, observations and findings are generally relevant to the use of mesomechanical models regardless of the finite element solver employed.

3.2 Model Description

3.2.1 Representative Volume Cell

The development of this model follows the derivations of Ivanov and Tabiei [64]. This work, however, corroborates and elaborates on the model in much greater detail than is found in any one literature source. This is achieved through reconstructing the model outside of LS-DYNA in an effort to understand implementation specifics. In addition, multiple sources are combined to provided more detailed model development than is provided in Reference alone [64].

The foundation of the model is the Representative Volume Cell (RVC) as shown in Figure 39. The RVC, at the meso level, is constructed to represent the periodic structure of the fabric. While most other meso scale models use a cell with sides parallel to fiber directions, this model aligns its diagonals with the fiber directions [36]. It is most often assumed that the warp and weft yarns are initially orthogonal; however, as a result of deformations, they will not remain as such.

The RVC is shown in more detail in Figure 40 where the RVC is divided into four subcells. Two of the cells contain the weft (fill) yarn and the other two contain the warp yarn. The two subcells containing the same yarn are antisymmetric. The figure also shows the angles utilized for determining the direction of each yarn. The braid angle, θ, and the undulation angle, β. β_f and β_w are defined for the weft and warp yarns, respectively. The subcells are label (f, w, F, W), as shown in Figure 40. This will be utilized in the homogenization procedure in an effort to make the mathematical
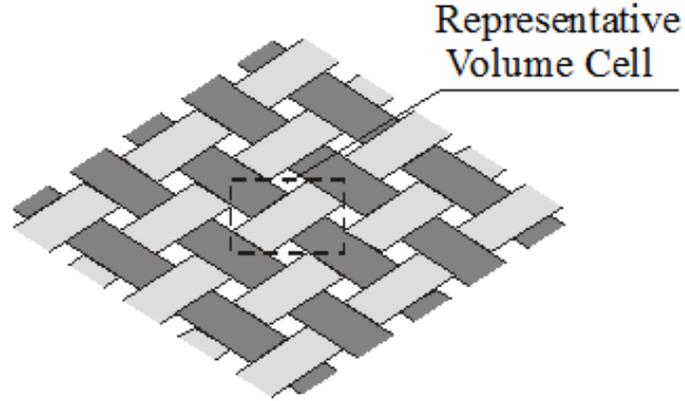
Figure 39: Flexible Woven Interlacing Pattern [64]

operations clear, as well as take advantage of the antisymmetry.
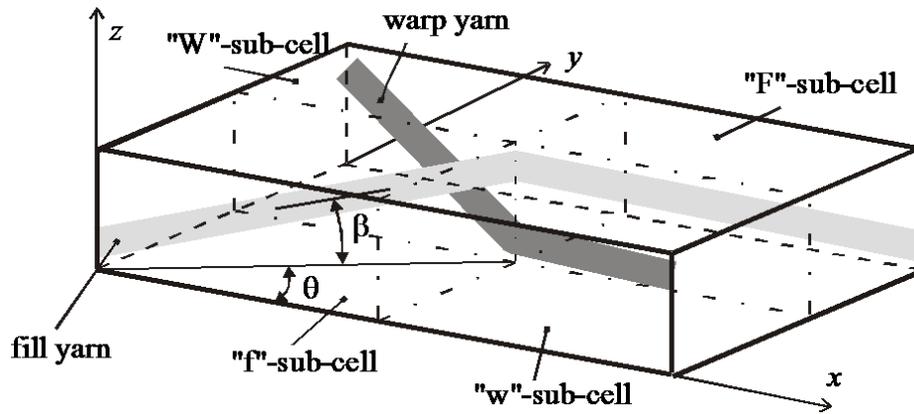
Figure 40: Tabiei and Ivanov Representative Volume Cell [64]

Prior to the homogenization process, the necessary coordinate systems must be defined. Three different coordinate systems will be utilized: the yarn material coordinate system, the RVC coordinate system, and the fabric coordinate system. The material properties of the yarns are expressed in the material coordinate system. The yarns are assumed to be transversely isotropic: meaning a special class of orthotropic material in which it has the same material properties in one plane and different properties in the direction normal to this plane.

The Voigt notation is used to express Hooke's Law. This notation will be consistently used throughout the development of material model. Equation (29) presents

the yarn material stiffness matrix, [C], expressed in the material coordinate system is noted with a ($''$). The material coordinate axes are labeled with lower case (x,y,z). The coordinate system transformations can be confusing without proper notation.

$$
\left[\sigma''\right] = \begin{bmatrix} \sigma_{xx} \\ \sigma_{yy} \\ \sigma_{zz} \\ \sigma_{xy} \\ \sigma_{yz} \\ \sigma_{xz} \end{bmatrix} = \begin{bmatrix} C''_{11} & C''_{12} & C''_{13} & 0 & 0 & 0 \\ C''_{21} & C''_{22} & C''_{23} & 0 & 0 & 0 \\ C''_{31} & C''_{32} & C''_{33} & 0 & 0 & 0 \\ 0 & 0 & 0 & C''_{44} & 0 & 0 \\ 0 & 0 & 0 & 0 & C''_{55} & 0 \\ 0 & 0 & 0 & 0 & 0 & C''_{66} \end{bmatrix} \begin{bmatrix} \epsilon_{xx} \\ \epsilon_{yy} \\ \epsilon_{zz} \\ 2\epsilon_{xy} \\ 2\epsilon_{yz} \\ 2\epsilon_{xz} \end{bmatrix} = \left[C''\right] \begin{bmatrix} \epsilon_{xx} \\ \epsilon_{yy} \\ \epsilon_{zz} \\ \gamma_{xy} \\ \gamma_{yz} \\ \gamma_{xz} \end{bmatrix} \quad (29)
$$

where (σ) defines the Cauchy stress and (ϵ) defines the Cauchy strain. As shown in Equation (30), The yarn stiffness matrix is expressed in the material coordinate system and contains 6 elastic constants. E_1, E_2, G_{12}, G_{23}, ν_{12}, and ν_{23} are the Elastic moduli, Shear moduli, and Poissons ratios of the yarn, respectively. The coefficient in front of the shear moduli, μ, is called the discount factor. It is defined as a function of the braid angle and can take on a value such that $0 < \mu \leq 1$. The fabric is not a continuous medium and the yarns will rotate over one another until they lock or jam together as a result of being loaded. The discount factor is used to model the low shear resistance in the fabric prior to the locking of the yarns. The initial value of the discount factor is typically set very close to zero because, due to friction between the yarns, the fabric has some shear resistance. μ is not allowed to be exactly zero as it would cause the stiffness matrix to become singular. When locking has occurred, the fabric begins to behave as an elastic medium, the discount factor is set to 1, and the yarns full shear modulus is regained.

$$\left[C'' \right] = \begin{bmatrix} \frac{1}{E_1} & \frac{-\nu_{12}}{E_1} & \frac{-\nu_{12}}{E_1} & 0 & 0 & 0 \\ \frac{-\nu_{12}}{E_1} & \frac{1}{E_2} & \frac{-\nu_{23}}{E_2} & 0 & 0 & 0 \\ \frac{-\nu_{12}}{E_1} & \frac{-\nu_{23}}{E_2} & \frac{1}{E_2} & 0 & 0 & 0 \\ 0 & 0 & 0 & \frac{1}{\mu G_{12}} & 0 & 0 \\ 0 & 0 & 0 & 0 & \frac{1}{\mu G_{23}} & 0 \\ 0 & 0 & 0 & 0 & 0 & \frac{1}{\mu G_{12}} \end{bmatrix}^{-1} \tag{30}$$

Different stiffness matrices are used for the weft and warp yarns to allow for modeling an unbalanced fabric. As part of the homogenization procedure, the yarn material properties expressed in the material coordinate system must be rotated to the RVC coordinate system. The transformation of each subcell is performed using Equation (31). The yarn material stiffness matrix expressed in the RVC coordinate system is noted with a ('). [T] is the strain transformation matrix.

$$[C'] = [T(\beta, \theta)]^T [C''] [T(\beta, \theta)] \tag{31}$$

This transformation matrix is a function of the directional cosines of the material axes unit vectors with respect to the RVC coordinate system. For purposes of expressing the constitutive matrix of the yarn material in the RVC coordinate system, the directional cosine convention shown in Equation (32) is followed in the rotation matrix. It should be noted that the components including $sin(\beta)$ have a sign change to treat these rotations as positive rather than negative.

$$\begin{bmatrix} xx \\ yy \\ zz \end{bmatrix} = \begin{bmatrix} \cos(\beta)\cos(\theta) & \cos(\beta)\sin(\theta) & \sin(\beta) \\ -\sin(\theta) & \cos(\theta) & 0 \\ -\sin(\beta)\cos(\theta) & -\sin(\beta)\sin(\theta) & \cos(\beta) \end{bmatrix} \begin{bmatrix} XX \\ YY \\ ZZ \end{bmatrix} = \begin{bmatrix} l_1 & m_1 & n_1 \\ l_2 & m_2 & n_2 \\ l_3 & m_3 & n_3 \end{bmatrix} \begin{bmatrix} XX \\ YY \\ ZZ \end{bmatrix} \tag{32}$$

The strain transformation matrix referenced in Equation (31) is defined as shown in Equation (33).

$$
\begin{bmatrix} T \end{bmatrix} = \begin{bmatrix}
l_1^2 & m_1^2 & n_1^2 & l_1 m_1 & m_1 n_1 & n_1 l_1 \\
l_2^2 & m_2^2 & n_2^2 & l_2 m_2 & m_2 n_2 & n_2 l_2 \\
l_3^2 & m_3^2 & n_3^2 & l_3 m_3 & m_3 n_3 & n_3 l_3 \\
2l_1 l_2 & 2m_1 m_2 & 2n_1 n_2 & (l_1 m_2 + l_2 m_1) & (m_1 n_2 + m_2 n_1) & (n_1 l_2 + l_2 n_1) \\
2l_2 l_3 & 2m_2 m_3 & 2n_2 n_3 & (l_2 m_3 + l_3 m_2) & (m_2 n_3 + m_3 n_2) & (n_2 l_3 + l_3 n_2) \\
2l_3 l_1 & 2m_3 m_1 & 2n_3 n_1 & (l_3 m_1 + l_1 m_3) & (m_3 n_1 + m_1 n_3) & (n_3 l_1 + l_1 n_3)
\end{bmatrix}
\tag{33}
$$

As a result of expressing the yarn material properties in the RVC coordinate system, the constitutive matrix has the form shown in Equation (34). All of the matrix components are now possibly non-zero. The RVC coordinate axes are labeled with upper case (X,Y,Z).

$$
\begin{bmatrix} \sigma' \end{bmatrix} = \begin{bmatrix}
\sigma_{XX} \\ \sigma_{YY} \\ \sigma_{ZZ} \\ \sigma_{XY} \\ \sigma_{YZ} \\ \sigma_{XZ}
\end{bmatrix} = \begin{bmatrix}
C_{11} & C_{12} & C_{13} & C_{14} & C_{15} & C_{16} \\
C_{21} & C_{22} & C_{23} & C_{24} & C_{25} & C_{26} \\
C_{31} & C_{32} & C_{33} & C_{34} & C_{35} & C_{36} \\
C_{41} & C_{42} & C_{43} & C_{44} & C_{45} & C_{46} \\
C_{51} & C_{52} & C_{53} & C_{54} & C_{55} & C_{56} \\
C_{61} & C_{62} & C_{63} & C_{64} & C_{65} & C_{66}
\end{bmatrix} \begin{bmatrix}
\epsilon_{XX} \\ \epsilon_{YY} \\ \epsilon_{ZZ} \\ \gamma_{XY} \\ \gamma_{YZ} \\ \gamma_{XZ}
\end{bmatrix} = \begin{bmatrix} C' \end{bmatrix} \begin{bmatrix} \epsilon' \end{bmatrix}
\tag{34}
$$

Each of the subcell stiffness matrices must be computed during the homogenization process. Each of the subcells is generally symmetric about the main diagonal. In addition, there is antisymmetry between the weft subcells and the warp subcells. This makes the transformation easier since only two transformations are necessary to calculate all four matrices. Equation (35) is used to calculate the F subcell stiffness matrix using that of the f subcell. The same relation exists between the W and w subcells.

$$\left[C^F \right] = \begin{bmatrix} C_{11}^f & C_{12}^f & C_{13}^f & C_{14}^f & -C_{15}^f & -C_{16}^f \\ C_{21}^f & C_{22}^f & C_{23}^f & C_{24}^f & -C_{25}^f & -C_{26}^f \\ C_{31}^f & C_{32}^f & C_{33}^f & C_{34}^f & -C_{35}^f & -C_{36}^f \\ C_{41}^f & C_{42}^f & C_{43}^f & C_{44}^f & -C_{45}^f & -C_{46}^f \\ -C_{51}^f & -C_{52}^f & -C_{53}^f & -C_{54}^f & C_{55}^f & C_{56}^f \\ -C_{61}^f & -C_{62}^f & -C_{63}^f & -C_{64}^f & C_{65}^f & C_{66}^f \end{bmatrix} \tag{35}$$

The four subcell stiffness matrices are combined in order to arrive at a single stiffness matrix for the RVC. The transformed subcell stiffness matrices are homogenized in order to obtain the effective material properties of the RVC.

3.2.2 Homogenization Method

The homogenization procedure was originally formulated in Reference [81]. Iso-stress and strain conditions are assumed across the subcell boundaries. The stress and strain components are divided into the iso-strain or in-plane components and the iso-stress or out-of-plane components. The subcell 6 component stress and strain vectors are expressed using the organizational convention in Equation (36). These components are reorganized to group the in-plane and out-of-plane components together. The three in-plane stress components expressed in the RVC coordinate system are organized as follows, as a function of both the in plane and out of plane strain components.

$$\left[\sigma_N \right]_k = \begin{bmatrix} \sigma_{XX} \\ \sigma_{YY} \\ \sigma_{XY} \end{bmatrix}_k = \begin{bmatrix} C_{11} & C_{12} & C_{14} \\ C_{21} & C_{22} & C_{24} \\ C_{41} & C_{42} & C_{44} \end{bmatrix}_k \begin{bmatrix} \epsilon_{XX} \\ \epsilon_{YY} \\ \gamma_{XY} \end{bmatrix}_k + \begin{bmatrix} C_{13} & C_{15} & C_{16} \\ C_{23} & C_{25} & C_{26} \\ C_{43} & C_{45} & C_{46} \end{bmatrix}_k \begin{bmatrix} \epsilon_{ZZ} \\ \gamma_{YZ} \\ \gamma_{XZ} \end{bmatrix}_k \tag{36}$$

The subscript (N) denotes the iso-strain or in plane components. These are the stress and strain components associated with plane stress conditions. The (k) subscript is used to denote the subcells (f, w, F, W). A contracted notation shown in Equation (37) is used for the remainder of the discussion.

$$\left[\sigma_N\right]_k = \left[C_{NN}\right]_k \left[\epsilon_N\right]_k + \left[C_{NS}\right]_k \left[\epsilon_S\right]_k \tag{37}$$

The subscript (S) denotes the iso-stress or out of plane components. The three out of plane stress components expressed in the RVC coordinate system are organized as in Equation (38), as a function of both the in-plane and out of plane strain components.

$$\left[\sigma_S\right]_k = \begin{bmatrix} \sigma_{ZZ} \\ \sigma_{YZ} \\ \sigma_{XZ} \end{bmatrix}_k = \begin{bmatrix} C_{31} & C_{32} & C_{34} \\ C_{51} & C_{52} & C_{54} \\ C_{61} & C_{62} & C_{64} \end{bmatrix}_k \begin{bmatrix} \epsilon_{XX} \\ \epsilon_{YY} \\ \gamma_{XY} \end{bmatrix}_k + \begin{bmatrix} C_{33} & C_{35} & C_{36} \\ C_{53} & C_{55} & C_{56} \\ C_{63} & C_{65} & C_{66} \end{bmatrix}_k \begin{bmatrix} \epsilon_{ZZ} \\ \gamma_{YZ} \\ \gamma_{XZ} \end{bmatrix}_k \tag{38}$$

Similar to the iso-strain components, the contracted notation for the iso-stress components is shown in Equation (39).

$$\left[\sigma_S\right]_k = \left[C_{SN}\right]_k \left[\epsilon_N\right]_k + \left[C_{SS}\right]_k \left[\epsilon_S\right]_k \tag{39}$$

The result of the homogenization procedure is the effective stiffness matrix shown in Equations (41) and (42). The effective stress components are constructed using volumetric averages of the subcells known as *The Rule of Mixtures*. This is permitted by assuming that at all points, within the homogenized volume, the stress and strain are the same.

$$\begin{bmatrix} \bar{\sigma}_N \\ \bar{\sigma}_S \end{bmatrix} = \left[\bar{\sigma}\right] = \left[\bar{C}'\right] \left[\bar{\epsilon}\right] = \begin{bmatrix} \bar{C}_{NN} & \bar{C}_{NS} \\ \bar{C}_{SN} & \bar{C}_{SS} \end{bmatrix} \begin{bmatrix} \bar{\epsilon}_N \\ \bar{\epsilon}_S \end{bmatrix} \tag{40}$$

Applying the mixed boundary conditions to the subcells, the iso-strain assumption implies that the effective in-plane strains must be the same across the subcells. In addition, the out-of-plane stresses are also assumed to be the same. The rule of mixtures is applied to the out of plane strains and in plane stresses, as well. Equations (41) to (44) expresses the above assumptions mathematically.

$$
\left[\bar{\epsilon}_N\right] = \left[\epsilon_N\right]_k \tag{41}
$$

$$
\left[\bar{\sigma}_S\right] = \left[\sigma_S\right]_k \tag{42}
$$

$$
\left[\bar{\epsilon}_S\right] = \sum_k f_k \left[\epsilon_S\right]_k \tag{43}
$$

$$
\left[\bar{\sigma}_N\right] = \sum_k f_k \left[\sigma_N\right]_k \tag{44}
$$

The boundary conditions are associated with the shell or membrane element formulation. The volume fraction, f_k, of the kth subcell in the RVC can be varied to account for an unbalanced fabric. Using a value of $(f_k = \frac{1}{4})$ implies that the warp and weft yarns constitute equal portions of the RVC.

Substituting Equations (41) and (42) into both Equations (37) and (39) results in subcell out of plane strains and in plane stresses expressed as a function of effective out of plane stresses and in plane strains. These resulting quantities are then substituted into Equations (43) and (44); which are rearranged to arrive at Equations (45) and (46), where the effective stresses are a function of the effective strains.

$$
\left[\bar{\sigma}_N\right] = \left(\left[C_1^*\right] + \left[C_2^*\right]\left[C_3^*\right]^{-1}\right)\left[\bar{\epsilon}_N\right] + \left(\left[C_2^*\right]\left[C_3^*\right]^{-1}\right)\left[\bar{\epsilon}_S\right] \tag{45}
$$

$$
\left[\bar{\sigma}_S\right] = \left(\left[C_3^*\right]^{-1}\left[C_4^*\right]\right)\left[\bar{\epsilon}_N\right] + \left(\left[C_3^*\right]^{-1}\right)\left[\bar{\epsilon}_S\right] \tag{46}
$$

where intermediate matrices are defined in Equations (47) to (50) in order to condense the above equations.

$$
\left[C_1^*\right] = \sum_k f_k \left(\left[C_{NN}\right]_k - \left[C_{NS}\right]_k \left[C_{SS}\right]_k^{-1} \left[C_{SN}\right]_k\right) \tag{47}
$$

91

$$\left[C_2^*\right] = \sum_k f_k \left[C_{NS}\right]_k \left[C_{SS}\right]_k^{-1} \tag{48}$$

$$\left[C_3^*\right] = \sum_k f_k \left[C_{SS}\right]_k^{-1} \tag{49}$$

$$\left[C_4^*\right] = \sum_k f_k \left[C_{SS}\right]_k^{-1} \left[C_{SN}\right]_k \tag{50}$$

The resulting effective stiffness matrix represents the properties of the fabric material expressed in the RVC coordinate system. The components of this matrix will be symmetric about the main diagonal due to the nature of the subcells. It is noted that the effective stiffness shown in Equation (51) is reordered back to the original convention established prior to the homogenization process.

$$\left[\bar{\sigma}\right] = \begin{bmatrix} \bar{\sigma}_{XX} \\ \bar{\sigma}_{YY} \\ \bar{\sigma}_{ZZ} \\ \bar{\sigma}_{XY} \\ \bar{\sigma}_{YZ} \\ \bar{\sigma}_{XZ} \end{bmatrix} = \begin{bmatrix} \bar{C}_{11} & \bar{C}_{12} & \bar{C}_{13} & \bar{C}_{14} & 0 & 0 \\ \bar{C}_{21} & \bar{C}_{22} & \bar{C}_{23} & \bar{C}_{24} & 0 & 0 \\ \bar{C}_{31} & \bar{C}_{32} & \bar{C}_{33} & \bar{C}_{34} & 0 & 0 \\ \bar{C}_{41} & \bar{C}_{42} & \bar{C}_{43} & \bar{C}_{44} & 0 & 0 \\ 0 & 0 & 0 & 0 & \bar{C}_{55} & \bar{C}_{56} \\ 0 & 0 & 0 & 0 & \bar{C}_{65} & \bar{C}_{66} \end{bmatrix} \begin{bmatrix} \bar{\epsilon}_{XX} \\ \bar{\epsilon}_{YY} \\ \bar{\epsilon}_{ZZ} \\ \bar{\gamma}_{XY} \\ \bar{\gamma}_{YZ} \\ \bar{\gamma}_{XZ} \end{bmatrix} \tag{51}$$

Since the model is implemented into a membrane element formulation, the $\bar{C}_{55}$, $\bar{C}_{56}$, and $\bar{C}_{66}$ components can be eliminated from the effective stiffness matrix. This elimination is allowed because the corresponding stress and strain components are always zero for membrane elements. This comes with the added benefit of making the code more computationally efficient. At every time step in an explicit finite element simulation, the instantaneous stiffness matrix is used to obtain the stress response of the fabric resulting from an increment of strain.

3.2.3 Yarn Reorientation

The reorientation of the fabric yarns is accounted for in this model. At a given time step, the current state of the global finite element model is a function of the yarns orientation in the RVC. Geometric nonlinearity is introduced to the model through the yarn reorientation and possible locking. As shown in Figure 41, unit direction vectors q_f and q_w are defined in the RVC coordinate system for the weft (fill) and warp yarns, respectively.
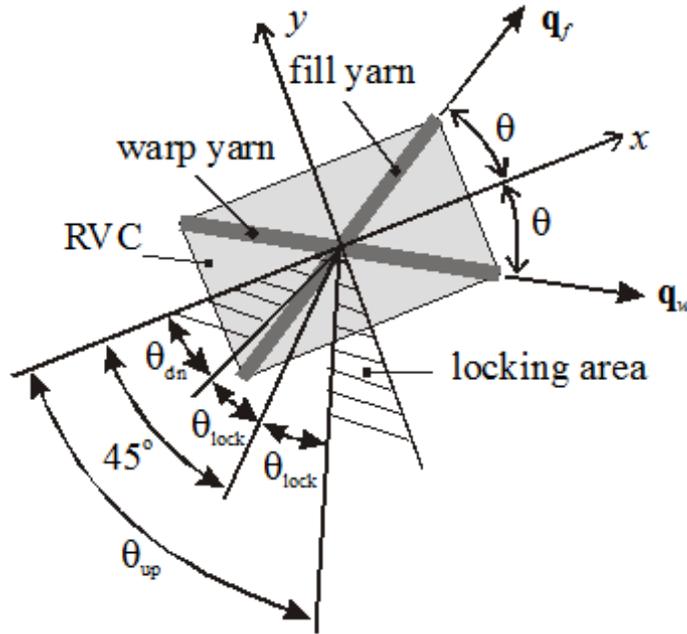
Figure 41: Range of Locking Angles [64]

The unit direction vectors ,$(\vec{q})$, for the warp and weft yarns are defined for the yarn material in the w and f subcells. Initially, the unit direction vectors are defined as shown in Equation (52):

$$\vec{q_i} = \left\{ \cos(\beta_i)\cos(\theta) \quad \cos(\beta_i)\sin(\theta) \quad \sin(\beta_i) \right\}^T \ for \ i = f, w \tag{52}$$

The deformation gradient matrix, $[F]$, is used to update the unit direction vectors at each time step. Due to the small increments in strain, an infinitesimal strain assumption is employed to construct the deformation gradient. To understand how

the yarn unit direction vectors are rotated as the element is deformed, the derivation of the deformation gradient in the model is stepped through in more detail. First, it is beneficial to provide a physical understanding to the deformation gradient prior to defining it mathematically. The deformation gradient is a tensor that quantifies the shape change and material rotation. This property makes it better than strain as a more comprehensive measure of deformation in material elements. Consider the simple example provided in Figure 42. Let the shape on the left represent an undeformed material element, while the shape on the right represents the deformed element. By introducing horizontal and vertical axes, the undeformed element can be said to have unit length in both axes. It can be seen that the deformed element is stretched in both principal directions.
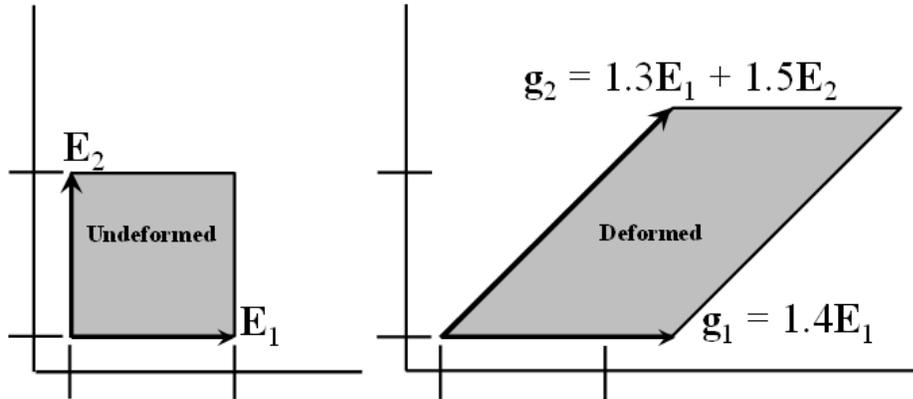
Figure 42: Determination of Deformation Gradient Graphically

The resulting direction vectors are expressed in terms of the initial unit direction vectors. Reading from the plot on the right, the components of the direction vectors can expressed in vector form as in Equation (53).

$$\vec{g_1} = \begin{bmatrix} 1.4 & 0 \end{bmatrix}^T \ and \ \vec{g_2} = \begin{bmatrix} 1.3 & 1.5 \end{bmatrix}^T \tag{53}$$

Assembling these components into a 2×2 matrix as shown in Equation (54) results in a 2D deformation gradient tensor for this element.

$$\mathbf{F} = \begin{bmatrix} 1.4 & 1.3 \\ 0 & 1.5 \end{bmatrix} \tag{54}$$

Working from the derivation in Crisfield, consider an element $\mathbf{dX}$ that has original coordinates (X) [82]. Let the element be moved to new coordinates (x) resulting from displacement (u) as shown in Figure 43.
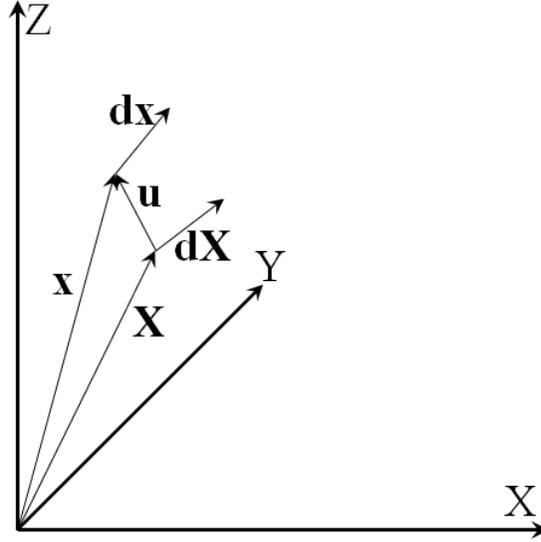
Figure 43: Element Position Vectors

This can be written in vector form and differentiated to give the later part of Equation (55).

$$\vec{x} = \vec{X} + \vec{u} \;\Rightarrow\; \vec{dx} = \frac{\partial \vec{x}}{\partial \vec{X}} d\vec{X} = \mathbf{F} d\vec{X} = \frac{\partial(\vec{X} + \vec{u})}{\partial \vec{X}} d\vec{X} \tag{55}$$

Expanding upon this, Equation (56) introduces the mathematical representation of the deformation gradient (F) which can be expressed as the identity matrix plus the displacement derivative matrix. In the case of infinitesimal strains, the deformation gradient can be expressed in the final form of Equation (56). This form works well with the explicit finite element method because of the inherently small time steps used in this method.

$$
\mathbf{F} = \begin{bmatrix} \frac{\partial x}{\partial X} & \frac{\partial x}{\partial Y} & \frac{\partial x}{\partial Z} \\[8pt] \frac{\partial y}{\partial X} & \frac{\partial y}{\partial Y} & \frac{\partial y}{\partial Z} \\[8pt] \frac{\partial z}{\partial X} & \frac{\partial z}{\partial Y} & \frac{\partial z}{\partial Z} \end{bmatrix} = \begin{bmatrix} 1 + \frac{\partial u}{\partial X} & \frac{\partial u}{\partial Y} & \frac{\partial u}{\partial Z} \\[8pt] \frac{\partial v}{\partial X} & 1 + \frac{\partial v}{\partial Y} & \frac{\partial v}{\partial Z} \\[8pt] \frac{\partial w}{\partial X} & \frac{\partial w}{\partial Y} & 1 + \frac{\partial w}{\partial Z} \end{bmatrix} = \begin{bmatrix} 1 + \Delta\epsilon_1 & \frac{\Delta\epsilon_4}{2} & 0 \\[8pt] \frac{\Delta\epsilon_4}{2} & 1 + \Delta\epsilon_2 & 0 \\[8pt] 0 & 0 & 1 + \Delta\epsilon_3 \end{bmatrix}
$$
$$(56)$$

As stated earlier, the directions of both the warp and weft yarns are determined by the unit direction vectors, q_w and q_f, respectfully. At the beginning of the simulation, the unit direction vectors are defined based on Equation (52). After computing the deformation gradient matrix, using the strains at each time step, the updated direction vectors of each yarn are computed and normalized, as in Equation (57), to remain unit vectors.

$$
\vec{q'}_i = \mathbf{F}\vec{q}_i \ \Rightarrow \ \vec{q}_i = \frac{\vec{q'}_i}{\|\vec{q'}\|} \ for \ i = f, w
$$
$$(57)$$

New values defining the orientation of the yarns are then calculated, as is shown in Equations (58) and (59), from the components of the unit direction vectors.

$$
\beta_i = sin^{-1}(q_{i3}) \ for \ i = f, w
$$
$$(58)$$

$$
\theta = \frac{tan^{-1}(q_{f2}/q_{f1}) - tan^{-1}(q_{w2}/q_{w1})}{2}
$$
$$(59)$$

For an explicit finite element code, such as LS-DYNA, the time integration stability conditions require small time steps. This works well with the infinitesimal strain assumption. In the case of plane stress for membrane elements in the explicit finite element method, the transverse normal strain increment component, $\Delta\bar{\epsilon}_3$, has to be calculated first. This transverse strain is important in calculating the change in thickness for the membrane elements. The transverse normal strain is obtained from the, $\Delta\bar{c}_3 = 0$, condition in Equation (60).

$$\Delta \bar{\epsilon}_3 = -\frac{\bar{C}_{13} \Delta \bar{\epsilon}_1 + \bar{C}_{23} \Delta \bar{\epsilon}_2 + \bar{C}_{34} \Delta \bar{\epsilon}_4}{\bar{C}_{33}} \qquad (60)$$

3.2.4 Parameter Discussion

Values for the initial braid angle are usually set in a free state at an angle equal to 45°. In the case that this model is used to simulate the behavior of a biaxial braided fabric, the initial braid angle could be set to values other than 45° to study the effect of varying braid angle on an air-inflated structure. In addition, this parameter could be used to study the effect of a small misalignments in the yarns on a structure.

Mathematically, the undulation angle changes with the yarn and varies from $0° < \beta \leq 90°$. In practice, it is typical for undulation angles much smaller than that. As discussed in previous chapters, the maximum value of the undulation angle is a function of crimping. In this model, the undulation angle is an average value characterizing the material principle directions of a sub-cell. As shown in Equation (61), the inverse tangent of half the fabric thickness divided by the distance between yarns is considered a good approximation for the undulation angle needed for the model.

$$\beta = \tan^{-1}\left(\frac{h}{2s}\right) \qquad (61)$$

The discount factor, μ, scales the shear moduli of the yarn before locking occurs. The factor is a function of the braid angle and can be altered to switch the fabric model from a trellis mechanism to an elastic medium. A piece-wise function with a linear transition range is chosen for the discount factor [64]. Parameters μ_0, $\Delta\theta$, and θ_{lock} govern the initial behavior, transition range, and locked behavior respectively. $\Delta\theta$ can be set a small as possible while being large enough to prevent high frequency oscillations that can occur from sharp changes in model behavior.

The minimum value of the discount factor, μ_0, corresponds to the period in the load history when the yarns are still open. The value should provide small shear

resistance and negligible tension in the yarns when loading is applied in the bias direction. In the case of a coated plain woven fabric, the initial discount factor should be set to model the initial shear behavior dominated by the coating.

As shown in Figure 44, the range of the locking angle, θ_{lock}, can be obtained from the yarn width, w, and the spacing parameter of the fabric, s, using the simple geometrical approximation in Equation (62). In the absence of actual yarn measurements, a good approximation for the spacing parameter of the fabric is the reciprocal of the thread count in a given direction.

$$\sin 2\theta_{min} = \frac{w}{s} \tag{62}$$
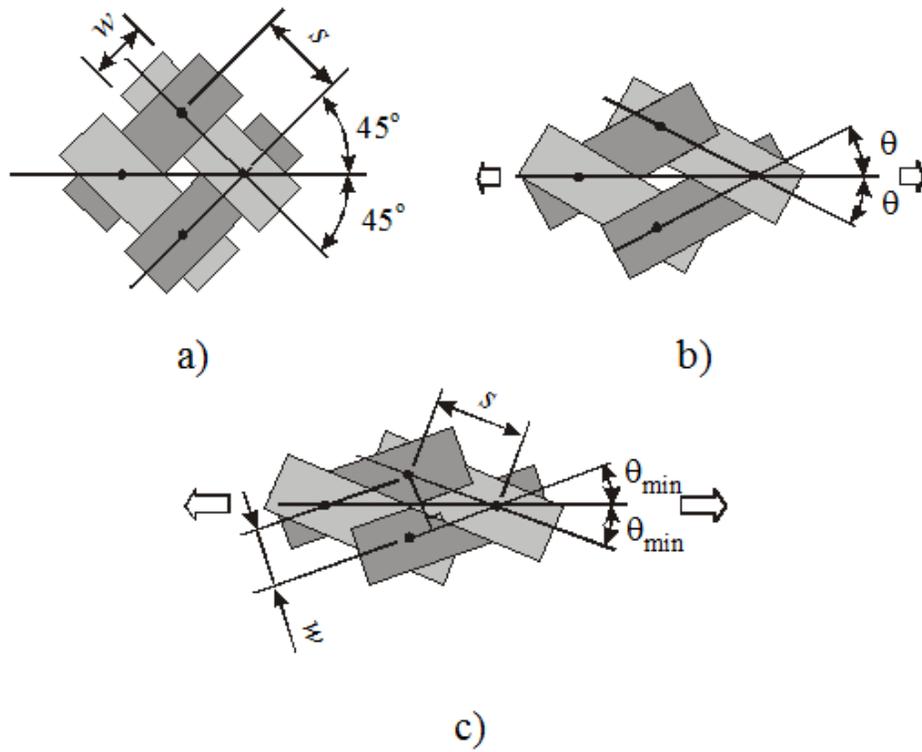
Figure 44: In-plane Motion of Woven Fabrics as Trellis Mechanism (a) Initial State (b) Slightly Stretched in Bias Direction (c) Stretched to Locking [64]

Table 12 provides descriptions for all model parameters.

Using initial parameter estimates and ranges, these parameters can be chosen to fit the force-displacement curve recorded during tests such as the Bias-Extension,

Table 12: MAT_235 Input Parameters and Descriptions

Variable	Symbol	Description
RO	ρ	Yarn Mass Density
E1	E_1	Young's Modulus of Yarn - Axial Direction
E2	E_2	Young's Modulus of Yarn - Transverse Direction
G12	G_{12}	Shear Modulus of Yarn
G23	G_{23}	Transverse Shear Modulus of Yarn
V12	ν_{12}	Poisson's Ratio
V23	ν_{23}	Transverse Poisson's Ratio
XT	X_t	Stress or Strain to Failure
THI	θ_i	Initial Braid Angle
THL	θ_l	Yarn Locking Angle
BFI	β_{fi}	Initial Undulation Angle - Weft Direction
BWI	β_{wi}	Initial Undulation Angle - Warp Direction
DSCF	μ	Discount Factor
CNST	D_R	Reorientation Damping Constant
ATLR	$\Delta\theta$	Angle Tolerance for Locking

Uniaxial Tension, or Trellis Frame tests of the fabric. Parameters are chosen to simulate and best fit the force-displacement curve to the experimentally obtained curve. Before proceeding to the inverse analysis, the experimental data is examined and corrected if necessary. Nominal analyses are carried out using the initial parameter estimates. These nominal analyses are used to examine the model fidelity by identifying where the data trends are fundamentally different from model predictions. Finally, parameter ranges that are used in the inverse analyses are selected.

3.3   Nominal Analysis

The experimental data used to carry out the inverse analysis is that of the 200 denier Plain Woven Silicone coated Kevlar® introduced in the previous chapter. The loading condition is that of the Bias Extension test which is well suited for this material model. Due to the orientation of the RVC, a rectangular mesh aligned with the edges of the fabric sample aligns the yarns in this manner. Thus, the Bias Extension test is perhaps a natural starting point for numerical simulation.

As described earlier in this work, a fabric's shear behavior consist of several phases, such as deformation when the shearing forces at yarn intersections is too small to

overcome friction, slippage of the yarns once that friction is overcome, and elastic deformation after yarn locking. While the shear modulus, G, is usually much less than the elastic modulus, E, in the warp and weft directions, it has a significant effect on the effective moduli on orientations not align with the warp and weft directions. The idealized shear stress-strain behavior of a coated woven fabric is presented back in Figure 12. A rubber sheet demonstrates a plastic response, while woven fabrics typically have a hyperelastic response. The response of a coated woven fabric is typically a composite of these patterns, with the rubberized sheet dominating at low strain, and the woven fabric at higher strain.

The Bias Extension test data available for this work is limited to lower strains. As such the attempts to model the elastic deformation after yarn locking that occurs at higher strains requires additional data from which to fit. One method to deal with the lack of data is to extrapolate from the existing data. This can be complicated when there is not actual data from which to continue the trend in the curve. In addition, the more nonlinear the data, the less confidence one has in accuracy. In this work, a combination of literature sources and complimentary data sets are utilized to lend confidence in the extrapolation method. Furthermore, this work is more interested in demonstrating the parameter identification methodology on applicable data sets than providing exact parameter estimates for the 200 denier Plain Woven Silicone coated Kevlar® fabric.

Figure 45 provides a comparison of the experimental bias extension test data with an extrapolated curve fit. A fourth order curve fit with an $R^2 > 0.999$ was applied to available data. The curve fit equation was then use to calculate a simulated force-displacement curve ranging from 0 to 40 mm. The resulting curve fit exhibits an initial approximately linear region, that fits well with the available data, followed by steeper response that corresponds to the elastic response after locking.

Taha et al. provide a comparison of Trellis Frame and Bias Extension tests for
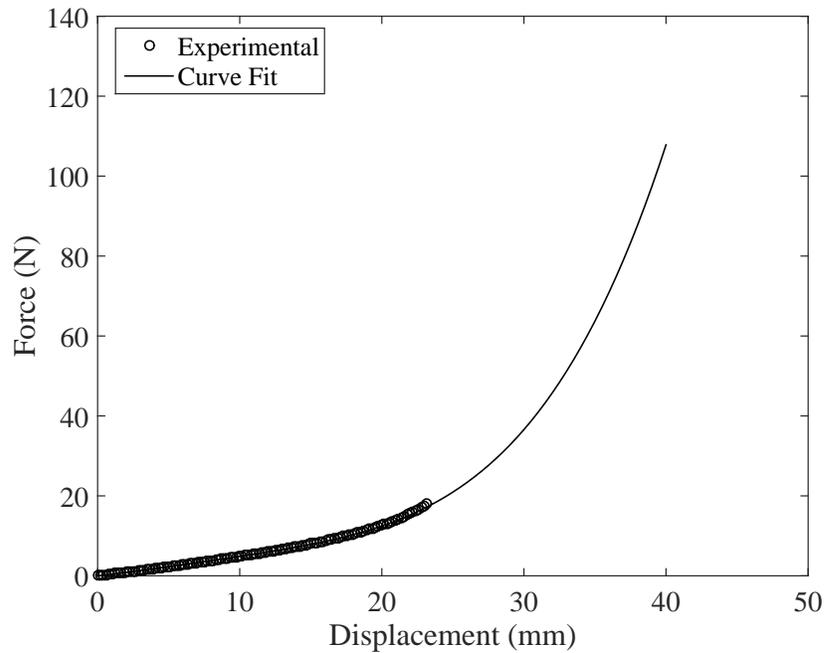
Figure 45: Comparison of Experimental Data with Extrapolated Curve Fit

the characterization of shear behavior in natural fibre woven fabrics [83]. In that study, force-displacement curves for both tests are compared and the data trends are consistent between the simulated Bias Extension data and available Trellis Frame data from Reference [25]. This lends confidence to extrapolation method selected for this work.

Table 13 outlines the initial input parameter values. The initial yarn material property estimates were obtained from a combination of sources including an online database for the Kevlar® 29 yarn [84]. Strain rate effects are not considered in this work. Thus, the two viscous modulus parameters were set to values near zero. Initial estimates for fabric architecture are made using approximates discussed in this chapter. D_R is related to CNST and refers to the reorientation damping coefficient.

The Bias Extension geometric model and boundary conditions are kept consistent with Chapter 2. This investigation utilizes the LS-DYNA MAT_235 material model

Table 13: MAT_235 Nominal Input Parameter Values

Symbol	Value	Units
ρ	1.44	g/cm^3
E_1	61	GPa
E_2	4.2	GPa
G_{12}	2.9	GPa
G_{23}	2.9	GPa
ν_{12}	0.35	-
ν_{23}	0.35	-
X_t	10	GPa
θ_i	45	Deg
θ_l	7.5	Deg
β_{fi}	5	Deg
β_{wi}	5	Deg
μ	2e-4	-
D_R	1000	-
$\Delta\theta$	0.5	Deg

which utilizes the micro-mechanical approach and the homogenization technique usually used in composite material models. The model accounts for reorientation of the yarns and the fabric architecture. The behavior of the flexible fabric material is achieved by discounting the shear moduli of the material in free state, which allows the simulation of the trellis mechanism before packing the yarns. As of the writing of this thesis MAT_235 is not supported by the implicit solver, so the LS-DYNA explicit solver is used for all simulations.

Figure 46 provides a comparison of the experimental Bias Extension test data with model predictions using nominal parameters. The nominal results exhibit the initial trellising behavior followed by stiffer locking behavior. Comparing the simulation results with the experimental data, a shallower initial response, sharper transition, and steeper response after the transition are observed.

The homogenization procedure and yarn reorientation are carried out at each time step. While the yarn reorientation procedure utilizes the deformation gradient to update the yarn unit vectors, the homogenization procedure only considers the architecture's current state. This means that the homogenized material properties can be studied regardless of any deformation information. It is beneficial to study the
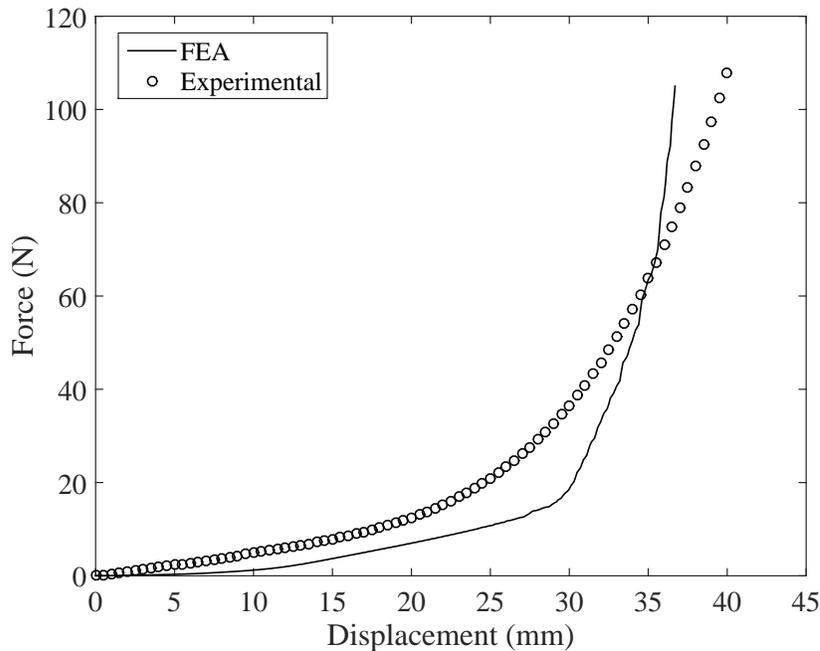
Figure 46: Comparison of Data with Predictions from Model Based on Nominal Parameters

homogenized results to gain insights into material property sensitivity to changes in input parameters. Figures 47, 48, 49, and 50 show the homogenized in plane material properties as a function of the undulation angle. The RVC orientation corresponds to loading in the bias direction. The material properties are the elastic moduli, Poisson's Ratio, and shear modulus in the local material coordinate system.

As expected, Figures 47 and 48 have identical trends since the warp and weft yarns are oriented $[-45°,+45°]$ from the loading axis. The plots show data for free and locked states. A value of $\mu = 1e - 5$ provides a great enough discount on the yarn shear moduli to show the difference between the two states. The plots show little influence from changes in undulation angle between 0 and 9°. This is a realistic range of angles based on estimates calculated using information from Table 1 and Equation (61). The yarn material properties used for this homogenization study were consistent with those in Reference [64]. The elastic moduli are near 0.1 MPa in the free state and approximately 8.9 GPa in the locked state. This behavior can be
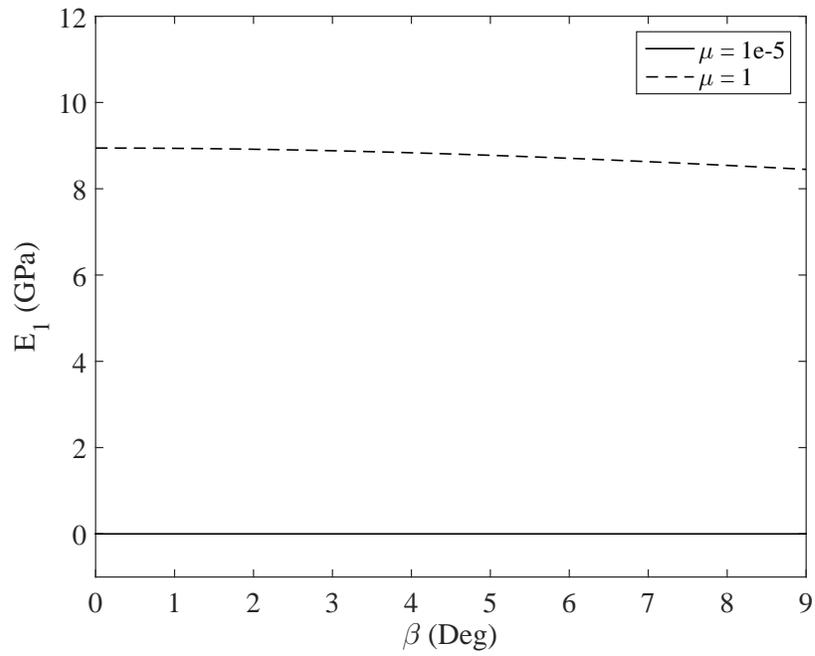
Figure 47: Comparison of Undulation Angle Influence on Homogenized Longitudinal Elastic Modulus in Free and Locked States

mapped to the large deformation seen in the Bias Extension test for the yarns lock.
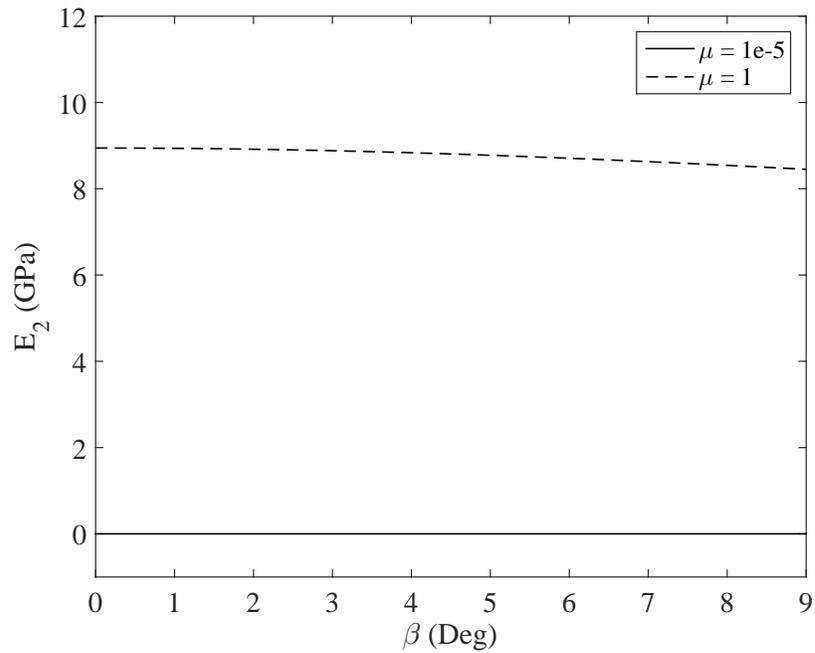
Figure 48: Comparison of Undulation Angle Influence on Homogenized Transverse Elastic Modulus in Free and Locked States

Figure 49 shows the in plane Poisson's ratio for homogenized RVC for varying initial undulation angles. Considering that, in the free state, E_1 and E_2 are approximately equal and invariant to changes in the undulation angle as well as G_{12} being effectively constant as a function of β, it follows that ν_{12} would be approximately one and invariant to changes in β. In the locked state, ν_{12} follows the other property trends by decreasing with increasing β, but takes on a value less than one due to the other properties being closer in magnitude.
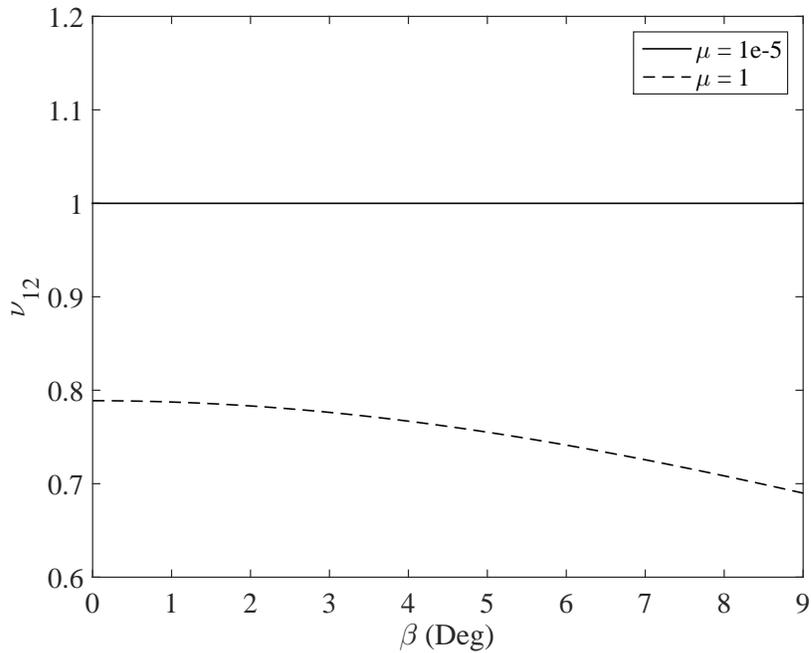
Figure 49: Comparison of Undulation Angle Influence on Homogenized In Plane Poisson's Ratio in Free and Locked States

When the yarns are oriented $[-45°,+45°]$ from the loading axis and the yarns are not locked, the shear properties of the RVC are lower and dominated by the shear moduli of the yarns. This is due to the discounting of the shear moduli with the parameter μ. In the transformed homogenized compliance matrix, the reciprocal of the entry in the last column and row is equal to the in plane shear modulus for the RVC. This entry is a function of the yarn's two elastic moduli, Poisson's ratio, in plane shear modulus, and braid angle. The result of multiplying the yarn's in plane shear

modulus by μ which approaches zero, is the inverse of that number is very large. Thus, it's contribution to the shear properties of the RVC is dominant. However, when the full shear modulus is regained, the shear properties are higher and are governed by the elastic moduli of the yarn. This is because all of the properties are within one order of magnitude of each other and the largest entry, which is the yarn's longitudinal elastic modulus, dominates the other's contribution. Figure 50 shows that the homogenized in plane shear modulus decreases with increasing undulation angle. Again, this effect is more noticeable when the yarn's are locked, but $\beta's$ effect is still present. In the free state, G_{12} increases rapidly near zero β due to trigonometric functions in the strain transformation matrix.
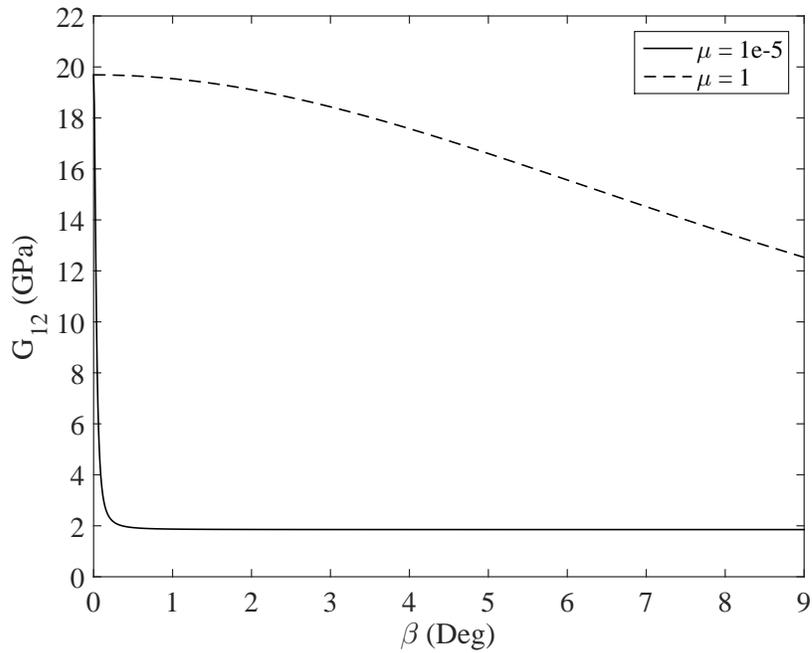
Figure 50: Comparison of Undulation Angle Influence on Homogenized In Plane Shear Modulus in Free and Locked States

Figures 51, 52, 53, and 54 show the homogenized in plane material properties as a function of the braid angle. Similar to Figures 47 and 48, Figures 51 and 52 show trends that are expected based on RVC orientation. Data is shown for free and locked states and shows little influence from changes in braid angle between 42 and 48°.

106
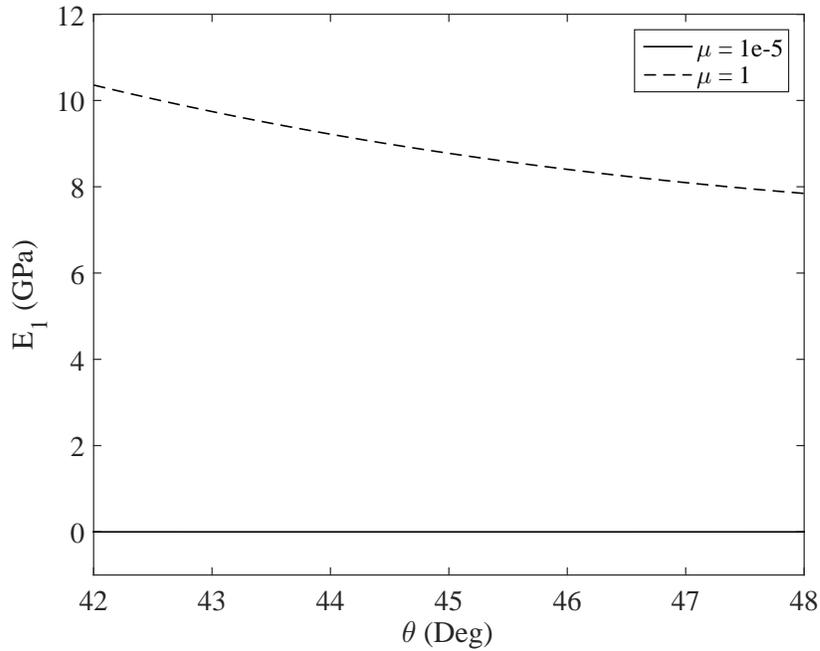
Figure 51: Comparison of Braid Angle Influence on Homogenized Longitudinal Elastic Modulus in Free and Locked States

Again, in the free state, the elastic moduli are small and in the MPa range. However, the trends with increasing and decreasing θ from the nominal value of 45° are opposite for E_1 and E_2. Once the yarns are rotated away from 90° from each other, they no longer contribute equally to the homogenized RVC longitudinal and transverse elastic moduli. As the yarns rotate toward one direction, they contribute more the stiffness in that direction and less to the perpendicular direction.

Figure 53 shows the in plane Poisson's ratio for homogenized RVC for varying initial braid angles. Considering that, in the free state, E_1 and E_2 are approximately equal and invariant to changes in the braid angle as well as G_{12} being effectively constant as a function of θ with the exception of near 45°, it follows that ν_{12} would be approximately one and invariant to changes in θ. However this is not the case, as Poisson's ratio increases with θ. While it is hard to observe from Figures 51 and 52 due to the magnitude differences, the two elastic moduli are changing with braid angle. In the locked stated, ν_{12} decreases with increasing braid angle. As the braid angle
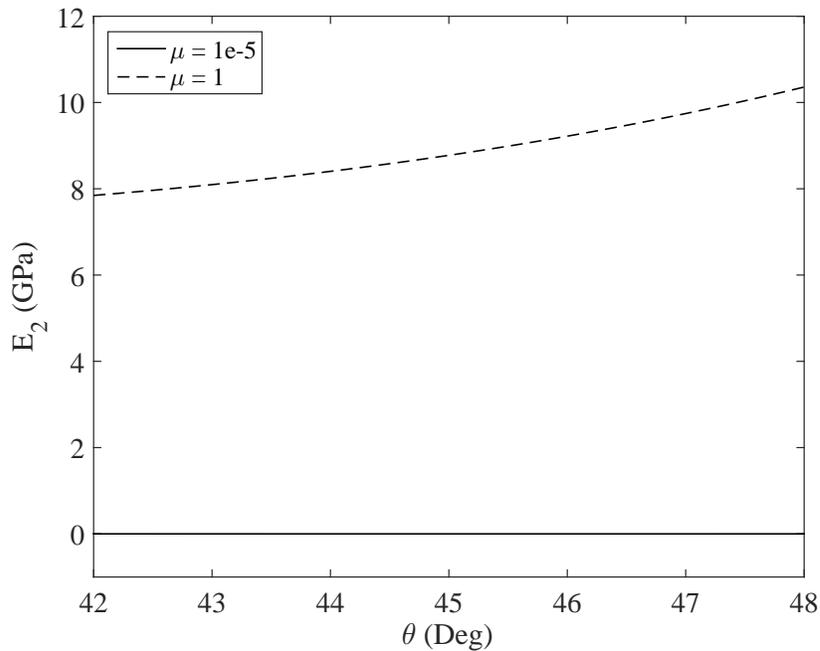
Figure 52: Comparison of Braid Angle Influence on Homogenized Transverse Elastic Modulus in Free and Locked States

increases, the yarns are rotated off the loading axis. This directs more of the yarn's longitudinal elastic modulus perpendicular to the loading axis, which then provides more resistance to transverse contraction resulting from longitudinal extension.

In the free state, the in-plane shear modulus of the homogenized RVC has a similar but more exaggerated trend as in the locked state as shown in Figure 54. The shear properties are maximum near $45°$ and decreases at angles away from nominal. Again in the free state, the shear properties of the RVC are lower and dominated by the shear moduli of the yarns. However, when the full shear modulus is regained, the shear properties are higher and are governed largely by elastic moduli of the yarn.

It should be noted that the trends discussed above are valid only for the RVC orientation and parameter ranges stated above. While the figures above correspond to bias loading, loading parallel to the yarn longitudinal axes would produce different trends. The previous discussion was focused on gaining insights for purposes of directing the sensitivity analysis before proceeding to the inverse analysis.
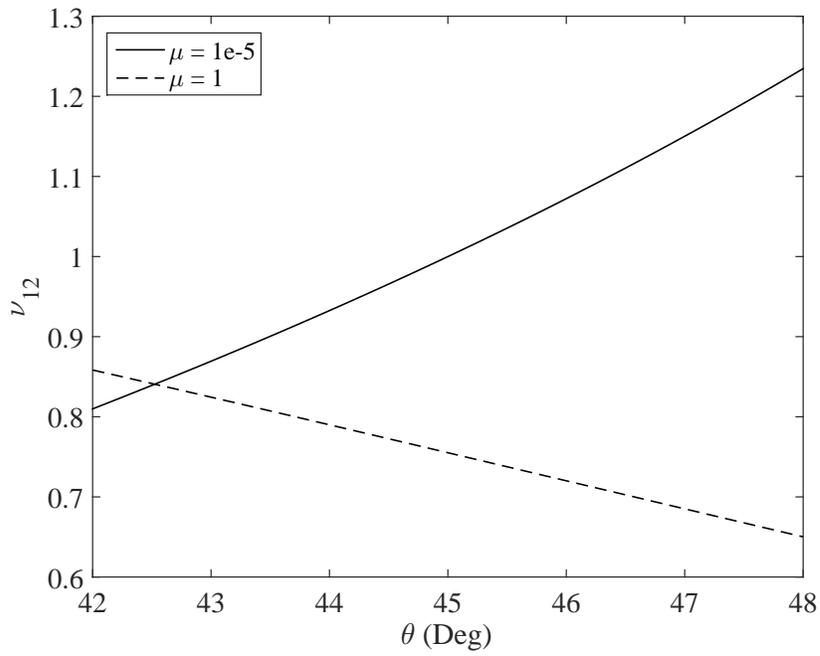
Figure 53: Comparison of Braid Angle Influence on Homogenized In Plane Poisson's Ratio in Free and Locked States
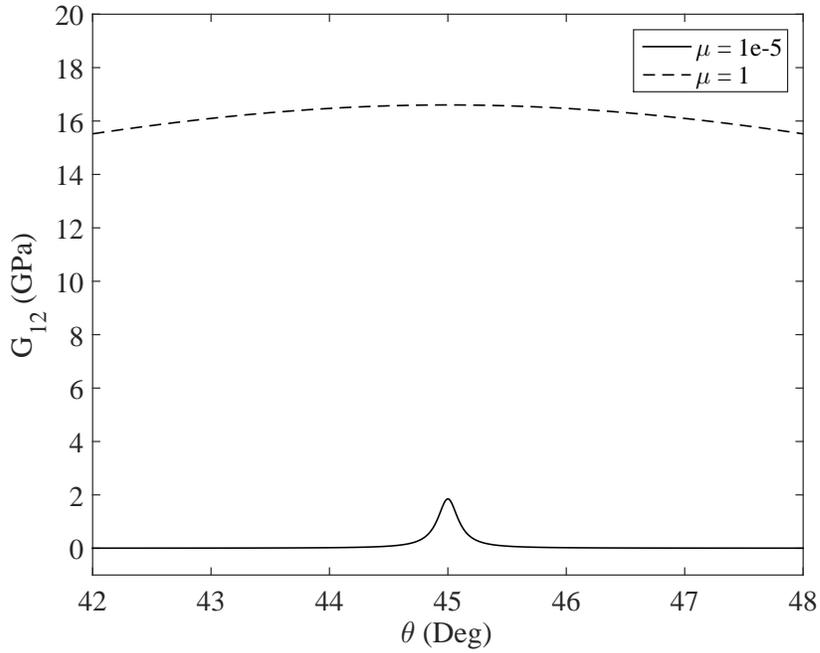
Figure 54: Comparison of Braid Angle Influence on Homogenized In Plane Shear Modulus in Free and Locked States

3.4 Sensitivity Analysis

Responses can depend on many variables, and the computational effort of an optimization strongly depends on the number of variables. In most cases, only a few variables are significant. Sensitivity analysis allows for the determination of the significance of design variables when computing a selected response. This helps to understand the simulation model and to reduce the design variables used in an optimization. The least significant ones can be neglected to reduce the computational effort. This filtering happens through variation of the variables and comparison of the response values. In a sensitivity analysis, usually rather large variable ranges are examined in order to reproduce design changes. The set of points is uniformly distributed on the design space (Space Filling or D-Optimal as examples).

Two sensitivity measures can be implemented in LS-OPT: Linear ANOVA and GSA. Both are global in nature and are evaluated using the metamodel. Thus, the metamodel quality is essential to achieve reasonable sensitivity results. ANOVA is a linear sensitivity measure, whereas GSA is non-linear. The results are comparable for linear metamodels. An advantage of GSA is, that the values are normalized. Hence they can be summed up to determine the influence of a parameter on multiple responses, on a full load case, or on the entire optimization problem. In this work, Sobol's GSA is implemented to filter variables.

As a first step, a single iteration is run using quadratic polynomial based metamodel to find the most sensitive parameters. With only one iteration, the total computational expense is comparatively much lower than the several iterations to convergence used in the inverse analysis. Thus, a higher order model is selected for the single iteration over a initial design space. There is also considerable practical experience indicating that quadratic models work well in solving real-world response surface problems. In this manner, a non-linear approximation is created across the

whole design space. The number of simulation points required to build the meta-model using the D-Optimal method increases from 22 in the linear case to 158 in the quadratic case.

The computed vs. predicted MSE is provided in Figure 55 along with the corresponding $R^2 \approx 0.994$. The computed and predicted pairs lie closely along a straight line. The straight line in the graph is a result of a least squares fit. This is usually a good indication that the model is satisfactory fit to the data.
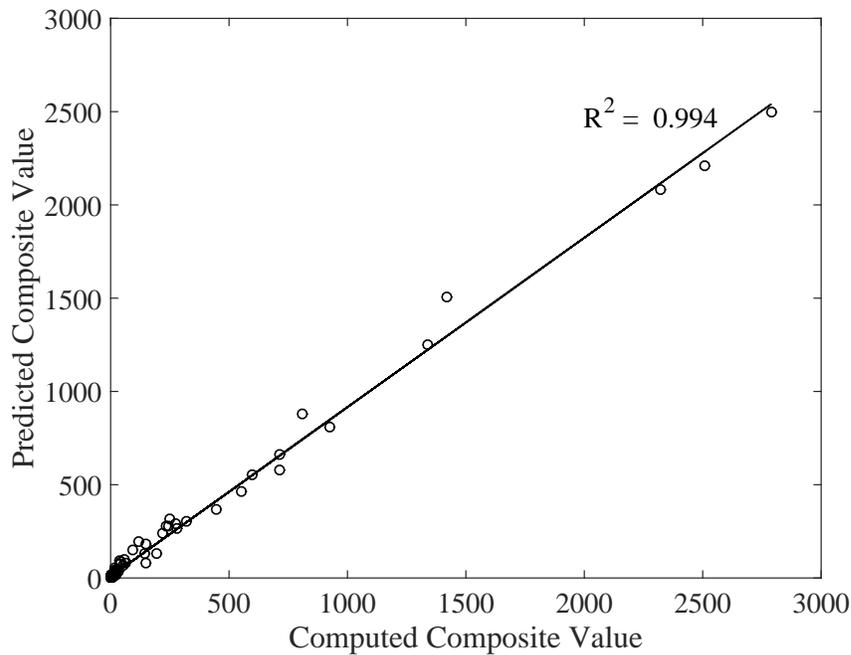
Figure 55: Comparison of Computed and Predicted Mean Square Error for Sensitivity Analysis

Figure 56 shows the global sensitivities for the MSE response. Each bar represents the contribution of a variable to the variance of the respective response (MSE). The values are normalized such that the sum of all displayed values is 100%. The values are sorted in descending order of contribution to the total variance. Approximately 93% of the total variance is attributed to the initial braid angle, locking angle, undulation angle, and reorientation damping coefficient. Thus, one case in the inverse analysis should be dedicated to estimating these four parameters while keeping the others
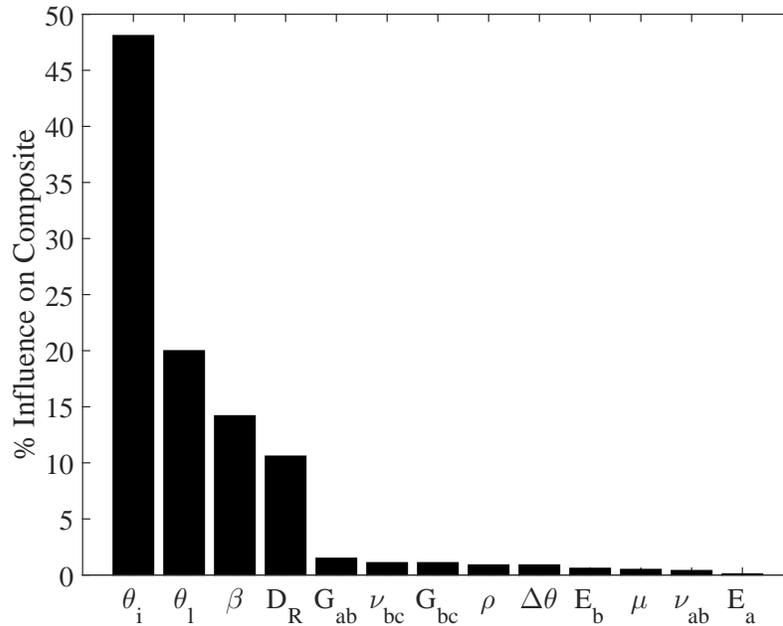
Figure 56: Percent Influence of Each Parameter on Total Mean Square Error

constant. As an initial check of these results, model theory can be utilized. The impact of the initial braid angle, locking angle, and undulation angle can be traced back to specific locations in model theory. As the load case for this study is that of the bias-extension, it makes sense that the fabric architecture would have a strong influence on the shear stress-strain response. However, the reorientation damping coefficient is not easily traced in model theory or even explicitly defined in literature. The LS-DYNA material model manual makes only one reference to the parameter by noting that the parameter is defined to damp some of the high frequency oscillations. With no physical attribute to map to, further sensitivity studies will be required to understand more about this parameter's impact on model behavior. Additionally, the response from which the sensitivities are calculated can be checked. In LS-OPT, sensitivities are calculated from the response surface. Because the response accuracy is dependent on the response type and parameter ranges, a poor model fit can lead to misleading sensitivities. Since this work is focused more on demonstrating the

methodology for a representative material, these checks on sensitivity calculations are saved for future work.

It should be noted that the trends discussed above are valid only for the RVC orientation and parameter ranges stated above. The sensitivities discussed above correspond to bias loading and the significant parameters for loading parallel to the yarn longitudinal axes would likely change. In the following section results from full parameter analyses are compared with those using a parameter subset.

3.5   Inverse Analysis

The purpose of inverse analysis is to provide a better match between the experimental test data and the finite element model predictions. This is accomplished by minimizing the mean square error objective function using the methods discussed in Appendix A. Using the sequential response surface method, the parameter identification results for various sets of parameters will be compared. The parameters used here are a subset of parameters identified from the sensitivity analysis. After identifying the appropriate subset of parameters using the results of the sensitivity analysis, a metamodel-based optimization is performed using a sequential response surface method with domain reduction and linear metamodels.

The are many options for selecting the initial parameter values and ranges to be used in the estimation process. The previous steps helped provide guidance for intelligent selection process. Considering the homogenization method's effect on the individual yarn material properties and initial yarn architecture, it is difficult to estimate these parameters simultaneously. In addition, without carrying out yarn material testing, it is difficult to find consistent material property data. In researching nominal values for the 200 denier Kevlar$^{®}$ 29 yarn's longitudinal elastic moduli, sources varied by as much as approximately 30%. However, with minimal testing, the 6 yarn material properties can typically be acquired to a higher confidence level

than the yarn architecture. The yarn architecture can be estimated from optical microscopy images, but the process of integrating the fabrics into larger structures can have a large impact on the final values.

Table 14 summarizes the initial input parameter values and ranges. As discussed in a previous section, the yarn material properties for the exact 200 denier Kevlar® 29 yarn were not available for this work. Several material databases were referenced in an effort to bound the likely ranges for the material properties. The nominal values were found in literature and the minimum and maximum values are based on differences other sources. The initial braid angle, locking angle, and undulation angle estimates were based on geometrical approximations combined with known fabric data. The remaining parameter estimates were based on nominal analyses and suggestions found in Reference [64].

Table 14: MAT_235 Initial Input Parameter Values and Ranges

Symbol	Value	Minimum	Maximum	Units
ρ	1.44	1.40	1.50	g/cm^3
E_1	61	50	70	GPa
E_2	4.2	2.7	5.7	GPa
G_{12}	2.9	1.9	3.9	GPa
G_{23}	2.9	1.9	5.0	GPa
ν_{12}	0.35	0.25	0.5	-
ν_{23}	0.35	0.25	0.5	-
θ_i	45	42	48	Deg
θ_l	7.5	6.5	8.5	Deg
β_{fi}	5	1	9	Deg
β_{wi}	5	1	9	Deg
μ	2e-4	1e-5	4e-4	-
D_R	1000	500	1500	-
$\Delta\theta$	2.75	0.50	5.00	Deg

Table 15 shows the 5 parameter identification analyses performed using different sets of estimated parameters. In all cases, the initial estimate for the parameter values was the nominal values and then the sequential domain reduction algorithm is employed to obtain a better estimate of these parameters by attempting to minimize the objective function. The first two cases attempt to estimate all parameters with the only difference being that the initial undulation angles are constrained to remain

114

equal in the second case. This decision was made in an attempt to reduce the number of parameters and is a reasonable constraint considering the manufacturing process.

Table 15: Summary of Parameter Identification Analyses

Case	Parameters	Description
	Initial	See Table 13
1	*All*	See Table 14
2	*All*	$\beta_f = \beta_w$
3	$\Delta\theta,\beta,\mu,\theta_i,\theta_l$	Constant Yarn Mat. Props
4	$\beta,\mu,\theta_i,\theta_l$	–
5	$\beta,D_R,\theta_i,\theta_l$	–

It can be clearly seen from cases $1 - 5$ in Table 16 that different parameter estimates can be obtained depending on what parameters are estimated. There is an improvement in the estimation seen by constraining the initial undulation angles to be the same. Cases 2 and 3 show consistent results from constraining yarn material properties to their nominal values. Cases 4 and 5 show only marginal increases in the MSE from reducing the number of parameters even further.

Table 16: Summary of Parameter Identification Results

Parameters	Initial	Case 1	Case 2	Case 3	Case 4	Case 5
ρ	1.44	1.469	1.479	*Nominal*	*Nominal*	*Nominal*
E_1	61	53.565	50.685	*Nominal*	*Nominal*	*Nominal*
E_2	4.2	4.433	4.336	*Nominal*	*Nominal*	*Nominal*
G_{12}	2.9	1.900	1.900	*Nominal*	*Nominal*	*Nominal*
G_{23}	2.9	4.914	4.481	*Nominal*	*Nominal*	*Nominal*
ν_{12}	0.35	0.437	0.401	*Nominal*	*Nominal*	*Nominal*
ν_{23}	0.35	0.286	0.385	*Nominal*	*Nominal*	*Nominal*
θ_i	45	45.985	47.021	47.230	47.484	47.058
θ_l	7.5	7.000	6.514	6.653	7.349	6.693
β_{fi}	5	3.696	1.369	1.113	1.005	1.680
β_{wi}	5	1.413	1.369	1.113	1.005	1.680
μ	2e-4	3.021e-4	2.331e-4	1.013e-4	6.397e-5	*Nominal*
D_R	1000	565	592	671	*Nominal*	646
$\Delta\theta$	2.75	1.450	3.255	5.000	*Nominal*	*Nominal*
$MSE\ (10^{-4})$	185.724	7.516	2.883	2.652	3.110	3.920

The load-displacement plots in Figures 57 and 58 show results for the Bias Extension test cases. Figure 57 illustrates the experimental test data compared to results using nominal parameters and the case 1 best estimate parameters. Figure 58 shows

the comparison for the best estimated parameters from cases 3 through 5. A closer match with the data is obtained through the parameter identification process. Similar results are seen with the subset of parameters as with the full set.
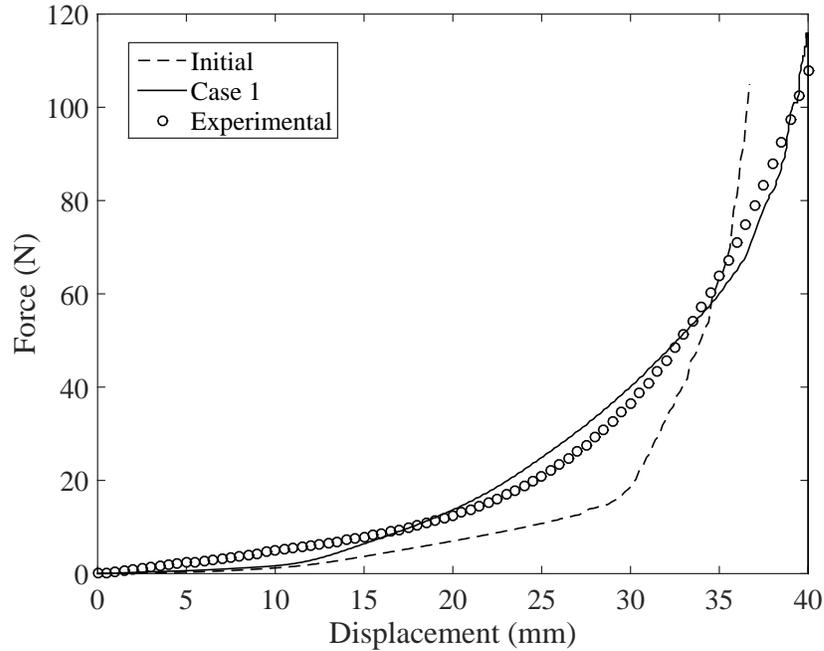
Figure 57: A Closer Match Between the Data and FEA Predictions Achieved Through the Inverse Analysis

In some cases multiple solutions will give the same or similar values for the objective function. This phenomenon often appears in under-defined parameter identification problems. The underlying problem is that of a singular system of equations having more than one solution. One symptom of non-uniqueness is different solutions are found having the same objective function values. Another symptom is the confidence interval for a non-linear regression problem is very large, signaling a singular system. An important check is that the test/target results are sufficient. It may be that the data set is large but that some of the parameters are insensitive to the functions corresponding to the data. As an example, cases 1-3 had confidence intervals that extended to plus and minus infinity. This is a signal that the problem is likely under-defined. As shown in Tables 17 and 18, by constraining the problem further
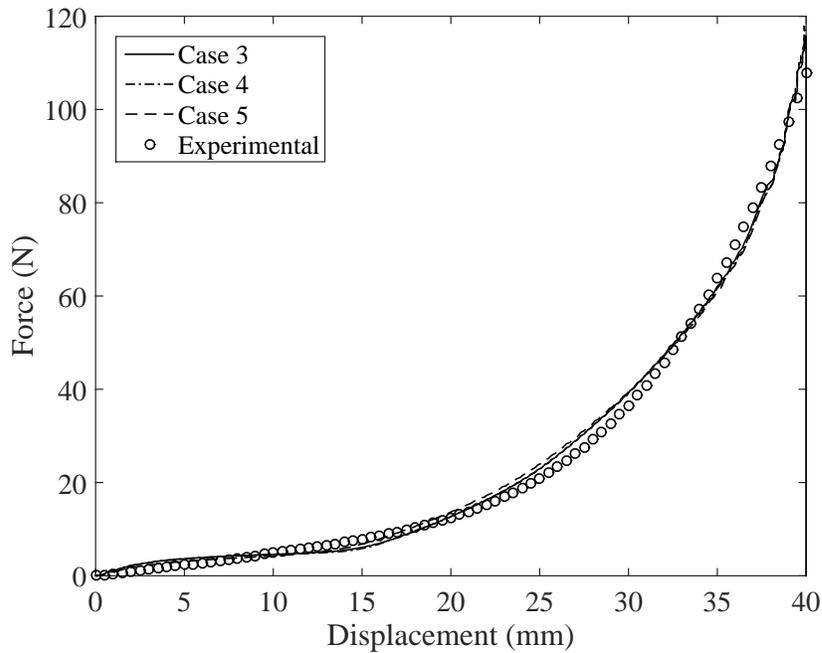
Figure 58: Close Agreement Between the Data and FEA Predictions Achieved Through the Inverse Analysis with Subset of Parameters

much lower confidence intervals exist for the remaining parameters.

Table 17: Case 4-95% Confidence Intervals for Individual Optimal Parameters

Name	Value	Lower	Upper
θ_i	47.484	47.370	47.598
θ_l	7.349	7.222	7.476
β	1.005	0.695	1.314
μ	6.397e-5	2.777e-5	1.002e-4

Inverse analyses were carried out to 20 iterations with the exception of Case 1 which was only carried out to 15 iterations. The maximum iterations were increased from 15 to 20 after analyzing the results from Case 1. The convergence in MSE is shown in Figure 59 with most cases showing convergence by 15 iterations. The initial behavior of all cases shown in the plot indicates a poorer model fit in the early iterations. As the design space is reduced in size, the linear metamodels improve in model fit and eventually converge to a solution.

Table 18: Case 5-95% Confidence Intervals for Individual Optimal Parameters

Name	Value	Lower	Upper
θ_i	47.058	46.931	47.186
θ_l	6.693	6.321	7.065
β	1.680	1.563	1.796
D_R	646	560	732
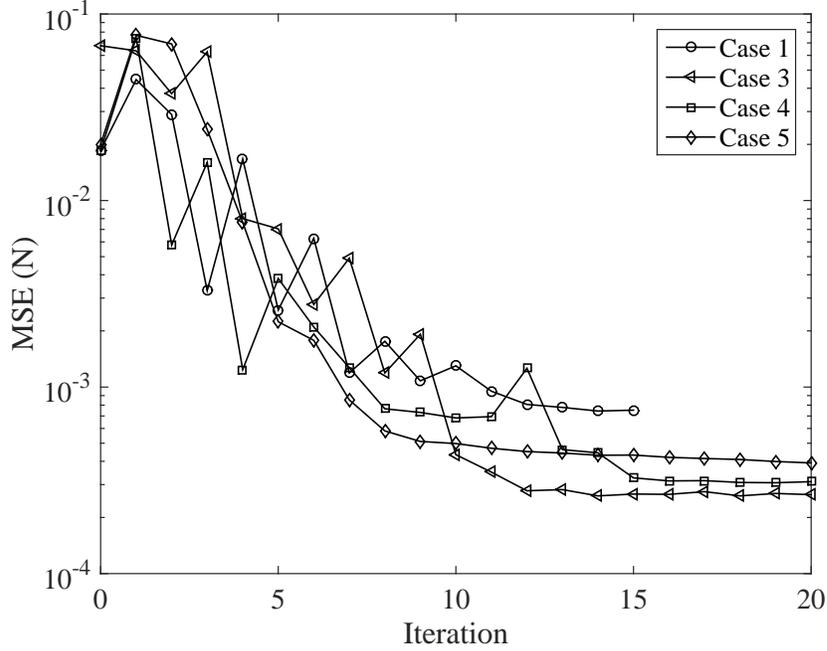
Figure 59: Convergence of Mean Square Error Between Test and Computed Curves for Multiple Cases

3.6 Summary

In this chapter, the parameter identification methodology is applied to a mesomechanical material model using a set of experimental test data. The model accounts for the reorientation of yarns and the fabric architecture. Fabric behavior is achieved by discounting the shear moduli of the material in the free state. The mesomechanical model is developed through a detailed presentation of homogenization method and yarn reorientation algorithm. The model is presented in more detail than, at the time of this writing, was found in any one literature source. In the nominal analysis, the model predictions are compared to the bias-extension data through a direct analysis

to identify where the model is fundamentally different than the experimental data. The available data is insufficient for purposes of studying the yarn locking behavior. Simulated data is used to extend the experimental force-displacement curve in to the locking region.

The homogenization process is studied to gain insights into effective material property sensitivity to changes in input parameters. The model shows effective material properties that vary with undulation and and initial braid angle. In addition, the discount factor is shown to have a significant impact on model behavior. In the sensitivity analysis, the contribution of each variable to the variance of the response is calculated. Based on the information provided in the previous steps, an inverse analysis is performed to obtain an accurate match between the model predictions and the data through estimation of input parameters. The inverse analysis was performed for many different parameter subsets to illustrate the advantage of the methodology as compared to the traditional direct approach. Results show a significant improvement in the matching between the model predictions and the data.

CHAPTER IV

NUMERICAL DETERMINATION OF MECHANICAL PROPERTIES FOR FLEXIBLE MATERIAL SYSTEMS

4.1   Introduction

A methodology is explored that involves homogenizing a unit cell in a manner such that the yarn mechanics are accounted for prior to the global simulation of a larger model. This is in contrast to the LS-DYNA MAT_235 mesomechanical model utilized in Chapter 3 that accounts for yarn mechanics at each time step of the simulation. By modeling a small, but detailed, unit cell of the fabric at the meso level and then applying a homogenization method to produce the material properties that can be applied to a membrane element, the nonlinear and stress state dependent behavior of the fabric can be captured without sacrificing computational cost. In addition, this methodology is not limited to the plain woven and biaxial braided fabric architectures like MAT_235, but can be applied to many fabric architectures. The process begins with measurements of geometrical parameters obtained from optical microscopy. Next, the fabric architecture is replicated at the meso scale within a detailed 3D unit cell (RVC) model. Material models of the yarn and coating are applied to the unit cell. A combination of specified displacements and periodic boundary conditions are applied to this model and the resulting reaction forces are extracted from the numerical testing. The unit cell force-displacement relationship is correlated to a membrane element. The homogenized element can then be applied to a large scale model. This methodology requires some knowledge of the expected state of stress over the large scale structure, but has the benefit of reducing the amount of experimental testing required to characterize the fabric at several states of stress

and could eventually bring higher fidelity structural models for IADs forward in the design process. Furthermore, not only is the amount of experimental testing reduced, the type of testing (yarn vs. fabric) allows the results to be applicable to multiple fabric architectures. This has the potential effect of increasing the speed between iterations be reducing additional testing between design cycles. The yarn geometrical and mechanical property measurements which take the most time to obtain in this methodology (days) are front loaded, while the remaining steps are governed by computational resources.

In a similar manner to Chapters 2 and 3, this work relies on experimental data for validation. In contrast though, a Urethane Coated Plain Woven 400 Denier Kevlar® 49 Fabric is utilized. The switch from the fabric used in previous chapters was made due to availability of physical fabric samples for measurement of geometric parameters. Table 19 summarizes properties of the fabric used for IAD testing in [4]. In addition, uniaxial extension and inflated cylinder tests were carried out on the Kevlar® 49 fabric [26]. These results are used for validation of the methodology.

Table 19: Properties of Urethane Coated Plain Woven Kevlar® Fabric

Denier	TPI	Coated Areal Density (oz/yd^2)	Coated Thickness (in)
400	36	11.1	0.01315

These properties alone are not sufficient to model the yarn geometry and weave architecture. Optical microscopy measurements are taken of fabric samples to construct a unit cell model. The next section presents the development unit cell geometric and finite element models.

4.2 Unit Cell

A mesomechanical approach captures the actual yarn geometry and weave architecture by modeling individual yarns and the weave pattern with solid finite elements.

121

The fabric geometry and material properties of a single yarn in an undeformed state are needed to build the finite element model. To obtain the appropriate weave architecture, a novel procedure is employed. High resolution images are used to provide a microscopic view of the yarn geometry.

4.2.1 Geometry Computation

The geometric description in Figure 74 for the plain woven fabric used by McBride and Chen defines four sinusoidal curves, shown in Equation (63), in terms of the yarn width, w, yarn spacing, s, and yarn thickness, h to represent the periodic pattern of the textile [85]. Using these three values the periodic nature can be modeled in the unit cell.
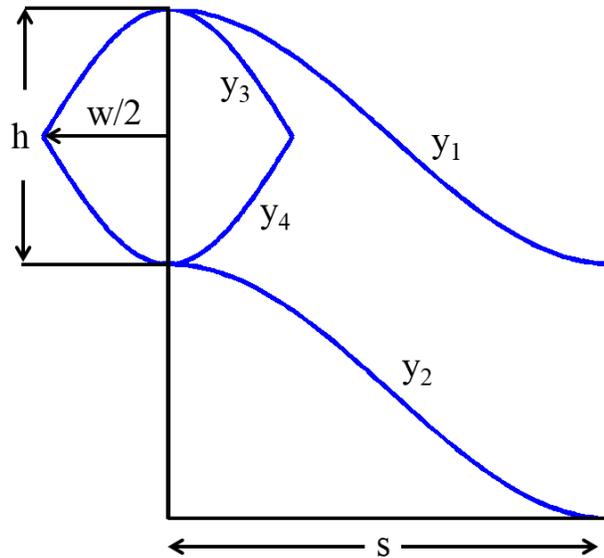
Figure 60: Unit Cell Geometry

The cross-sections of the yarns are approximated as circular arcs. The characteristic values of w, s, and h shown in Table 20 are averaged from 30 total measurements. The value t refers to the total fabric thickness, including coating. The method for taking the fabric measurements and data processing as discussed in Appendix C.

$$y_1 = \frac{h}{2}\left[\cos\left(\frac{\pi x}{s}\right) + 1\right]$$
$$y_2 = \frac{h}{2}\left[\cos\left(\frac{\pi x}{s}\right) - 1\right]$$
$$y_3 = \frac{h}{2}\left[\cos\left(\frac{\pi x}{w}\right) + 1\right] \tag{63}$$
$$y_4 = \frac{h}{2}\left[\cos\left(\frac{\pi x}{w} - \pi\right) + 1\right]$$

In comparing Table 20 with Table 19, a difference of approximately 46% in fabric thickness is observed between the value referenced in [4] and that measured directly. Fabric thickness measurement can be problematic due to the high level of fabric compressibility. The thickness obtained is highly sensitive to the amount of pressure applied during measurement. As the method of measurement of thickness taken from literature is unclear, this work will rely on that taken from direct optical measurements. The warp and weft measurements shown in Appendix C were quite close and as a means of simplifying the modeling process, were homogenized to arrive at a balanced plain weave model. The five measurements each in the warp and weft directions were averaged and the resulting values shown in Table 20.

Table 20: Characteristic Yarn Values from Fabric Image Measurements

w (mm)	s (mm)	h (mm)	t (mm)
0.5621	0.7223	0.091	0.3715

4.2.2 Geometric Modeling

In this work, the fabric geometry, shown in Figure 61, is generated using TexGen in combination with the characteristic yarn values in Table 20. TexGen is an open source software tool developed at the University of Nottingham for modeling the geometry of textile structures [86].

123
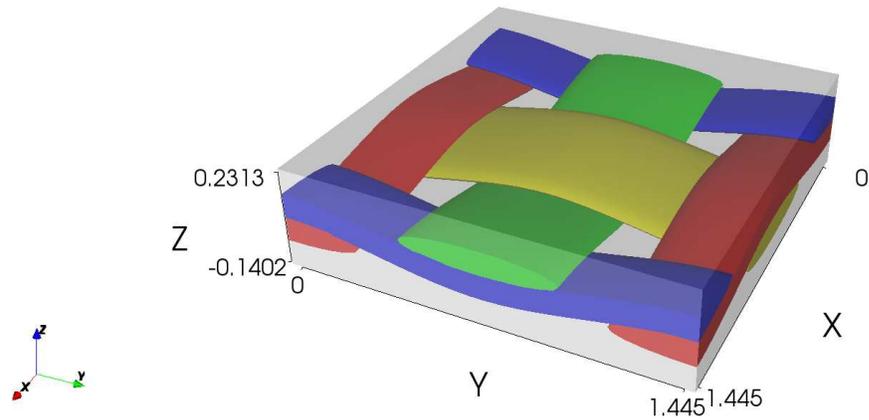
Figure 61: 400 Denier Kevlar® 49 Plain Woven Fabric RVE Created Using TexGen

Once a model has been specified as described above it can be meshed to proceed with analysis. Dry fiber volume meshes can be created in TexGen using tetrahedral and hexahedral elements as illustrated in Figures 62 and 63, respectively. When both the yarns and matrix are required to be meshed a tetrahedral mesh is created. Views of the resulting yarn and combined yarn/matrix tetrahedral meshes are shown in Figure 62.

(a) With Matrix

(b) Without Matrix
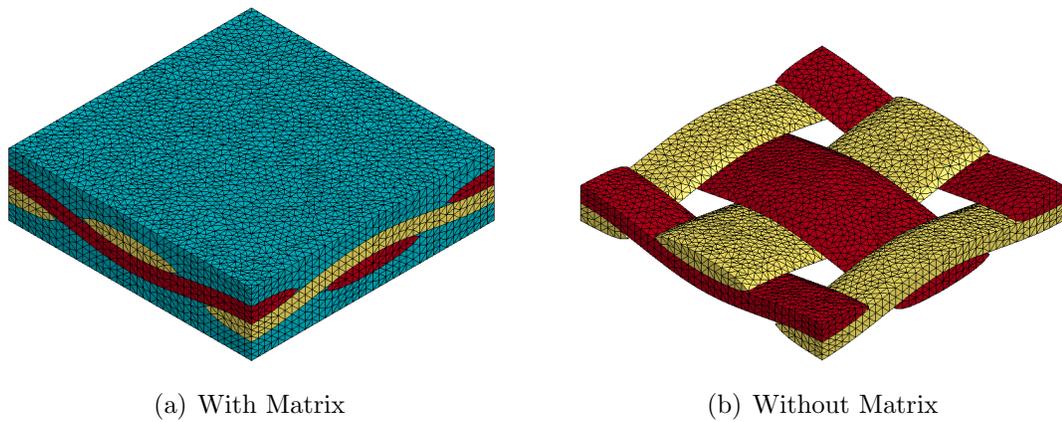
Figure 62: 4 Noded Tetrahedral Elements - Volume Mesh

Generation of conformal meshes can be challenging for textile geometries. In particular, close to yarn crossovers it is often difficult or impossible to generate elements

of acceptable quality that conform to the local yarn surfaces. Furthermore, utilizing tetrahedral elements adds difficulty in specifying proper material directions for the non-isotropic yarns. Uniform hexahedral meshes are better suited for controlling material directions of the yarns.
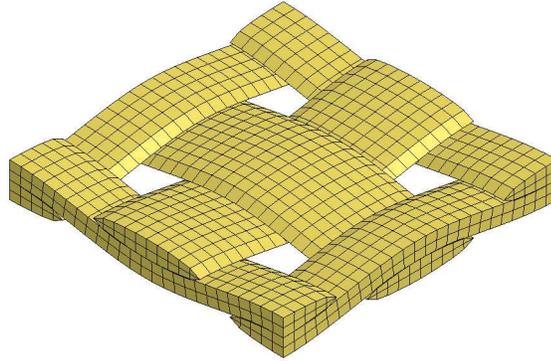
Figure 63: 8 Noded Hexahedral Elements - Volume Mesh

The geometry can also be discretized with a regular pattern of 8-node hexahedral finite elements. This pattern is known as a voxel mesh (volume and pixel). Each element is assigned to the material of the phase where its center is located: either in the matrix material or in the homogenized yarn material. In the latter case, the local orientation is mapped from the geometry to the yarn element. Such a voxel mesh is illustrated on Figure 64, shown with and without the matrix elements.
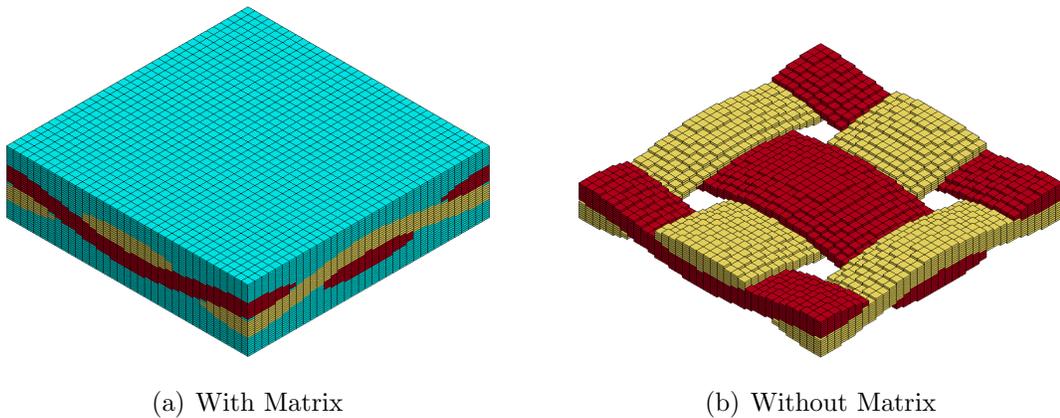
(a) With Matrix (b) Without Matrix

Figure 64: 8 Noded Hexahedral Elements - Voxel Mesh

In a voxel mesh, the boundary between the matrix element set and the yarn element set is a patch of rectangular facets that are parallel to one of the RVC faces. It may then be regarded as a less accurate approximation to the RVC inner surfaces than the one that would be obtained with a usual tetrahedral mesh generator with nodes exactly on the surfaces. This approach is more robust than that alternative which can lead to poorly-shaped tetrahedral elements in areas between yarns or close to yarn crossings. Moreover, the resulting finite element stiffness matrix has a smaller bandwidth and a better conditioning number than with a conventional mesh. The linear systems to be solved are well suited to iterative solvers, which have been found to be computationally efficient in this work. Consequently, models with small element edges, which represent the geometry sufficiently well, may be solved in a moderate CPU time.

When the fabric demonstrates a large degree of yarn reorientation in shear loading, the 8 noded hexahedral element based volume mesh approach is recommended. The smoother surface obtained from the nodes being exactly on the surfaces allows for better modeling of the rotations. However, when a matrix or coating restricts the reorientation, this attribute is less significant and a voxel mesh is sufficient to provide accurate results. Remaining simulations are performed using a voxel mesh.

4.3   Numerical Tests on Unit Cell

Numerical tests such as uniaxial and trellising are conducted on the unit cell for the determination of the effective material properties for a membrane element. Two methods are presented for obtaining the effective mechanical stiffness matrix. The first is a linear approach in which the macro complaince matric, $\mathbf{S}$ is obtained by inverting the macro stiffness matrix, $\mathbf{C}$ and, by definition, effective linear material properties can be computed. In the second appraoch, the nonlinear mechanical stiffness matrix will be iteratively modified and imposed on a membrane element in each

increment of the finite element analysis to match the force-displacement curves of the unit cell obtained from numerical tests. The same displacement as the unit cell will be prescribed on a membrane element at each increment.

4.3.1 Material Modeling

At present, it is not feasible to simulate each fiber using an FEM approach. In this work, the yarns are considered as orthotropic solid bodies. The longitudinal direction is defined by (11), which is parallel to the fibers; the transverse plane is described by directions (22) and (33), which are characterized by a plane of isotropy at every point in the yarn. The orthotropic behavior of the yarn is described using a 3D stiffness matrix containing up to nine independent constants. Data for all the 400 Denier Kevlar® 49 yarn elastic constants are not available in the literature. Baseline material estimates as shown in Table 21 are defined consistent with those found in literature [84] and [64]. Matrix estimates are consistent with urethane rubber coatings. The accuracy of these values is unknown and are consider rough estimates. Future studies would benefit from dedicated yarn material testing to support simulations.

Table 21: Estimate Yarn and Matric Elastic Constants

Yarn	E_{11}	E_{22}	E_{33}	G_{12}	G_{13}	G_{23}	ν_{12}	ν_{13}	ν_{23}
Property (GPa)	135	7.4	7.4	2.5	2.5	5	0.2	0.2	0.2
Matrix	E	ν							
Property (MPa)	3	0.2							

Since yarns are highly anisotropic materials, an important point is to define material orientation and to specify the mechanical characteristics in the appropriate directions during simulations. A local orthogonal material coordinate system is defined for material properties. The material coordinate system is defined by specifying an angle, β, relative to the local element coordinate system; which is defined by element connectivity.

4.3.2 Boundary Conditions

Fabric unit cell modeling is based on the assumption that fabric deformation is uniform at the meso scale. Periodic boundary conditions are applied to replicate the repeating nature of the fabric. Since plain woven fabrics can be treated as a periodical array of unit cells, the PBC devised by Xia et al. is applied on the unit cell to ensure that there is continuity between neighboring cells [87]. Since the periodic array of the unit cell represents a continuous physical body, two continuities must be satisfied at the boundaries of the neighboring unit cells. One is that the displacement must be continuous. In other words, neighboring unit cells cannot be separated or overlap after deformation. The second condition implies that the traction distributions at the opposite parallel boundaries of a unit cell must be the same. From this, the individual unit cells can be assembled as a continuous body.

The solution obtained by applying unified displacement-difference periodic boundary conditions, in a displacement-based finite element analysis, will also meet the traction continuity conditions. All the boundary pairs match each other exactly, which is a necessary condition for applying periodic boundary conditions. When generating the mesh, special attention is paid on the node locations on all boundary pairs so that the node pairs can be found and constrained. By applying the periodic boundary conditions and using Equation (64), the constraints can be imposed on any arbitrary node pair.

$$u_i\big(0, y, z\big) - u_i\big(l, y, z\big) = \bar{\epsilon}_{ij} \times \big[l, 0, 0\big]_j$$
$$u_i\big(x, 0, z\big) - u_i\big(x, w, z\big) = \bar{\epsilon}_{ij} \times \big[0, w, 0\big]_j$$
$$u_i\big(x, y, 0\big) - u_i\big(x, y, t\big) = \bar{\epsilon}_{ij} \times \big[0, 0, t\big]_j$$
$$\big(i, j = 1, 2, 3; \ 0 \le x \le l; \ 0 \le y \le w; \ 0 \le z \le t\big)$$

(64)

where, u_i denotes the displacement along the i direction; l, w, and t, respectively,

denote the length, width, and thickness of the unit cell. The global strain $\bar{\epsilon}_{ij}$ is exerted on the unit cell.

4.3.3 Loading Conditions

The mechanical behavior of the unit cells under tensile strain and in-plain shear strain are analyzed in the following sections. First, the specific loading conditions are discussed along with method for effective material property calculation.

4.3.3.1 Uniaxial Loading

The prescribed deformation applied on the RVC for the uniaxial tension in warp and weft directions are shown in Equation (65), where the word *unprescribed* in the deformation gradient implies that the RVC is free to contract or expand in the corresponding direction. The RVC is imposed by the periodic boundary conditions. As part of the PBC, master nodes were defined on the global y axis and z axis. These master nodes were employed in the PBC to allow the strain in those directions to be unprescribed, but still constrain all the boundary pairs match each other exactly. As stated in Appendix C, the measurements of the fabric were averaged in the warp and weft directions. Thus, only one case of uniaxial tension is required for this analysis and the orthogonal direction is assumed to be identical.

$$\mathbf{F}_{uniaxial} = \begin{bmatrix} 1 + \epsilon_{xx} & \epsilon_{xy} & \epsilon_{xz} \\ \epsilon_{yx} & 1 + \epsilon_{yy} & \epsilon_{yz} \\ \epsilon_{zx} & \epsilon_{zy} & 1 + \epsilon_{zz} \end{bmatrix} = \begin{bmatrix} 1 + \epsilon_{xx} & 0 & 0 \\ 0 & unprescribed & 0 \\ 0 & 0 & unprescribed \end{bmatrix}$$
(65)

Figure 65 provides an example of how a unit cell is loaded in uniaxial tension. The figure shows a cube of material with a load F_x applied on one of the faces along the x-direction. Assume that the face coincident with the y-z plane is constrained to in-plane motion. In addition, the corner at the origin of the coordinate system is

completely fixed. One other constraint is necessary to stop this model from rotating about the x-axis. As a result of these constraints and loading, the cube face displaces along the x-axis by some amount δ. Due to the Poisson effect, the cube will displace in the y and z directions as well. However, those displacements do not need to be prescribed. The applied force and resulting displacement can then be mapped to stress and strain on the cube.
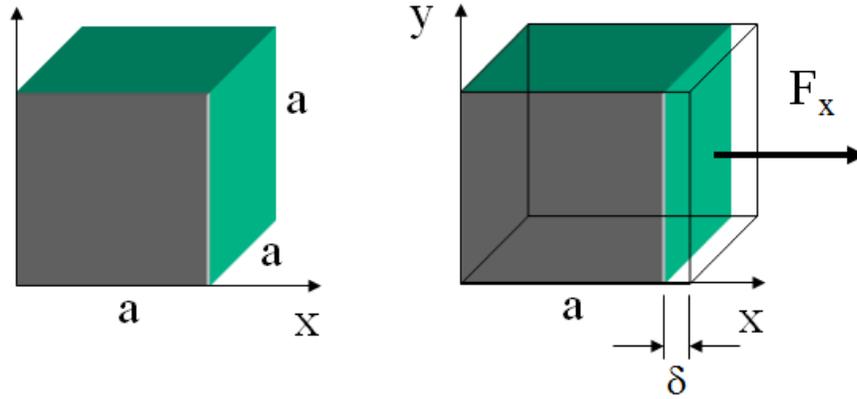
Figure 65: Cube of Material Under Uniaxial Tension

4.3.3.2 Shear Loading

The prescribed in-plane shear deformation applied to the RVC is shown in Equation (66), where the word *unprescribed* in the deformation gradient implies that the RVC is free to contract or expand in the corresponding direction. Compared to the uniaxial tension case, the RVC is imposed by the different PBC. As part of the PBC, master nodes were defined on the global y axis and z axis. These master nodes were employed in the PBC to allow the strain in those directions to be unprescribed, but still constrain all the boundary pairs match each other exactly.

$$\mathbf{F}_{shear} = \begin{bmatrix} 1+\epsilon_{xx} & \epsilon_{xy} & \epsilon_{xz} \\ \epsilon_{yx} & 1+\epsilon_{yy} & \epsilon_{yz} \\ \epsilon_{zx} & \epsilon_{zy} & 1+\epsilon_{zz} \end{bmatrix} = \begin{bmatrix} 0 & \epsilon_{xy} & 0 \\ \epsilon_{yx} & 0 & 0 \\ 0 & 0 & unprescribed \end{bmatrix} \tag{66}$$

130

Figure 66 provides an example of how a unit cell is loaded in in-plane shear. The figure shows a cube of material with a shear stress τ_{xy} applied on one of the faces along the y-direction. Assume that the face coincident with the y-z plane is constrained to in-plane motion. In addition, the corner at the origin of the coordinate system is completely fixed. One other constraint is necessary to stop this model from rotating about the x-axis. As a result of these constraints and loading, the cube face displaces along the y-axis by some amount δ. Due to the Poisson effect, the cube will displace in the z directions as well. However, this displacement is not prescribed. For small angles, the shear strain γ_{xy} for this cube can be approximated as δ/a. This is just one example of how pure in-plane shear can be applied to a unit cell.
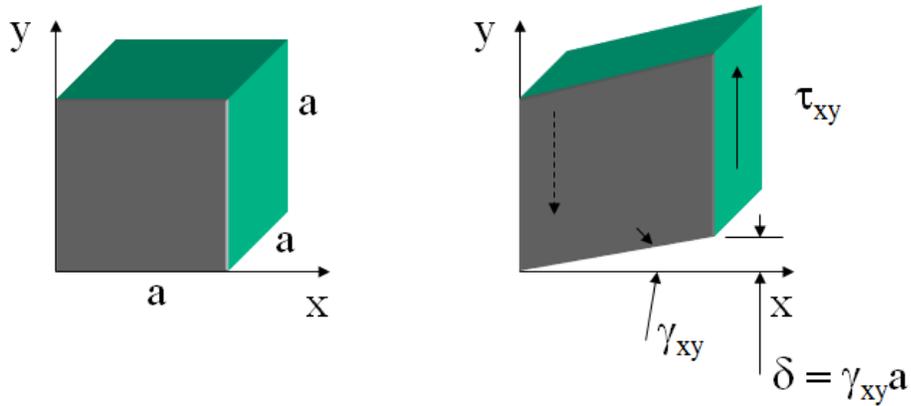
Figure 66: Cube of Material Under Shear Stress

4.3.3.3 Effective Material Property Calculation

For a full 6 × 6 stiffness matrix, six different cases must be run, and each case will be assigned the above-mentioned PBC as well as a unit strain in a certain direction. For the simplification of plane stress, where the stresses in the z-direction are considered negligible, $\sigma_{zz} = \sigma_{yz} = \sigma_{xz} = 0$, the stress-strain stiffness relationship for orthotropic materials reduces to that shown in Equation (67). From this simplification, the number of cases required reduces to three. Each case gives one column of the stiffness matrix. After completing the stiffness matrix, the compliance matrix can be obtained

by inverting the stiffness matrix, from which all engineering constants can be computed as shown in Equation (68). A further simplification can be made by assuming that the $E_x = E_y$ (as is the case in this work). Based on this assumption, only two cases are required to obtain the all the necessary engineering constants.

$$\begin{Bmatrix} \bar{\sigma}_x \\ \bar{\sigma}_y \\ \bar{\sigma}_{xy} \end{Bmatrix} = \begin{bmatrix} C_{11} & C_{12} & 0 \\ C_{12} & C_{22} & 0 \\ 0 & 0 & C_{66} \end{bmatrix} \begin{Bmatrix} \bar{\epsilon}_x \\ \bar{\epsilon}_y \\ \bar{\gamma}_{xy} \end{Bmatrix} \tag{67}$$

$$E_x = \frac{1}{S_{11}}, \quad E_y = \frac{1}{S_{22}}, \quad \nu_{xy} = -\frac{S_{12}}{S_{11}}, \quad and \quad G_{xy} = \frac{1}{S_{66}} \tag{68}$$

4.3.4   Results

The warp and weft yarns, as well as the matrix (coating), were meshed with 8-node 3D linear hexahedral (brick) elements. According the periodicity characteristic of the fabric, the RVC us meshed such that the corresponding opposite surfaces (left and right; front and back; top and bottom) are discretized into equivalent distribution of nodes.

In practice, the interface debonding between the fiber and matrix can occur during the fabrication process (due to the mismatch of their thermal expansion coefficients). However, the interface debonding between the fiber and matrix is not considered in this work because the microstructure constituted of the fibers and the matrix within the yarn is not modeled, as explained earlier. Therefore, the nodes between the yarns and matrix interfaces are merged in order to simulate the perfect bonding between both volumes. Moreover, the perfect bonding is justified to reduce the computational cost and time, since the interface formulation can increase the cost and time.

Four levels of meshes are created for the textile RVC, from level 1 (coarse) to level 4 (fine), for obtaining the optimum meshed RVC in terms of the accuracy of analysis results and CPU time. Figure 67 shows the range of mesh densities of the matrix

volume and yarns volume. Table 22 shows the number of nodes, number of elements, total number of degrees of freedom (DOF), and the relative CPU time for the analysis (uniaxial tension) in each mesh density level.

(a) 8000 Elements   (b) 74088 Elements
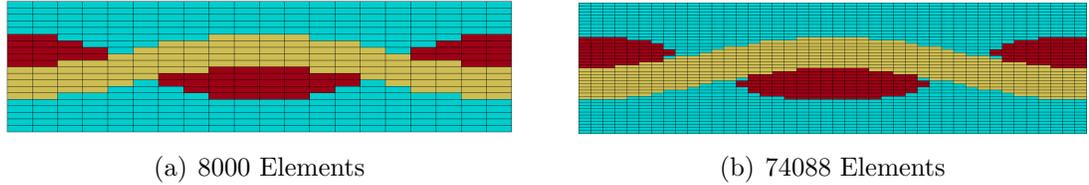
Figure 67: Comparison Between Course and Fine Voxel Meshes

The deformation gradient matrix, F shown in Equations (65) and (66), is applied on the RVC for prescribing the total deformation through the displacement of a defined *control node* and imposed by the PBC. The control node is defined by creating an additional node not tied to the unit cell geometry. The amount of displacement prescribed for the uniaxial and shear cases is defined to be consistent with the experimental results used for validation [26]. The subscripts x, y, and z are denoted for the directions of the axes on the global coordinate system. The material properties of the yarns are considered transversely anisotropic defined by a local material coordinate system and the matrix (coating) is considered to be isotropic as described in Section 4.3.1.

Table 22: Textile RVE Mesh Statistics

Mesh Density Level	Number of Nodes	Number of Elements	Degrees of Freedom	Relative CPU Time
1 (coarse)	9261	8000	27783	1
2	19683	17576	59049	3.55
3	42875	39304	128625	14.36
4 (fine)	79507	74088	238521	45.44

Figure 68 shows the analysis results (maximum Von Mises stress) for varying mesh density levels. Table 22 shows the relative CPU time for each mesh level. There is a clear difference between the coarse mesh (level 1) and the other meshes, however the

mesh density level 3 and level 4 (fine) show very similar results. Furthermore, the maximum Von Mises stress for each mesh density level provides sufficient maximum equivalent stress compared to level 4. The mesh density level 3 gives a much lower relative CPU time compared to the finest mesh. Thus, it can be concluded from Figure 68 and Table 22 that the mesh density level 3 is sufficient to provide accurate results. Remaining simulations are performed using mesh density level 3. The shear loading case utilizes the same mesh density due to the same conclusion.
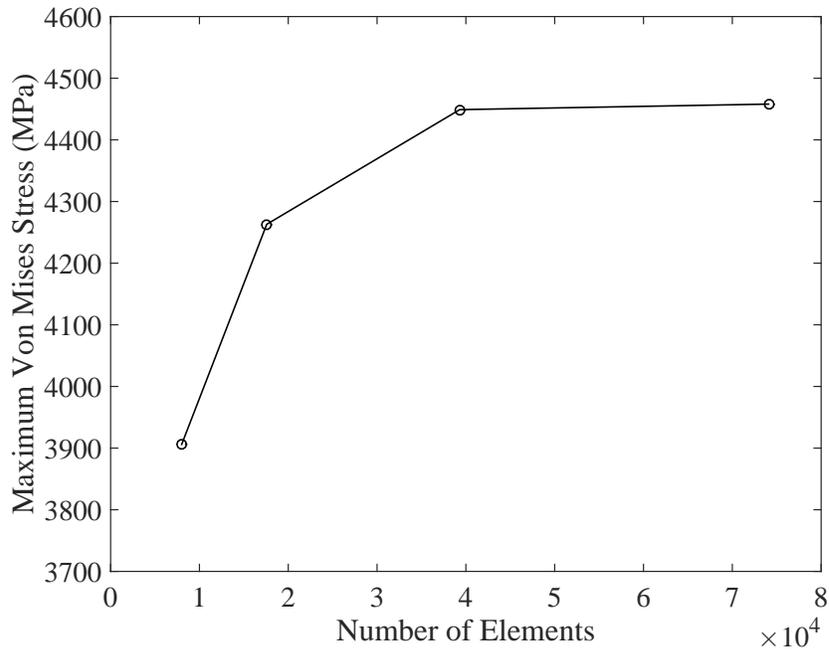
Figure 68: Von Mises Stress Vs. Number of Elements

The reaction force on the unit cell as a result of uniaxial displacement u_x is shown in Figure 69. The plot shows a linear relationship between force and displacement. Using the transformations in Appendix B, the results can be converted to PKII stress and Green strain. It is observed that this model does not capture the decrimping behavior typically seen in the low strain region of fabrics under uniaxial load. This is explained by referring back to Section 1.3.3. The decrimping of the fabric is a product of the yarns initially sliding over one another with resistance due to friction.

As discussed earlier, the nodes between the yarns and matrix interfaces are merged in order to simulate the perfect bonding. This prevents the unit cell from capturing the decrimping phenomenon. Modeling the decrimping process can achieved by not merging the nodes and defining contact conditions between the yarns and coating. The comes at the cost of increased computational expense.
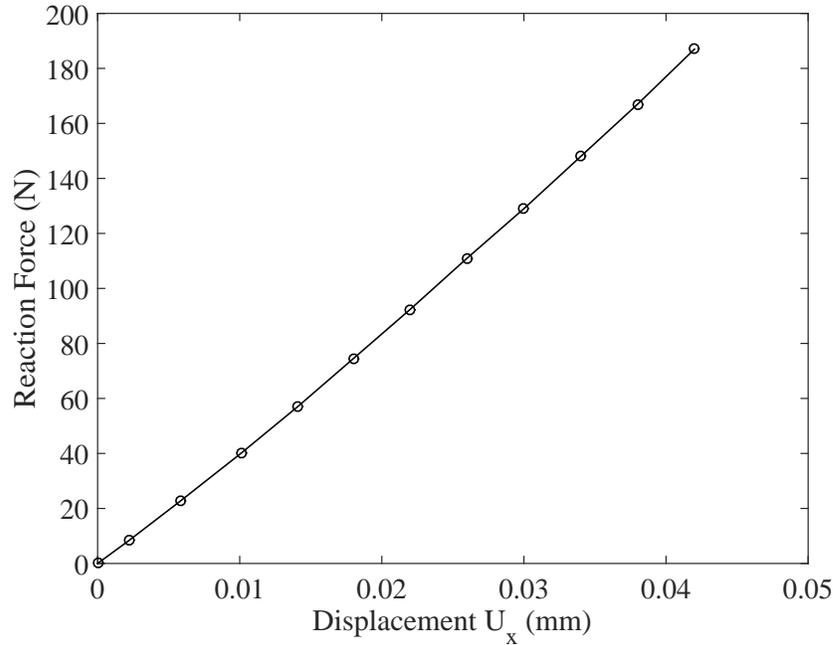
Figure 69: Reaction Force Vs. Displacement U_x

The Poisson effect in the unit cell is shown in Figure 70 with the contraction of the unit cell in the y-direction as a result from extension in the x-direction. As expected, the contraction is much smaller in magnitude than the extension. From Section 1.3.3, the yarns under load will begin to straighten which decreases their crimp heights and elongates their effective lengths. As a result, the perpendicular family are forced to increase their crimp heights and decrease their effective lengths. This change in crimp height is referred to as crimp interchange and is often compared to the Poisson's effect from continuum mechanics. As shown in [25], plain woven fabrics can exhibit effective Poisson's ratios greater than 1. Similar to decrimping, the nodes between the yarns

135

and matrix interfaces being merged limits that amount of lateral contraction in the unit cell due to longitudinal extension.
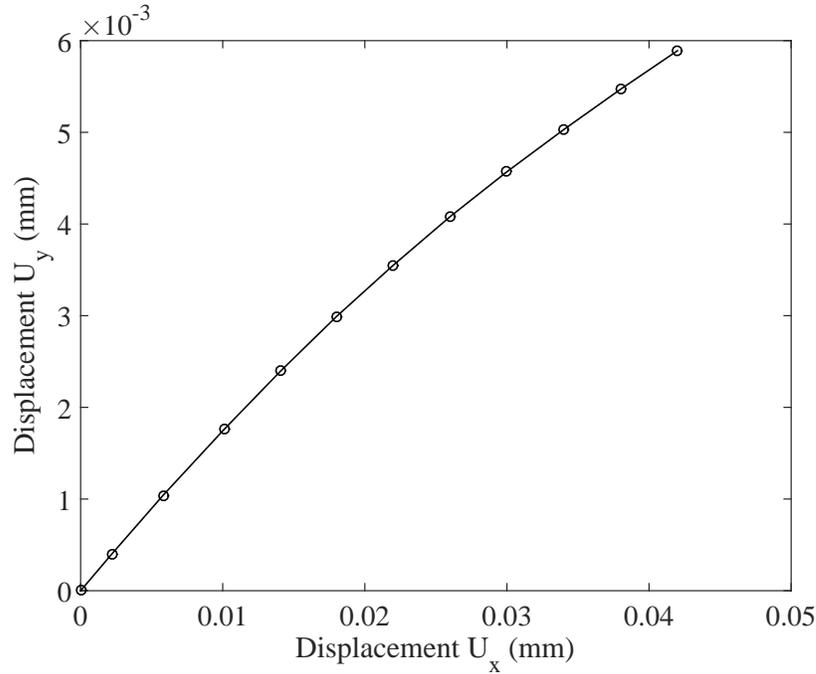
Figure 70: Displacement U_y Vs. Displacement U_x

In Chapter 1, it was noted that air inflated structures are subjected to biaxial states of stress. This biaxial loading typically prevents crimp interchange from occurring in any significant manner due to loading occurring in both yarn directions. Similarly, it is common for the low stiffness region due to decrimping to be much smaller in cases of biaxial loading. From these observations, it is reasonable to expect this unit cell model to capture the important load-deformation characteristics of air-inflated structures.

The mechanical behavior of the unit cell under tensile strain is yarn dominated. However, the mechanical behavior of the unit cell is matrix dominated under shear loading. It is observed in Figure 71 that compared to Figure 69, a larger resultant displacement causes a much lower resultant force. The domination of the matrix in the shear case is also shown in the absense of a significant increase in stiffness usually

136

attributed to the yarn locking. Furthermore, it is likely that the coating shown in Figure C.2 prevents the yarns from rotating to a degree that yarn locking would occur.
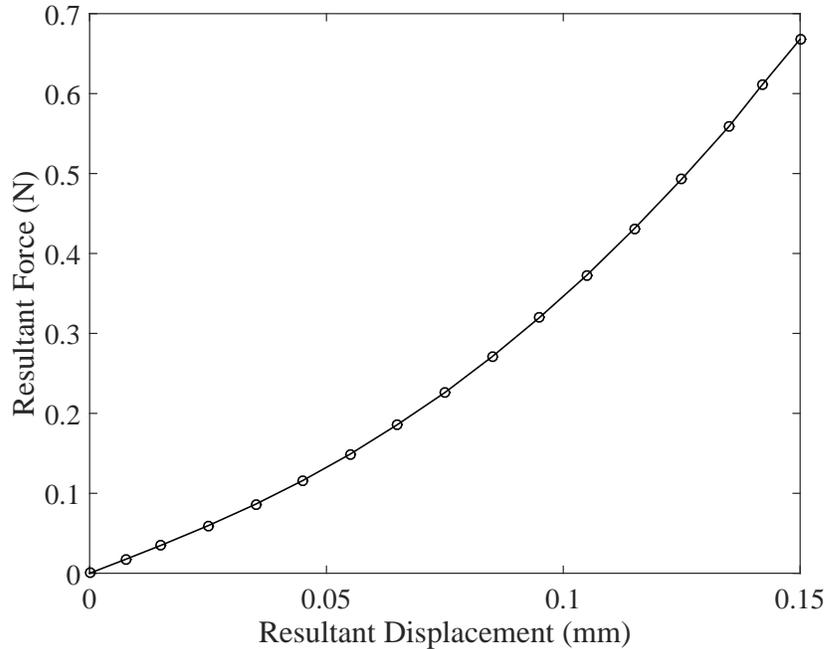
Figure 71: Resultant Force Vs. Resultant Displacement

The results in Table 23 show a comparison between the elastic constants obtained from numerical tests on the unit cell with the experimental results. Using Equations (67) and (68), linear elastic constants are calculated. There is a small difference between the experimental elastic moduli in warp and weft directions. The unit cell elastic moduli are identical resulting from assumptions discussed earlier. Overall, there is good agreement with the experimental and unit cell results. It is likely that better yarn material estimates would increase the agreement between experimental and calculated results. In addition, the nodes between the yarns and matrix interfaces were merged in order to simulate perfect bonding between both volumes. Better agreement between the experimental and calculated results may be achieved by unmerging the nodes and defining contact conditions between the yarns and matrix. This would better simulate the yarn reorientation under loading. The experimental

shear moduli reported are from an inflated cylinder test. This method includes both the strain energy from the fabric and the work done by the air. Thus, experimental results report a higher shear modulus than shown in Table 23. A better comparison is made at the end of this chapter by simulating the inflated cylinder test.

Table 23: Comparison Between the Elastic Constants Obtained from Unit Cell Numerical Tests with Experimental Results

	Experimental	Unit Cell
$E_1(GPa)$	13.68	12.51
$E_2(GPa)$	13.32	12.51
$G_{12}(MPa)$	-	5.96

In the preceding section, effective linear material properties were computed from numerical tests on a unit cell. It may however be desirable to obtain nonlinear material based on the force-displacement results from the numerical testing. The following section presents a process for correlating the nonlinear stress-strain curve applied to a membrane element with the force-displacement results of the unit cell.

4.4   Membrane Element Correlation

In the second approach, the nonlinear mechanical stiffness matrix is iteratively modified and imposed on a membrane element in each increment of the finite element analysis to match the force-displacement curves of the unit cell obtained from numerical tests. The same displacement as the unit cell is prescribed on a membrane element at each increment.

4.4.1   Effective Mechanical Stiffness Matrix

This portion of study employs a four node membrane element with the outer size of the unit cell and the MAT_FABRIC material model in LS-DYNA. In Appendix B, it is noted that *Form* 14 within MAT_FABRIC allows to use of nonlinear stress-strain data in the form of input curves. MAT_FABRIC requires the input of E_a, E_b, ν_{ab},

and G_{ab} as either constants or input curves. The following sections develop a method for the parametrization the input stress-strain curves in such manner that curve can be modified systematically to best match the unit cell and membrane element force-displacement curves.

4.4.2 Parameterization

To optimize LS-DYNA input curves, e.g. stress vs. strain data, one solution is to use splines that interpolate a certain number of given points. The coordinates of the points are defined as parameters. A hermetic cubic spline formulation is used in order to generate continuous load curves for the optimization. Each load curve is divided into 3 segments with a cubic polynomial interpolation for each respective segment as shown in Figure 72.
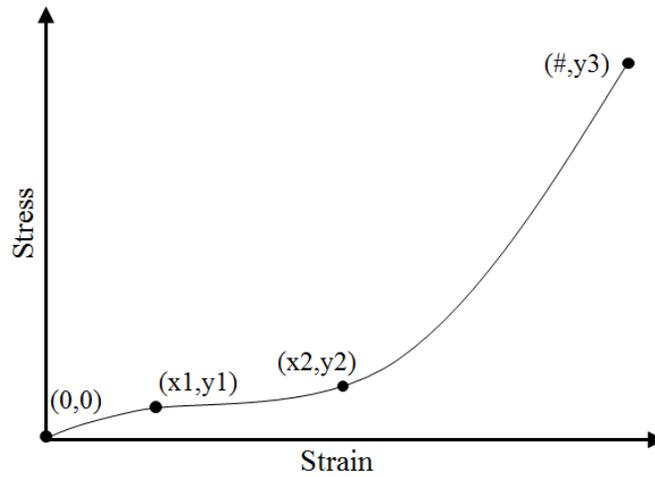

Figure 72: Input Stress-Strain Curve

4.4.2.1 Parametric Cubic Curves

In order to ensure C_1 continuity at two extremities, our functions, shown in Equations (69) and (70) must be of at least degree 3. If the slope of the curve (or the first derivative of the function) is continuous, then the function has 1st order continuity. Consider the following 3rd order equations:

$$x = a_x t^3 + b_x t^2 + c_x t + d_x \tag{69}$$

$$y = a_y t^3 + b_y t^2 + c_y t + d_y \tag{70}$$

By applying the above equations and the first derivatives at two extremities and rearranging into matrix form, the hermite specification is expressed as a matrix equation. The resulting equation is used to solve for the coefficients as shown in Equation (71).

$$
\begin{bmatrix}
a_x & a_y \\
b_x & b_y \\
c_x & c_y \\
d_x & d_y
\end{bmatrix}
=
\begin{bmatrix}
2 & -2 & 1 & 1 \\
-3 & 3 & -2 & -1 \\
0 & 0 & 1 & 0 \\
1 & 0 & 0 & 0
\end{bmatrix}
\begin{bmatrix}
x_1 & y_1 \\
x_2 & y_2 \\
\frac{dx_1}{dt} & \frac{dy_1}{dt} \\
\frac{dx_2}{dt} & \frac{dy_2}{dt}
\end{bmatrix}
\tag{71}
$$

The coefficients can then be substituted back into the original 3rd order parametric equations. In matrix form, with $t \in [0,1]$, the resulting parametric equation is expressed in Equation (72).

$$
\begin{bmatrix} x & y \end{bmatrix}
=
\begin{bmatrix}
2t^3 - 3t^2 + 1 \\
-2t^3 + 3t^2 \\
t^3 - 2t^2 + t \\
t^3 - t^2
\end{bmatrix}
\begin{bmatrix}
x_1 & y_1 \\
x_2 & y_2 \\
\frac{dx_1}{dt} & \frac{dy_1}{dt} \\
\frac{dx_2}{dt} & \frac{dy_2}{dt}
\end{bmatrix}
\tag{72}
$$

From this, four points are needed to define the input stress-strain curve. The first point is constrained to be located at $(0,0)$ so that the model has zero stress at zero strain. The final strain value is also predetermined based on the expected strain range. This range is set by the experimental testing used for validation. This leaves five parameters remaining to alter the shape of the input curve. These parameters are optimized to produce an input stress-strain curve that results in a best match the unit cell and membrane element force-displacement curves.

Utilizing nonlinear input stress-strain curves are not limited to the numerical testing methodology presented in this chapter. The parameter identification process shown in Chapter 2 utilized constant mechanical properties by neglecting the nonlinear crimp interchange region in the stress-strain curve. By redefining the problem to include the above five parameters for each parameter estimated in Chapter 2, nonlinear behavior can me included in the model. However, the entire load-deformation test curve, not just the linear elastic region, must be include in the process.

4.4.3   Objective Function and Constraints

In order to optimize the input curve, an objective function must be defined. Similar to Chapters 2 and 3, the objective function is the mean square error, defined in Equation (18), between the unit cell and membrane element force-displacement curves.

This study adds two constraints to ensure that the supporting points are monotonically increasing and hence the stress-strain curve is monotonically increasing. As shown in Equations (73) and (74), assuming δ is a positive constant, the inequality constraints ensure the supporting points are monotonically increasing.

$$x_2 - x_1 > \delta_x \tag{73}$$

$$y_2 - y_1 > \delta_y \tag{74}$$

4.4.4   Numerical Tests on Membrane Element

The nonlinear input stress-strain curves are iteratively modified and applied to a membrane element in each increment of the finite element analysis to match the force-displacement curves of the unit cell obtained from numerical tests. The same displacement as the unit cell is prescribed on the membrane element.

The tensile elastic moduli E_1 and E_2 are determined by the uniaxial tension test. In the extension tests, the shear strain is theoretically zero, so the value of the shear modulus in this load case is insignificant. A small positive constant is input for the shear modulus of the membrane element to prevent numerical instabilities [51]. Also, from the uniaxial tests, the effective Poissons ratio for the shell element can be obtained. The ratio between the warp direction strain and the weft direction strain at the end of each increment is taken as the Poissons ratio at the strain level in the warp direction. The same procedure can be applied for the Poissons ratio at strain levels in the weft direction. The process is notionally shown in Figure 73.
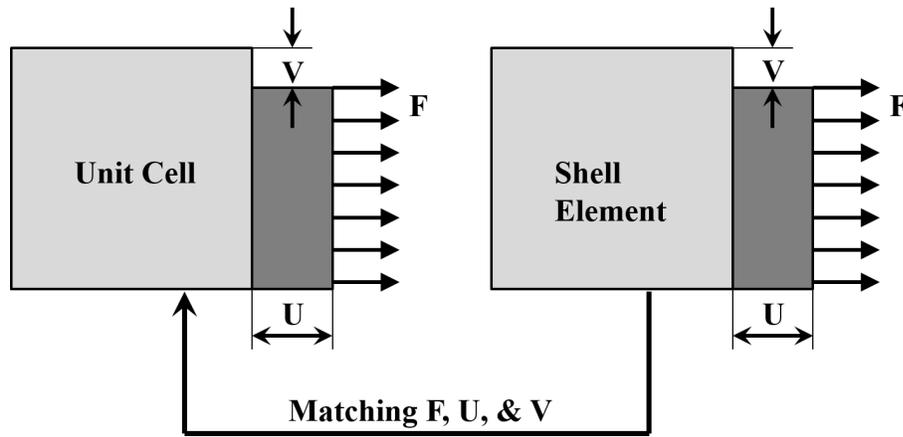
Figure 73: Equivalent Membrane Element in Uniaxial Tension

The effective shear modulus is determined from the trellising test. In the trellising test, the edges of the membrane element will be clamped, but allowed to rotate freely along the corner points. The major strains are expected to be negligible when compared to the shear strain and there is no coupling between shearing and extension in this case, so arbitrary small positive constants is input for the tensile moduli and Poissons ratio for the membrane element [51]. The process is notionally shown in Figure 74.

To demonstrate this process, the shear loading unit cell results shown in Figure 71
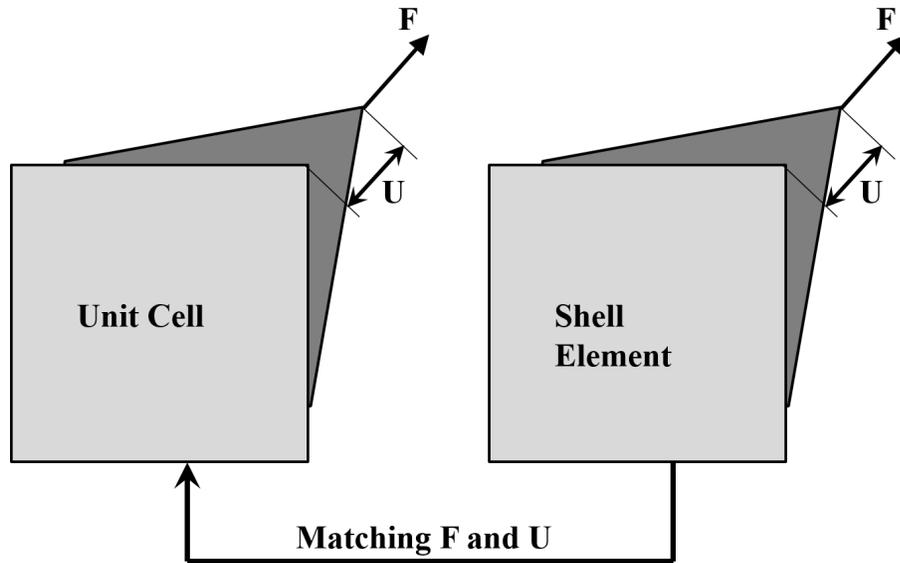
Figure 74: Equivalent Membrane Element in Shear

is used as a test case. The parameter identification methodology developed in Chapter 2 and show in Figure 23 is employed here as well. The only addition to the process is a step in between the sampling of a set of designs to build the response surface and the simulation. This step is the execution of the theory developed in Section 4.4.2.1 to construct the input curve before the simulation begins. To set initial estimates and ranges for the five parameters in the optimization, unit cell and experimental validation data provide guidance. An estimate for the initial value of y_3 is given from the linear shear modulus shown in Table 23. The remaining two points are evenly distributed along the line from the origin and the fourth point. The nominal values are allowed to initially vary by $\pm 20\%$ in the x and y directions. A comparison between the final resulting force-displacement curve from the membrane and that of the unit is shown in Figure 75. There is good agreement between the two data sets. The resulting nonlinear input stress-strain curve is shown in Figure 76.
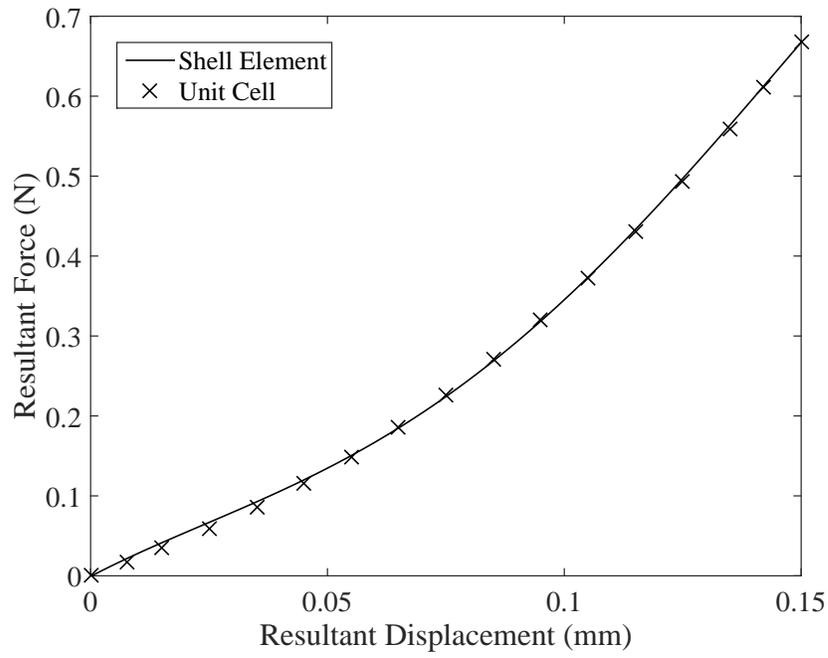
Figure 75: Comparison of Resultant Force in Pure Shear
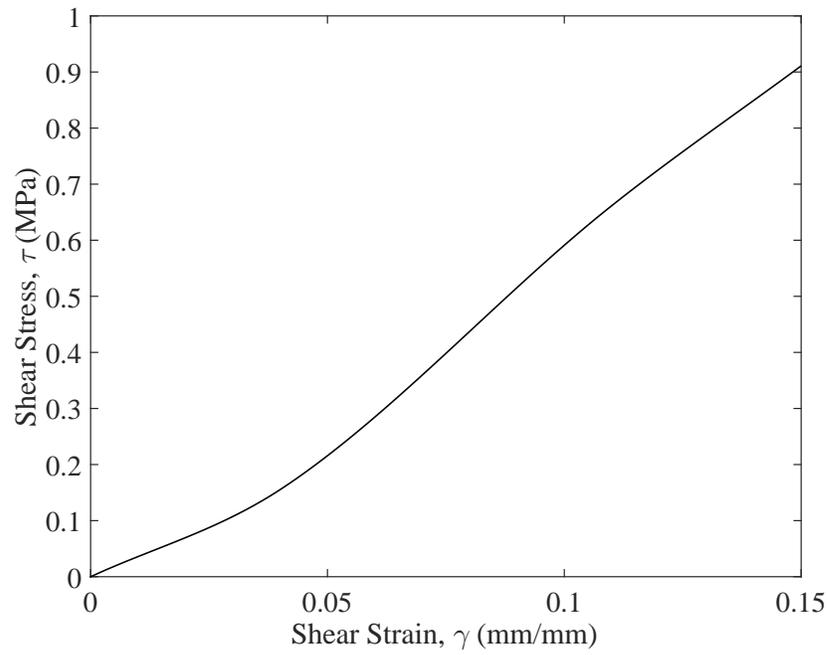
Figure 76: Equivalent Shear Stress and Strain for the Membrane Element

4.5 Validation

In this study, an experimental data set from the inflated cylinder torsion test method to characterize the shear stress-strain behavior of textile materials is used to validate the above methodology for air-inflated structures. In the inflated cylinder torsion test, torque versus twist angle is measured for an inflated cylinder where one end cap has a free rotational degree of freedom and the other end cap has a free axial degree of freedom. Using the well known relations from engineering mechanics discussed in Section 2.2.4.3, the applied torque can be converted to the resulting shear stress and the twist angle to shear strain.
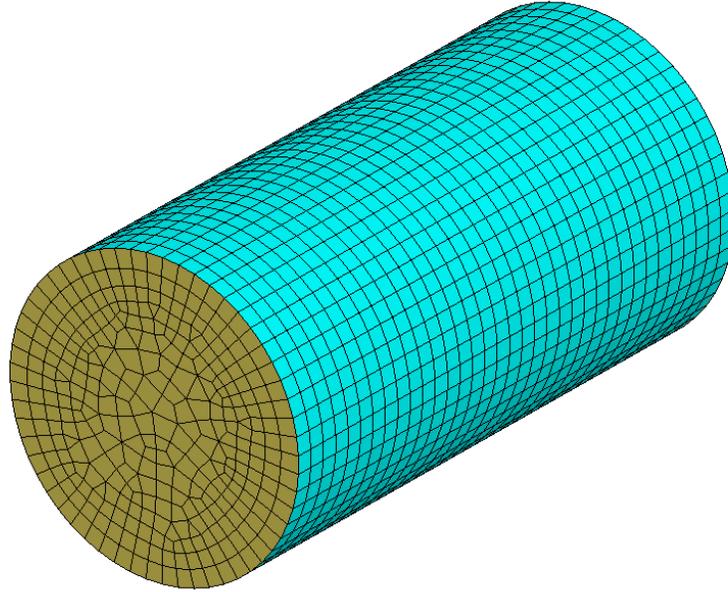
Figure 77: Inflated Cylinder Finite Element Model

A finite element analysis was completed in LS-DYNA using the MAT_FABRIC material model. The inflated cylinder model has a radius of 98.6 mm, a length of 392 mm, and thickness of 0.3715 mm. The model is meshed with 2732 nodes and 2628 membrane elements; of which 1960 membrane elements were dedicated to the fabric portion of the model and the remained elements were used on the end caps. Linear elastic moduli from Table 23 were used for E_a and E_b, the Poisson's ratio was

145

assumed to be low, and the non-linear shear modulus was that shown in Figure 76. The end caps were modeled as steel with isotropic material properties.

The nodes at one end cap were constrained to have only a free rotational degree of freedom about the longitudinal axis. This end cap had a prescribed rotation $(20°)$ applied consistent with that in the experimental testing. The opposite end cap was constrained to have only a free axial degree of freedom. Inflation pressure is applied using a simple airbag model to capture the effects of air compressibility on the structures stiffness. The inflation pressures were tested at $4\ psi$, $7\ psi$, and $10\ psi$. The model was allow to inflate to the prescribed inflation pressure and then the prescribed rotation was applied. After the model reached a steady state, the resulting torque was measured at the nodes that were constrained from rotating about the longitudinal axis.
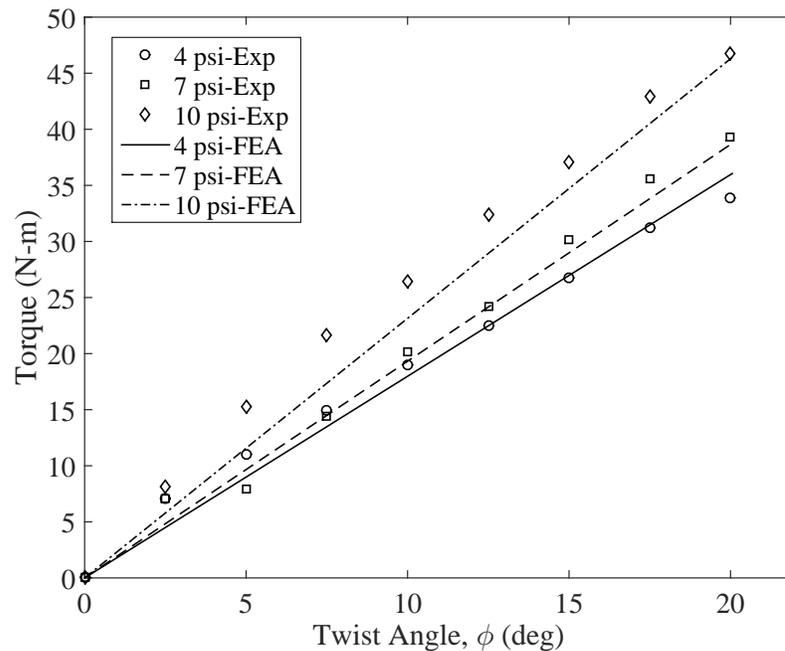
Figure 78: Applied Torque versus Twist Angle Comparison between Model and Data Cylinder of Urethane Coated Kevlar® at Three Inflation Pressures

Figure 78 provides a comparison between the experimental data and simulation results. The plot shows only a the final torque-rotation values from the simulation,

with a line connecting them to the origin. This should not imply that the simulation results were linear. The torque-rotation values are compared because the important trends do not require the conversion to stress-strain.

The simulation results trend well with the experimental data. As the pressure increases the stiffness in the model increases. This is consistent with previous analysis and testing [43, 35, 27]. While the stiffness of the inflated cylinder increases with increasing pressure, the same material shear modulus was used for all three models. This distinction is important because estimating shear modulus from the inflated cylinder test method and applying it to model of an air-inflated structure as shown above will likely result in an overly stiff structure.

Tanner found evidence in the inflatable tension cone models that an unrealistically low shear modulus value was needed to recover displacements that correspond to test data. This could be explained by the utilization of shear moduli calculated from the inflated cylinder test. The *unrealistic* estimate of shear modulus of 371 *psi*, used for the tension cone model, is much closer the values shown in Figure 76 and Table 23 than the value of 7417 *psi* obtained from the inflated cylinder test [15].

To illustrate this, Figure 79 shows the change in the predicted tension cone torus pitch angle from $0°$ to $9°$ AoA as a function of shear and elastic moduli originally shown in Reference [15]. The range of elastic moduli used in this orthotropic sensitivity analysis were based on varying the elastic moduli by $\pm 30\%$ around the nominal value. The range of shear moduli is progressively decreased by a factor of 20 from the isotropic value. It was initially thought that non-physical material properties may be necessary for the MAT_FABRIC model in LS-DYNA in order to recover more realistic magnitudes of deformation; however the unit cell estimate of shear modulus equal to 864 *psi*, which was estimated from physical dimensions and material properties, compares well with experimentally observed torus rotation of $1.89°$. Tanner found that an elastic modulus of 501,417 psi and shear modulus of 371 psi resulted in a
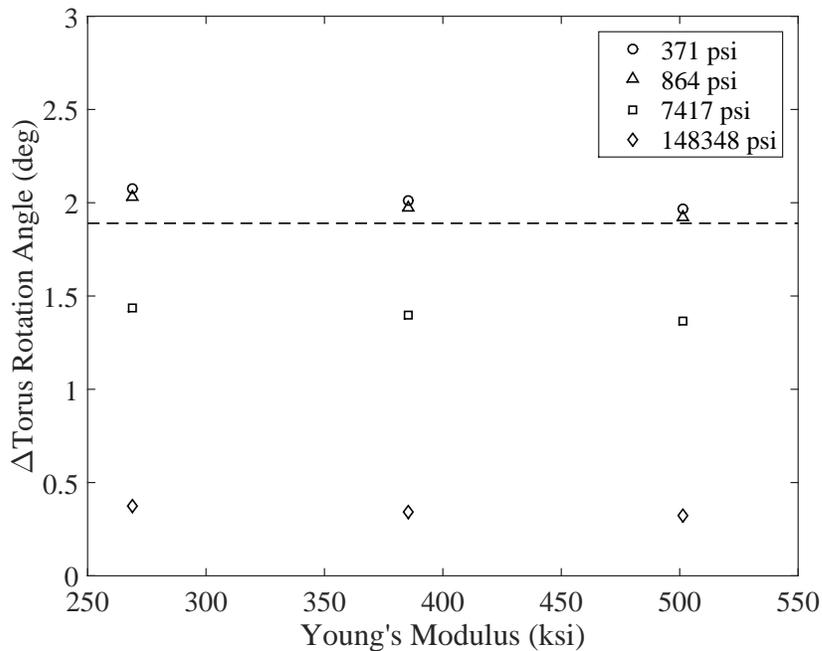
Figure 79: Comparison Between Change in Tension Cone Torus Angle for Various Shear and Elastic Moduli. Dashed Line Corresponds to Experimentally Observed Torus Rotation of 1.89°

1.96° change in torus rotation, which is within 4% of the experimentally observed rotation of 1.89°. The unit cell estimate of shear modulus equal to 864 *psi* resulted in a change in torus rotation within 2% of the experimentally observed rotation.

4.6 Summary

A novel methodology is presented in this chapter for predicting the effective nonlinear elastic moduli of fabrics using a combination of the homogenization method and finite element analysis. The methodology is shown on a Urethane Coated Plain Woven 400 Denier Kevlar® 49 Fabric. The general process is summarized as:

Step 1. Obtain or estimate geometric and material properties for the yarn.

Step 2. Build a unit cell for the fabric.

Step 3. Characterize the material behavior of force versus displacement by numerical trellising and extension tests on the unit cell using finite element analysis.

148

Step 4. Obtain equivalent elastic constants for membrane elements by correlating the force vs. displacement curves of the unit cell and a membrane element with the same outer dimensions.

A unit cell finite element model was constructed from fabric measurements taken using an high magnification microscope. Multiple mesh types were considered for the unit cell finite element model, including 4-node tetrahedral elements, 8-node hexahedral elements. A voxel based mesh was chosen using 8-node hexahedral elements in order to provide a balance in computational efficiency and accuracy. Periodic boundary conditions are applied to replicate the repeating nature of the fabric. Numerical tests such as uniaxial and trellising are conducted on the unit cell for the determination of the effective material properties for a membrane element. A transversely anisotropic material model is utilized for the yarns, while an isotropic material model is utilized for the matrix (coating). Nonlinear input stress-strain curves are iteratively modified and applied to a membrane element in each increment of the finite element analysis to match the force-displacement curves of the unit cell obtained from numerical tests. Comparison with experimental inflated cylinder results validates the effectiveness of this procedure. The methodology can be extended to other textile architectures by constructing the corresponding unit cell.

CHAPTER V

SUMMARY AND FUTURE WORK

5.1   *Summary*

This thesis proposes the development of a multi-scale flexible material modeling approach that enables efficient high-fidelity IAD design and a critical understanding of the new materials required for robust and cost effective qualification methods. The approach combines understanding of the fabric architecture, analytical modeling, numerical simulations, and experimental data. The work herein was performed to reach this goal.

Chapter 1 discusses the motivation and provided a background for the topics presented in this work. The development history of three IAD configurations is presented. Air-inflated structures in general are discussed in the context of fabric architectures and construction methods to provide insight into important mechanical properties. A comparison of experimental textile mechanical property determination methods is provided to highlight advantages and disadvantages of each method. Finally, three past approaches are provided to simulate the macroscopic behavior of woven fabrics.

Chapter 2 applies the parameter identification methodology to a set of bias-extension and uniaxial tension experimental test data. The parameter identification methodology is introduced. Mean Square Error is defined as the objective function to be minimized in the methodology. The nominal predictions are compared to the data through a direct analysis to identify where the model is fundamentally different than the experimental data. The nominal analysis describes the geometric and material models used in the finite element simulation as well as the specified loading and boundary conditions. A convergence study shows that the mesh size is set based on

a balance between accuracy and computational expense. Based on the information provided in the previous steps, an inverse analysis is performed to obtain an accurate match between the model predictions and the data through estimation of input parameters. Poisson's ratio was shown to be an insignificant contribution to the objective function. A high degree of correlation was shown between the three remaining parameters and the simulation of the test used to obtain them experimentally. The resulting estimate of shear modulus compares well with the experimental data from the trellis-frame test.

Chapter 3 applies the parameter identification methodology to a mesomechanical material model using a set of experimental test data. The mesomechanical model is developed through a detailed presentation of homogenization method and yarn reorientation algorithm. The homogenization process is studied to gain insights into effective material property sensitivity to changes in input parameters. The model shows effective material properties that vary with undulation and and initial braid angle. In addition, the discount factor is shown to have a significant impact on model behavior. In the sensitivity analysis, the contribution of each variable to the variance of the response is calculated. Based on the information provided in the previous steps, an inverse analysis is performed to obtain an accurate match between the model predictions and the data through estimation of input parameters. The inverse analysis was performed for many different parameter subsets to illustrate the advantage of the methodology as compared to the traditional direct approach. Results show a significant improvement in the matching between the model predictions and the data.

Chapter 4 presents a novel methodology for predicting the effective nonlinear elastic moduli of fabrics using a combination of the homogenization method and finite element analysis. The general process is summarized as:

Step 1. Obtain or estimate geometric and material properties for the yarn.

Step 2. Build a unit cell for the fabric.

Step 3. Characterize the material behavior of force versus displacement by numerical trellising and extension tests on the unit cell using finite element analysis.

Step 4. Obtain equivalent elastic constants for membrane elements by correlating the force vs. displacement curves of the unit cell and a membrane element with the same outer dimensions.

A unit cell finite element model was constructed from fabric measurements taken using an high magnification microscope. Multiple mesh types were considered for the unit cell finite element model, including 4-node tetrahedral elements, 8-node hexahedral elements. Periodic boundary conditions are applied to replicate the repeating nature of the fabric. Numerical tests such as uniaxial and trellising are conducted on the unit cell for the determination of the effective material properties for a membrane element. A transversely anisotropic material model is utilized for the yarns, while an isotropic material model is utilized for the matrix (coating). Nonlinear input stress-strain curves are iteratively modified and applied to a membrane element in each increment of the finite element analysis to match the force-displacement curves of the unit cell obtained from numerical tests. Comparison with experimental inflated cylinder results validates the effectiveness of this procedure. The methodology can be extended to other textile architectures by constructing the corresponding unit cell.

The next section provides recommendations for future efforts to advance the state of mechanical property determination research as it pertains to air-inflated structures. The modeling of fabric structures would benefit from the publication of additional macro and meso level material data. A discussion of possible augmentations to the parameter identification methodology is also presented.

5.2 Suggestions for Future Work

The higher fidelity material models presented in this work require information not typically tested for in standard mechanical tests regarding fibers and yarns used to construct the fabrics. A limitation encountered in this work was the lack of experimental test available for the individual yarns. Currently, modeling efforts rely only on macromechanical information for a particular fabric with minimal information regarding the constituent materials. The modeling of air-inflated fabric structures would benefit from publication of additional macromechanical properties and the mesomechanical properties of candidate materials. By performing uniaxial tension tests on the fabric yarns, more accurate data can be obtained for the longitudinal elastic modulus. Even with this, however, the other yarn material properties are more difficult to obtain experimentally. To overcome this, researchers have employed a homogenization method that relies on fiber material properties as well as estimates of fiber volume fraction [51]. The material properties for the yarn fibers is more consistent and easier to find in literature. Estimates of fiber volume fraction can be made using methods like optical microscopy as discussed in Appendix C.

IADs typically operate at lower strain levels far away from the failure load of the material. Furthermore, the IAD may operate on both the load or unload portion of the stress-strain curve. The analysis presented in this work focused on the single load cycles characteristic of air-inflated fabric structures. The raw experimental data from Chapters 2 and 3 exhibited appreciable hysteresis, as well as, a wandering or strain set between cycles. For future efforts, it may be necessary to model the hysteretic behavior in uniaxial loading and unloading of structural components. Hysteretic curves (curves with more than one possible y value for some of the x values) cannot be quantified using the ordinate-based curive matching approach introduced in Chapter 2 due to the non-uniqueness of the ordinate values of the computed curve with respect to the target curve. A logical approach for comparison of the two curves is to map

one of the curves onto the other. The questions of how to scale the curves and how to match two curves of unequal length immediately arise. Scaling can be particularly important since scale changes have an effect on the distances between the two curves. In many cases, such as stress vs. strain, there may be several orders of magnitude difference between the values on the abscissa and ordinate. The experimental data in Reference [25] provides a source of validation data for this effort. For a more detailed discussing on the use of curve mapping for parameter identification, refer to the work of Witowski and Stander [79]. The mesomechanical model presented in Chapter 3 also has the potential to capture hysteretic behavior through the yarn reorientation, but load and unload simulations will be required to determine which parameters have the largest impact on this phenomenon.

The numerical testing methodology presented herein has the advantage of being applicable to virtually any composite type under any load condition. Further development of this methodology should explore higher strain levels as well as various states of stress and braid angles. In the case of shear loading, simulations at higher strain levels would investigate a model's ability to capture the locking behavior discussed in Chapter 1. This investigation was limited to looking at pure tension and pure shear loading cases. Biaxial loading cases at multiple states of stress will be necessary for design space explorations. This effort would also benefit from the publication of biaxial experimental data to validate against. The available test data also limited this work to plain woven fabrics. Validating the methodology for other fabric architectures such as biaxial and triaxial braided fabrics would show broad applicability to air-inflated structures. The unit cell mesh utilized in this work was appropriate for fabric architecture and strain levels being modeled. When attempting to model signification yarn reorientation, the ability of a model to capture this behavior is important. The 8-node hexahedral volume mesh (that follows the yarn surface) may

154

prove to be necessary over the voxel based mesh in this case. Furthermore, the perfect bonding assumption between the matrix and yarns should be challenged in cases of little or no coating. Unmerging the nodes between the yarns and matrix, as well as, adding contact conditions between adjacent materials could capture more of the physics related to yarn reorientation.

Although the experimental test methods discussed in this work are representative of loads experienced by air-inflated structures, larger scale test articles address particular structural and integration issues related to flight IAD systems that can not be captured in sub-scale tests. As discussed in Chapter 1, Brayley tested the bending response of inflatable, braided beams and arches with external reinforcing straps [35]. The work focused on experimentally determining the constitutive properties of the constituent materials, and quantifying the load-displacement behavior of beams and arches with full scale laboratory tests. By matching the load-displacement data from the 4-point bend tests using the parameter identification methodology employed in Chapter 2, estimates for the material properties can be compared to those obtained from typical sub-scale tests. This would allow for modeling assumptions and scale effects to be quantified. As an example, the membrane assumption could be investigated for the tension cone shown in Figure 1 where deformation in the tension shell indicates bending may be important at that scale. Additionally, the inflatable, braided beam with external reinforcing straps shown in Figure 7 contains multiple components and materials that may impact the overall constitutive behavior of the structure.

APPENDIX A

STRUCTURAL OPTIMIZATION USING LS-OPT

A.1   Introduction

The material identification process is a non-linear optimization process that uses experimentally measured data to determine the parameters describing a material model. A non-linear simulation is performed with the model parameters as inputs and the deviation of the simulated performance from that measured is used as a criterion for minimization [88].

In using LS-OPT, the successive response surface method is used, which exploits a domain reduction scheme in order to converge to an optimum. Commonly, the construction of the response surface used a design of experiments approach in combination with a D-optimal experimental design. The following is a presentation of some of the basics in LS-OPT.

A.2   Optimization Algorithm

A.2.1   Problem Setup

The following introduction into optimization basics is necessary for the sake of completeness [65]. Vanderplaats describes the objective of engineering optimization as striving to produce the "best quality of life possible with the resources available [89]." Expressed mathematically in Equations (75) and (76), the above phrase is as follows:

$$\min\ f(\bar{x}) \tag{75}$$

subject to

$$g_j(\bar{x}) \leq 0 \ , \ j = 1, 2, \ldots, m \tag{76}$$

where f and g are functions of independent design variables $x_1, x_2, \ldots, x_n$. The function f is called the objective function and identifies the quantity to be minimized (or maximized). The design restriction in the form of inequality constraint functions g must be considered. The value m specifies the number of inequality constraints of the problem. It should be noted that equality constraints may exist, but can be algebraically represented by two inequality constraints with identical upper and lower bounds. Thus, the equality constraints are removed from this formulation. The independent design variables or design parameters are collectively described in Equation (77) by the vector $\bar{x}$, which is bounded by lower $(\bar{x}_L)$ and upper $(\bar{x}_U)$ bounds such that

$$\bar{x}_L \leq \bar{x} \leq \bar{x}_U \tag{77}$$

The numerical solution of constrained optimization problems can be transformed into pseudo-unconstrained problems by introducing the Lagrange function. The constraint function is added to the objective function with the help of the Lagrange multiplier vector, λ as shown in Equation (78).

$$L(\bar{x}, \lambda) = f(\bar{x}) + \lambda^T g(\bar{x}) \tag{78}$$

The optimization problem has been mathematically transferred into the determination of a saddle point on the Lagrange function (stationary problem). In order to properly determine the saddle point the partial derivatives of the Lagrange function with respect to the optimization variables are necessary. Through the use of the Kuhn-Tucker necessary conditions, an individual design point can be assessed for optimality. These conditions are discussed in more detail in Vanderplaats [89].

Solving the optimization problem requires an optimization algorithm. Gradient-based methods, like the Sequential Quadratic Programming (SQP) method, are often used and require the determination of first order derivatives of the objective and constraint functions with respect to the design variables. In order to guarantee convergence of the gradient-based methods, the functions as well as their 1st derivatives must be continuous. The gradients can be either computed analytically or numerically. Unfortunately, analytical gradients are generally difficult or impossible to obtain due to high nonlinearity of the problem being solved. Numerical gradients on the other hand, obtained from finite differences, can be spurious and not suitable for gradient-based optimization. From this, selecting the correct size for the finite differences can be problematic: too small and spurious gradients may occur, too large and a loss of accuracy occurs. It is often advised that gradient-based methods be used for linear structural analysis and certain simulations [65]. Unfortunately, most IAD simulations do not meet these criteria.

In order to overcome the problems mentioned above and to obtain a smooth design response, researchers have focused on approximation methods [90]. Two popular approximation methods are the Response Surface Methodology (RSM) and Neural Networks [91, 92]. In the following, an introduction into the methodology of RSM is presented.

A.2.2 Metamodel-Based Optimization

Stander and Craig note that the Response Surface Methodology (RSM) has its origin in the statistics and physical experimentation and has been the primary gradient-free simulation based approach available [93, 94, 95]. Instead of utilizing local information like gradients, RSM selects experimental design points that are optimally distributed within the design space. Utilizing those experimental design points, approximative surfaces are constructed. Rather than finding the optimum of the exact functions,

the approximative surfaces are used. Because only a few experimental design points are used to construct the approximation, this approach is relatively rapid and also suited for applications in which experimental data is used directly.

The first step in the RSM is the definition of the form for the approximate functions. LS-OPT allows for linear, elliptical (linear and diagonal terms), interaction (linear and off-diagonal terms) as well as quadratic functions for the approximation. The exact mathematical expression is then approximated as is shown in Equation (79)

$$y = \eta(\bar{x}) \approx f(\bar{x}) = \sum_{i=1}^{L} a_i \phi_i(\bar{x}) \qquad (79)$$

where ϕ_i are the basis functions that are dependent on the design variables $\bar{x}$ and weighting parameters a_i to be determined. L is the number of basis functions that are used to approximate the model. As examples, a linear approximation is shown in Equation (80) and quadratic approximation is shown in Equation (81).

$$1, x_1, x_2, \ldots, x_n \qquad (80)$$

$$1, x_1, x_2, \ldots, x_n, x_1^2, x_1 x_2, \ldots, x_1 x_n, \ldots, x_n^2 \qquad (81)$$

The generally accepted practice is to select the basis functions such that the approximation surface is accurate enough to achieve fast convergence, but simple enough to be used in numerous repeating calculations. Higher order basis functions are more accurate than lower order functions. It would be advantageous to select the functions on the basis of some knowledge about the true behavior of the structure which is seldom known [96, 97].

A.2.2.1 D-Optimal Designs

A specific number, P, of experimental design points are needed, depending on the order of approximation, for the second step of constructing the approximation. To

account for noisy responses, it is common to use a 50% oversampling in the experimental design points [98]. The actual number of experimental design points, P, also influences the accuracy. Generally, the prediction accuracy of the response surface improves as the number of points is increased; however, the computational cost increases as well. The design points in the actual region of interest are chosen using a factorial design that uses the D-optimality criterion [94]. An advantage in using the D-optimality criterion is that it can be applied to irregularly shaped design regions and any number of experimental design points can be considered [65]. The D-optimality criterion states that the best set of design points selected from a basis design is to maximize the determinant of $\underline{\underline{X}}^T\underline{\underline{X}}$, which is a measure for the accuracy of the approximation [99, 96].

As shown in in Equation (82), the unknown parameters, a_i in Equation (79) are determined on the basis of a least squares fit of the error, $E(\bar{a})$ between exact values $y(\bar{x}_p)$ and approximations $f(\bar{x}_p)$ at the selected experimental design points.

$$E(\bar{a}) = \sum_{p=1}^{P} \left[y(\bar{x}_p) - f(\bar{x}_p) \right]^2 = \sum_{p=1}^{P} \left[y(\bar{x}_p) - \sum_{i=1}^{L} a_i \phi_i(\bar{x}) \right]^2 \to \min \qquad (82)$$

The solution for the unknown coefficients is as shown in Equations (83) and (84).

$$\bar{a} = (\underline{\underline{X}}^T\underline{\underline{X}})^{-1}\underline{\underline{X}}^T\bar{y} \qquad (83)$$

where the matrix $\underline{\underline{X}}$ is:

$$\underline{\underline{X}} = \left[X_{pi} \right] = \left[\phi_i(\bar{x}) \right] = \begin{bmatrix} \phi_1(\bar{x}_1) & \cdots & \phi_i(\bar{x}_1) \\ \vdots & \ddots & \vdots \\ \phi_1(\bar{x}_p) & \cdots & \phi_i(\bar{x}_p) \end{bmatrix} \qquad (84)$$

The final step is concerned with the prediction of optimized values for each design variable. This prediction is made on the basis of the response surface just now

determined. LS-OPT automatically creates the next set of simulations (experimental designs) using these optimized design variables.

A.2.2.2 Sequential Response Surface Method

The current work exploits the successive RSM option in LS-OPT in order to accelerate convergence. As a result, the region of interest is neither constant in size nor is it fixed in space allowing for a convergence of the solution to a prescribed tolerance. Contraction and panning parameters control the successive adaptation of the subregion [65]. Those parameters are dependent on the previous optimum design and they are designed to reduce oscillation and prevent premature convergence [95, 100]. Figure A.1 highlights three possible cases for the adaptation of the region of interest: (a) pure panning, (b) pure zooming, (c) a combination of both.
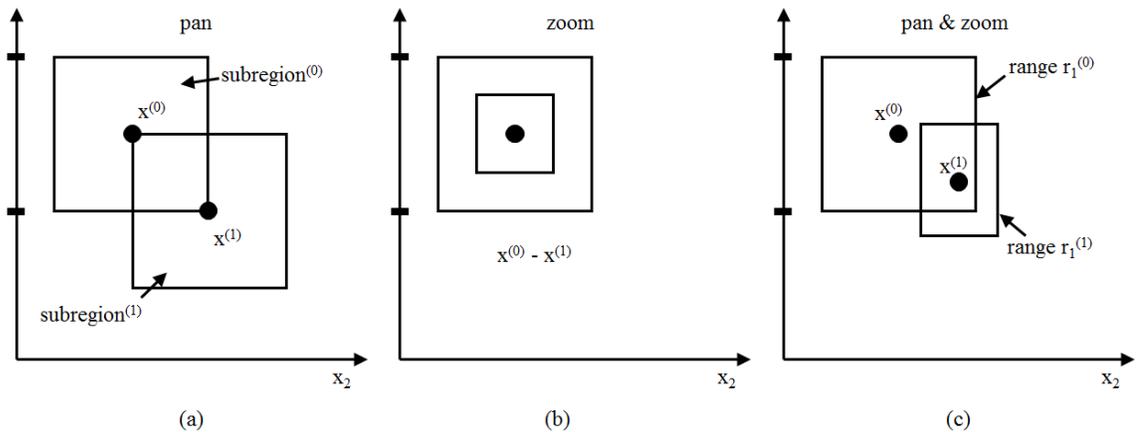
Figure A.1: Adaption of subregion: (a) pure panning, (b) pure zooming, (c) a combination of both

An adaptive domain reduction strategy is used to reduce the size of the subregion in order to accelerate convergence. During a particular iteration, new points are located in a subregion of the design space. This, however, is typically only used for an optimization process where the user is interested in the final optimum point rather than a global exploration of the design space. Thus, using a sequential domain reduction strategy is often used in parameter identification. SRSM allows the building

of a new response surface (typically linear polynomial) in each iteration. The size of the subregion is adjusted for each iteration and points belonging to the previous iteration are ignored. To automate the successive sub-domain reduction scheme for SRSM, the size of the region of interest (as defined by the range of each variable) is adapted based on the accuracy of the previous optimum as well as the occurrence of oscillation.

A variable subregion (trust region) has already been used in previous works [101, 102, 103]. Stander and Roux et al. provide a detailed description of SRSM [98].

APPENDIX B

MATERIAL PROPERTY DETERMINATION

A silicone coated 200 denier Kevlar® material underwent a series of pseudo-static test to determine its mechanical properties, the results of which are provided in Lin et al. [25]. Selected samples are included in this appendix as well. The tests were performed by researchers at ILC Dover. The MAT_FABRIC material model is used throughout this work and a short description is provided in Section 2.3.2. This appendix explains how the experimental test data were interpreted and reduced to arrive at an appropriate set of material properties for use in the nominal analyses.

B.1   Experimental Data

The purpose of this appendix is to outline the steps taken to post process the experimental load-deformation data obtained from the uniaxial tension and trellis-frame tests into an appropriate format for the MAT_FABRIC model with linear elastic material properties.

B.1.1   Uniaxial Tension Test

The uniaxial tension tests in the 200 denier Kevlar® warp and weft directions measure load-deformation for the load interval [0,2500 N]. Five samples were tested in each direction, with each sample undergoing ten load cycles. Figure B.1 shows the complete load history for one sample (sample B) in both the warp and weft directions. Both hysteresis and strain set are observed in the warp and weft directions. The loading in the weft direction shows a longer period of lower stiffness. This is most likely attributed to an increase in crimp in the weft direction.

Subjecting the samples to repeated load-deformation cycles serves multiple purposes. In addition to observing the hysteresis and strain set in the fabric samples, the multiple cycles serve as means of removing kinks and crimp that occur from manufacturing and processing. It can be seen in Figure B.1 that after the first cycle, the remaining cycles still contain a small amount of hysteresis but the drift in strain has effectively stopped. The last cycle, as shown in Figure B.2, is used to proceed with the post-processing.
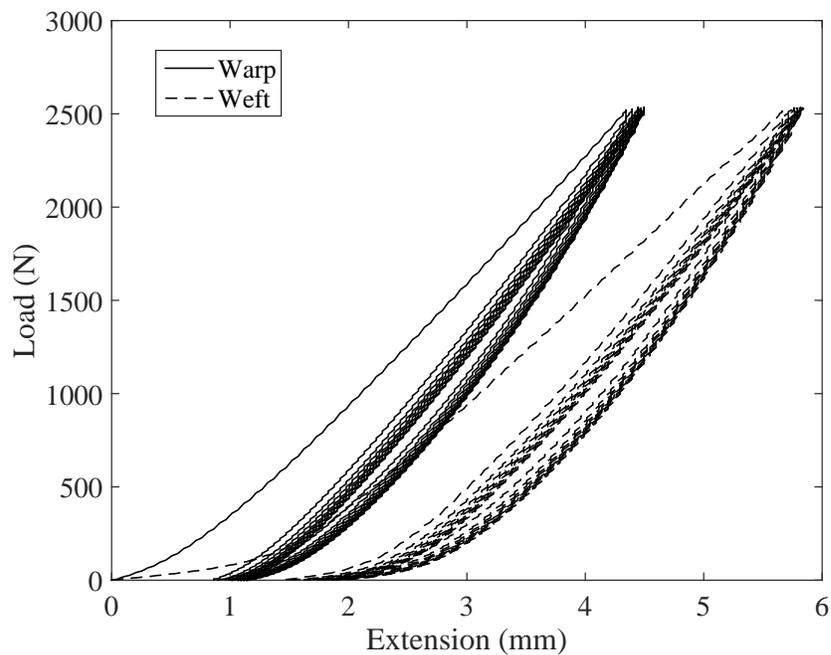
Figure B.1: 200 Denier Kevlar® Warp and Weft Uniaxial Tension Test - All Ten Cycles

B.1.2 Trellis Frame Test

A similar procedure for post-processing is followed for the trellis-frame test. One of the objectives in Chapter 2 is to show that shear modulus can be obtained from the bias-extension test, which is simpler and less expensive to carry out when compared to the trellis-frame test. The data from the trellis-frame will be compared to data from the bias-extension tests for validation purposes. Five samples were subjected to
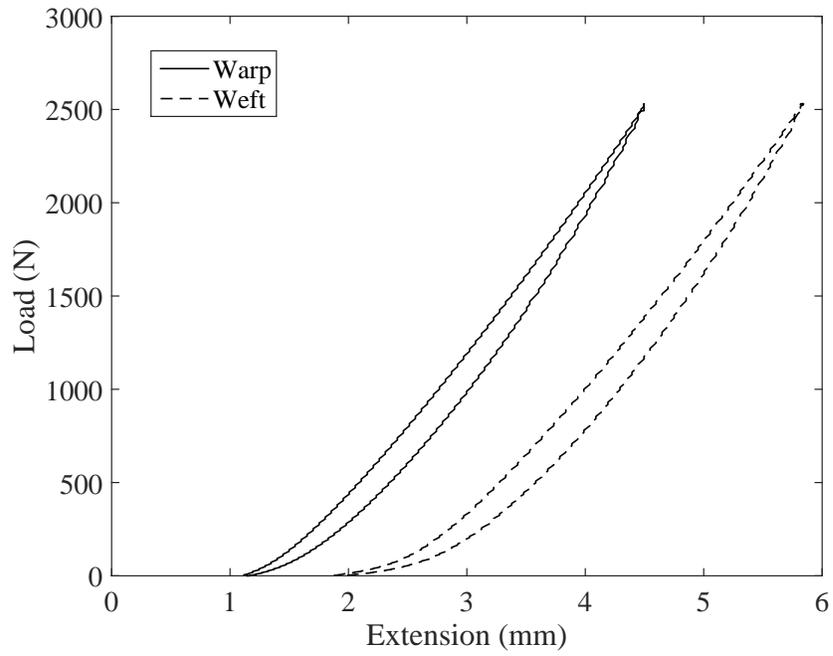
Figure B.2: 200 Denier Kevlar® Warp and Weft Uniaxial Tension Test - Last Cycle

pure shear loading over five cycles. The last cycle from one of the samples (sample D) is selected. Figure B.3 shows hysteresis in both tension and compression. It should be noted that little to no drift was observed in the strain response over multiple cycles.
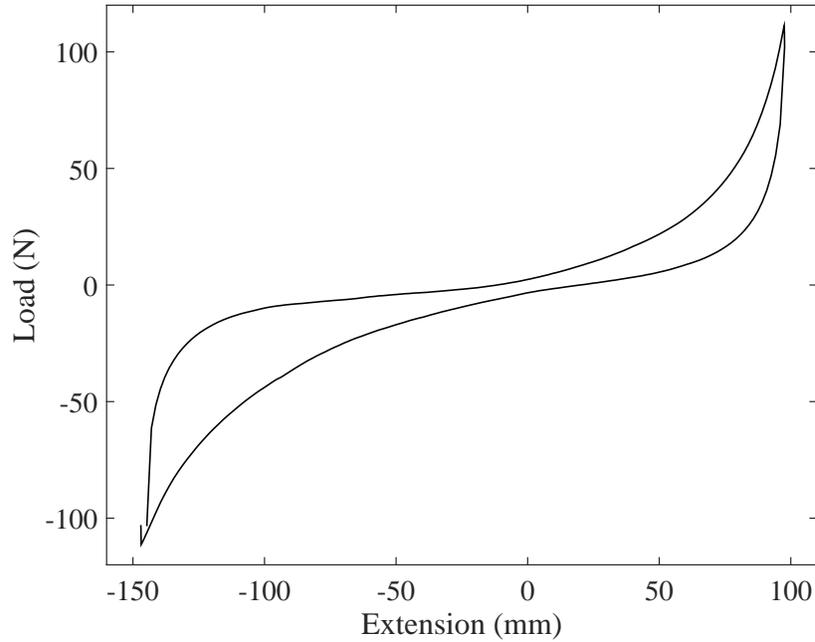
Figure B.3: 200 Denier Kevlar® Trellis Frame

B.2 Determination of Orthotropic Material Properties

The following properties are required for an orthotropic material definition: linear elastic modulus in both fiber directions, E_a and E_b and Poisson's ratios in both fiber directions ν_{ab} and ν_{ba}. MAT_FABRIC allows the input of E_a, E_b, and ν_{ab} and uses Hooke's Law, as shown in Equation (85) to calculate the remaining value. In addition, the model requires the input of a linear shear modulus, G_{ab}. The a and b fiber directions correspond to the warp and weft fiber directions.

$$\frac{\nu_{ab}}{E_a} = \frac{\nu_{ba}}{E_b} \tag{85}$$

The material model allows fiber directions to be defined relative to the material coordinate system in the 3 or 4 node shell element. The material coordinate system is defined by specifying an angle, β, relative to the local element coordinate system. In LS-DYNA, the term local refers to the shell element coordinate system. This system is determined from element connectivity, not some coordinate system defined

in the input deck. The node 1 to node 2 vector (n_1-n_2) is the local x-direction, the local z-direction is the normal to the shell (cross product of n_1-n_2 and n_1-n_4) and the local y-direction is the cross product of z and x. While the fiber orientations can be arbitrary for an orthotropic analysis in LS-DYNA, all of the analyses in this work assume the fibers to be orthogonal.

There exists several membrane element formulations within MAT_FABRIC that alter the stress-strain calculations within LS-DYNA. While rigorous mathematical derivations of these formulations are unavailable due to the nature of the commercial code, the LS-DYNA Keyword and Material Model user manuals provides some reference [66]. The least computationally intensive and default formulation is $form$ 0. This formulation assumes orthogonal fiber directions and is based on engineering stress and strain. The most expensive formulation is $form$ 14 which is not limited to small strain assumptions and is formulated in terms of Green strain and the 2nd Piola-Kirchhoff (PKII) stress. The addition of quadratic terms gives the Green strain tensor its rotation independence. $Form$ 14 allows to use of nonlinear stress-strain data, but calls on a linear elastic moduli if nonlinear data is not present. Recent updates have allowed the input of nonlinear data at negative values of strain. This is available in order to model the compressive stresses resulting from tight folding of an airbag for example. Non-orthogonal fiber directions are allowed for $form$ 14, so fiber directions must be specified in the input deck.

B.2.1 Uniaxial Tension Test Data - Sample B

The load-extension data from the warp and weft directions is shifted to remove the strain set in the data and allow the curves to originate at (0,0) as shown in Figure B.4.

It should be noted that nonlinear stress-strain data used in $form$14 have to be converted from Cauchy stress and stress values typically obtained from mechanical
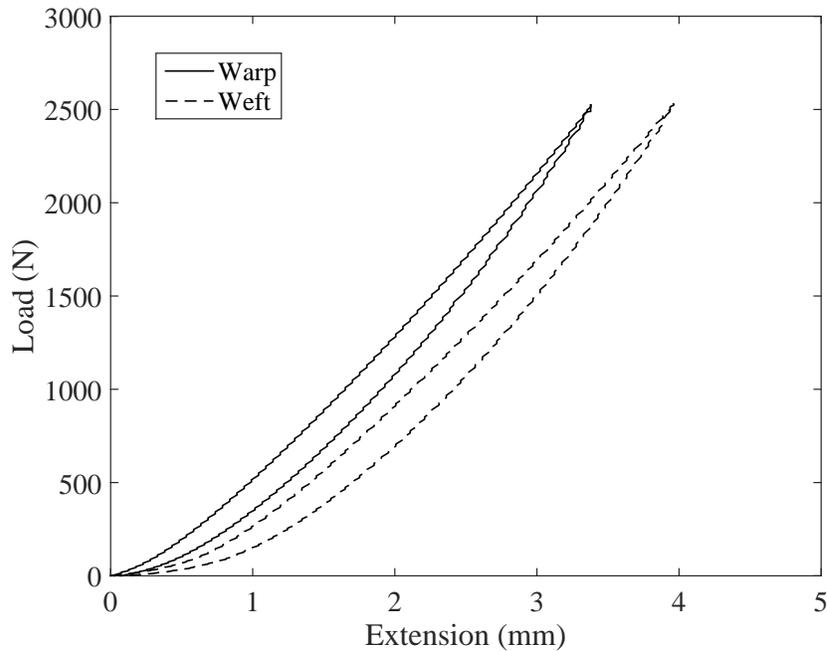
Figure B.4: 200 Denier Kevlar® Warp and Weft Uniaxial Tension Test - Shifted, Last Cycle

testing to the Green strain and PKII stress required by the formulation. The uniaxial test is carried out using a strip of fabric material with the initial length, l_0, and cross-section area, A_0. The measurements taken from the test are the grip handle displacement, d, and the force, $f(d)$, as a function of displacement. In lieu of calculating engineering stress and strain from force and displacement, Equations (86) and (87) can be used to go directly to Green strain and PKII stress. The stress-strain curve to be used in the material model is thus obtained by the following transformations to Green strain and PKII stress and shown in Figure B.5.

$$E_G = \frac{1}{2}\left(\frac{d}{l_0} + 1\right)^2 - \frac{1}{2} \tag{86}$$

$$S_{PKII} = \frac{f(d)}{A_0}\frac{l_0}{(l_0 + d)} \tag{87}$$

The ramp down or unloading portion of the curve is not being modeled and thus
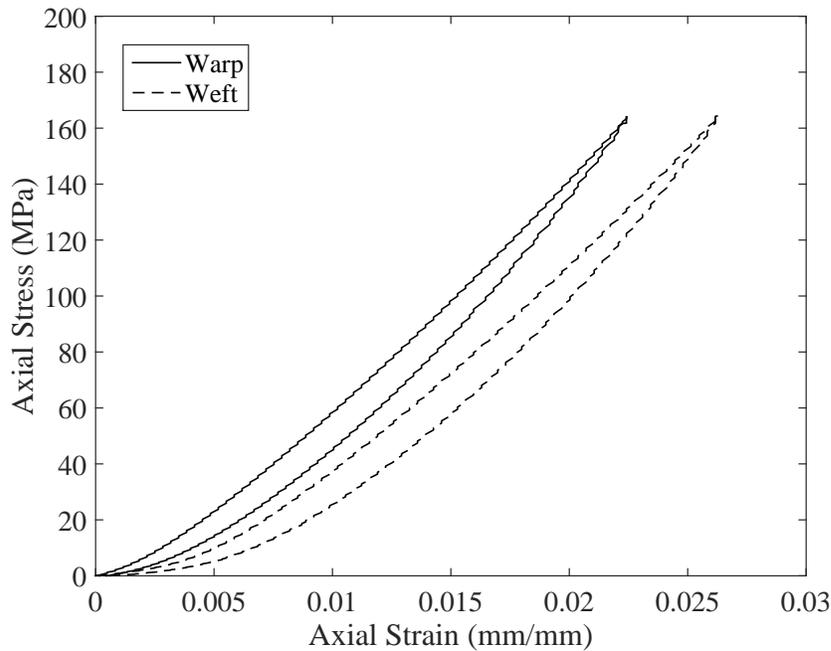
Figure B.5: 200 Denier Kevlar® Warp and Weft Uniaxial Stress Vs. Strain

Figure B.6 shows on the loading phase. A short region of lower stiffness followed by a linear stress-strain response is observed in the data. The initial region is attributed to mostly crimp interchange. As this phenomenon can be neglected for biaxial loaded cases, only the later linear portion is considered for the calculation of the warp and weft elastic moduli.

As shown in Figure B.7, only the linear portions of the stress-strain responses are utilized. When modeling this data using a linear curve fit, both the warp and weft curves have non-zero y-intercepts. The intercepts are neglected and the samples are assumed to have a linear response during all phases of loading. This is consistent with the work of Kabche et al [43].

The linear curves for the warp and weft direction curves produces slopes equal to 8409.8 MPa and 7673.4 MPa respectively. The mechanical behavior of the this material indicates that the Poisson's ration for a textile under uniaxial loading can be nonlinear and significantly greater than the value of 0.3 used by Tanner [15]. This
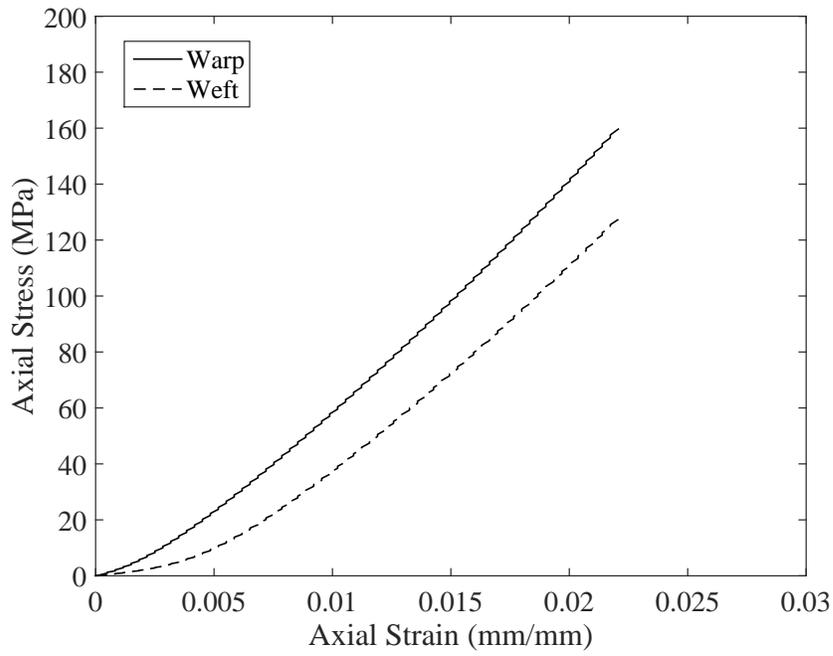
Figure B.6: 200 Denier Kevlar® Warp and Weft Uniaxial Stress Vs. Strain - Ramp Up
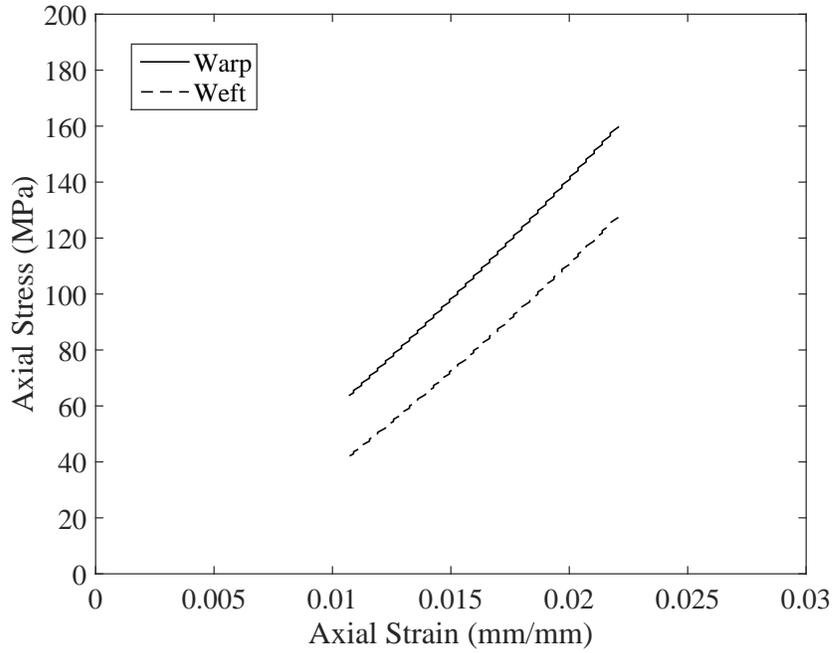
Figure B.7: 200 Denier Kevlar® Warp and Weft Uniaxial Stress Vs. Strain - Linear

property of textiles make it difficult to match Poisson's ratio using MAT_FABRIC. As discussed earlier, the lateral contraction in the fabric is caused by the crimp interchange seen at the low load levels in uniaxial tension. Since the crimp interchange can be neglected in cases of biaxial loading like that of air inflated fabric structures. Therefore, it is expected that $\nu_{ab} \approx 0$. For purposes of the nominal analysis, the value utilized is 0.3.

B.2.2 Trellis-Frame Test Data - Sample D

Only the tensile portion of the load history is utilized. Figure 29 provides reference to the equations that are utilized to convert load-deformation measurements into shear stress-strain data as shown in Figure B.8.

The force measured from the INSTRON load cell is converted into shear force in Equation (88) using the frame angle ϕ which is a function of the cross-head displacement and the frame kinematics.

$$F = \frac{F_{axial}}{2cos\phi} \tag{88}$$

In Equation (88), F is the resulting shear force. In Equation (89), L_{fabric} is the side length of the fabric sample. The shear stress near the center of the sample is calculated using Equation (89).

$$\tau = \frac{F}{L_{fabric}t} \tag{89}$$

The shear strain in Equation (90) is a function of the cross-head displacement and L_{frame} which is the side length of the trellis frame fixture.

$$\gamma = cos^{-1}\left[\frac{1}{\sqrt{2}} + \frac{\delta}{2L_{frame}}\right] \tag{90}$$

This is working is limited to modeling only the ramp up portion of loading. The unloading is neglected and thus can be remove from the stress-strain plot as shown in
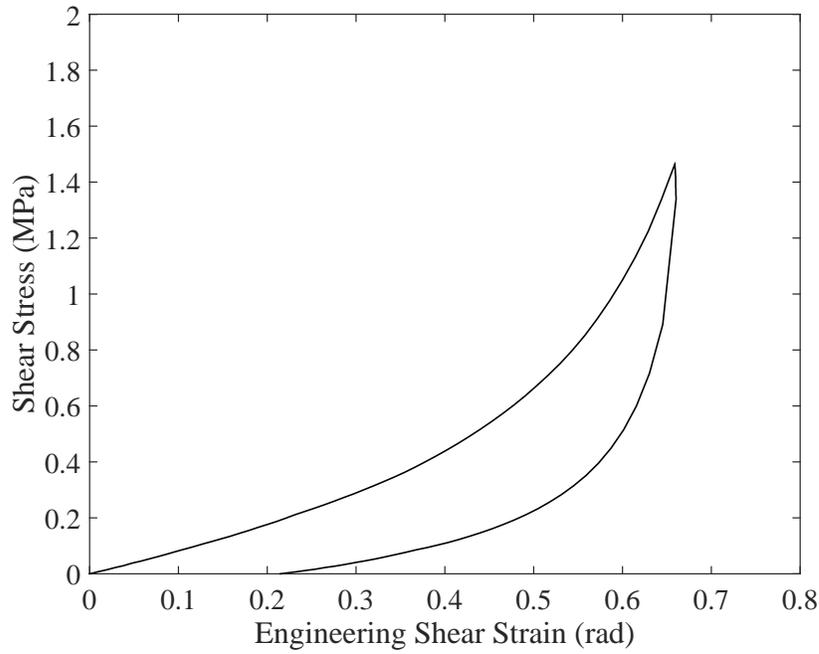
Figure B.8: 200 Denier Kevlar® Trellis Frame Stress Vs. Strain

Figure B.9. As discussed in Section 1.4.1, the results show trends that are consistent with the assumption that the initial shear response was dominated by the coating and with increased shearing, the behavior transitioned to that of an uncoated fabric. The initial region of low shear strain is modeled well using a linear curve fit with a slope of 0.898.

Table B.1 provides a summary of nominal set of material model input parameters obtained from experimental data.

Table B.1: Linear Elastic Orthotropic Material Properties

Property	Symbol	Value	Units
Density	ρ	1.101×10^{-9}	ton/mm^3
Thickness	h	0.202	mm
Young's Modulus, warp direction	E_a	8409.8	MPa
Young's Modulus, weft direction	E_b	7673.4	MPa
Poisson's Ratio	ν_{ab}	0.3	
Shear Modulus	G_{ab}	0.898	MPa

172

Figure B.9: 200 Denier Kevlar® Trellis Frame Stress Vs. Strain - Ramp Up

APPENDIX C

YARN GEOMETRY COMPUTATION

Microscopy is used to obtain cross-sectional images of a fabric cut along a particular plane. In order to restrict the movement of fibers during the cutting phase the fabric is often first cast in a resin. After allowing the resin to cure the composite structure can be cut along a desired plane. The surface is then usually polished to obtain a smooth surface. In the case of a composite that is already suspended in a matrix or coating, the casting and polishing steps can be skipped depending on the degree to which the yarns are restricted from moving. A microscope is used to take highly magnified images of the structure.
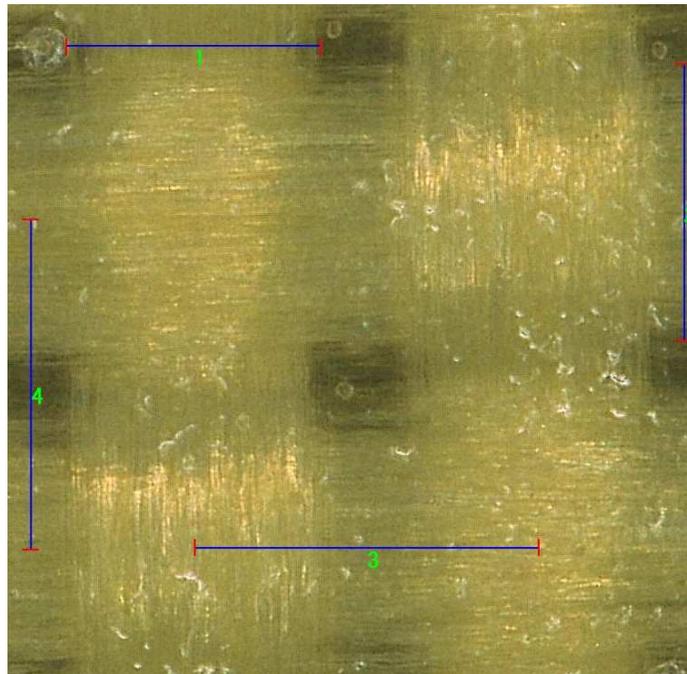
Figure C.1: Kevlar® 49 Face Image Taken Using Keyence Digital Microscope with 100 X Magnification

For this investigation, multiple samples were cut from a single roll of fabric. The

roll of fabric was provided by ILC Dover and was left over from a wind tunnel test campaign [2, 15]. The square samples were cut to be approximately 2 inches wide. The samples already contained a coating, so the cutting of the fabric did not significantly alter the architecture.

Figure C.2: Kevlar® 49 Cross-Section Image Taken Using Keyence Digital Microscope with 150 X Magnification

Each sample was placed under a microscope and multiple images were taken of the sample faces and cross-sections as shown in Figures C.1 and C.2. The measurements were taken manually at multiple locations.

Images from five samples were used to obtain measurements. Six measurements were taken per image. Measurements of the same characteristic were taken on the face and cross-section for comparison purposes. The measurements were averaged across the five samples. Table C.1 provides a summary of the measurements taken using the Keyence Digital Microscope. The table sorts the measurements in terms of the yarn width, w, yarn spacing, s, and yarn thickness, h. The subscripts w and f refer to the warp and weft directions respectively.

Table C.1: Optical Microscopy Image Measurements

Location	Type	Measurements (μm)				
		1	2	3	4	5
Face	w_w	522	596	551	543	524
Face	w_f	586	504	600	616	579
Face	s_w	727	710	745	714	718
Face	s_f	755	747	716	716	675
Cross Section	h	75	76	83	120	101
Cross Section	s	751	738	754	735	733

APPENDIX D

RELEVANT PUBLICATIONS

D.1 Journal Articles

1. **Hill, J.L.**, and Braun, R.D.; "Numerical Determination of Mechanical Properties for Flexible Material Systems," *Computers and Structures*, Submitted in March 2016.

2. **Hill, J.L.**, and Braun, R.D.; "Application of Parameter Identification to Current Experimental Mechanical Property Determination Methods," *Finite Elements in Analysis and Design*, (to be published).

3. **Hill, J.L.**, and Braun, R.D.; "Application of Parameter Identification to a Mesomechanical Material Model," *Computers and Structures*, (to be published).

D.2 Conference Papers

D.2.1 Published

1. Smith, B.P., **Hill, J.L.**, Clark, I.G., Braun, R.D.; "Oscillation of Supersonic Inflatable Aerodynamic Decelerators at Mars," AIAA 2011-2516, 21st AIAA Aerodynamic Decelerator Systems Technology Conference, Dublin, Ireland, May 2011.

2. **Hill, J.L.**, and Braun, R.D.; "Implementation of a Mesomechanical Material Model for IAD Fabrics within LS-DYNA," AIAA 2013-1367, 22nd AIAA Aerodynamic Decelerator Systems Technology Conference, Daytona Beach, FL, March 2013.

3. **Hill, J.L.**, and Braun, R.D.; "Modeling of Plain Woven Fabrics for Inflatable

Aerodynamic Decelerators," AIAA 2014-0631, 55th AIAA / ASMe / ASCE / AHS / SC Structures, Structural Dynamics, and Materials Conference, National Harbor, MD, January 2014.

4. **Hill, J.L.**; and Braun, R.D.; "Explicit Finite Element Analysis of Inflatable Braided Strapped Beams," AIAA 2015-0804, 23rd AIAA Aerodynamic Decelerator Systems Technology Conference, Daytona Beach, FL, April 2015.

D.2.2   Planned

1. **Hill, J.L.**, and Braun, R.D.; "Numerical Determination of Mechanical Properties for Flexible Material Systems," AIAA 2017-pending, 58th AIAA / ASMe / ASCE / AHS / SC Structures, Structural Dynamics, and Materials Conference, Gaylord, TX, January 2017.

REFERENCES

[1] Braun, R. D. and Manning, R. M., "Mars Exploration Entry, Descent, and Landing Challenges," *Journal of Spacecraft and Rockets*, Vol. 44, No. 2, March 2007, pp. 310–323.

[2] Clark, I. G., Hutchings, A. L., Tanner, C. L., and Braun, R. D., "Supersonic Inflatable Aerodynamic Decelerators for Use On Future Robotic Missions to Mars," *Journal of Spacecraft and Rockets*, Vol. 46, No. 2, March 2009, pp. 340–352.

[3] Coatta, D., Jurewicz, D. A., Tutt, B. A., Clark, I. G., and Rivellini, T., "Development and Testing of an 8m Isotensoid Supersonic Inflatable Aerodynamic Decelerator (SIAD)," American Institute of Aeronautics and Astronautics, 2013.

[4] Tanner, C., Cruz, J., and Braun, R., "Structural Verification and Modeling of a Tension Cone Inflatable Aerodynamic Decelerator," American Institute of Aeronautics and Astronautics, 2010.

[5] Lichodziejewski, D. L., Dillman, R. A., Jurewicz, D. A., Johnson, K., Cassell, A., and Tutt, B. A., "Ground and Flight Testing of a Stacked Torus Hypersonic Inflatable Aerodynamic Decelerator Configuration," American Institute of Aeronautics and Astronautics, 2013.

[6] Piascik, B., Vickers, J., Lowry, D., Scotti, S., Stewart, J., and Calomino, A., "Materials, Structures, Mechanical Systems, and Manufacturing," Tech. Rep. TA12, June 2015.

[7] Adler, M., Wright, M., Campbell, C., Clark, I., Engelund, W., and Rivellini, T., "Entry, Descent, and Landing Systems," Tech. Rep. TA9, June 2015.

[8] Smith, B. P., Tanner, C. L., Mahzari, M., Clark, I. G., Braun, R. D., and Cheatwood, F. M., "A Historical Review Of Inflatable Aerodynamic Decelerator Technology Development," IEEE, 2010, pp. 1–18.

[9] Houtz, N. E., "Optimization of Inflatable Drag Devices by Isotensoid Design," American Institute of Aeronautics and Astronautics, 1964.

[10] Barton, R. R., "Development of Attached Inflatable Decelerators for Supersonic Application," Tech. Rep. CR-66613, 1968.

[11] Faurote, G. L., "Design, Fabrication, and Static Testing of Attached Inflatable Decelerator (AID) Models," Tech. Rep. CR-111831, 1971.

[12] Mikulas Jr, C. M. W. and M, M., "Static Structural Tests of a 1.5-Meter-Diameter Fabric Attached Inflatable Declerator," Tech. Rep. TN D-6929, 1972.

[13] Anderson, M. S., Robinson, J. C., Bush, H. G., and Fralich, R. W., "A Tension Shell Structure for Application to Entry Vehicles," Tech. Rep. TN D-2675, 1965.

[14] Clark, I. G. and Braun, R. D., *Aerodynamic Design, Analysis, and Validation of a Supersonic Inflatable Decelerator*, Ph.D. thesis, May 2009.

[15] Tanner, C. L. and Braun, R. D., *Aeroelastic Analysis and Testing of Supersonic Inflatable Aerodynamic Decelerators*, Ph.D. thesis, May 2012.

[16] Brown, G., "Estimating Minimum Inflation Pressure for Inflatable Aerodynamic Decelerators," American Institute of Aeronautics and Astronautics, 2009.

[17] Hughes, S., Dillman, R., Starr, B., Stephan, R., Lindell, M., Player, C., and Cheatwood, F., "Inflatable Re-entry Vehicle Experiment (IRVE) Design Overview," American Institute of Aeronautics and Astronautics, 2005.

[18] Lindell, M., Hughes, S., Dixon, M., and Willey, C., "Structural Analysis and Testing of the Inflatable Re-Entry Vehicle Experiment (IRVE)," American Institute of Aeronautics and Astronautics, 2006.

[19] Samareh, J. A., "Estimating Mass of Inflatable Aerodynamic Decelerators Using Dimensionless Parameters," June 2011.

[20] Jurewicz, D., Brown, G., Gilles, B., Taylor, A., Sinclair, R., Tutt, B., Lichodziejewski, D., Kelley, C., and Hughes, S., "Design and Development of Inflatable Aeroshell Structure for IRVE-3," American Institute of Aeronautics and Astronautics, 2011.

[21] Leonard, R. W., McComb, H. G., Brooks, G. W., and States, U., "Structural Considerations Of Inflatable Reentry Vehicles," Tech. rep., 1960.

[22] Cruz, J. and Lingard, J., "Aerodynamic Decelerators for Planetary Exploration: Past, Present, and Future," American Institute of Aeronautics and Astronautics, 2006.

[23] Player, C., "The Program to Advance Inflatable Decelerators for Atmospheric Entry (PAIDAE)," June 2008.

[24] Rohrschneider, R., *Variable-Fidelity Hypersonic Aeroelastic Analysis of Thin-Film Ballutes for Aerocapture*, Ph.D. thesis, 2007.

[25] Lin, J. K., Shook, L. S., Ware, J. S., and Welch, J. V., "Flexible Material Systems Testing," Tech. rep., Nov. 2010.

[26] Hutchings, A., Braun, R., Masuyama, K., and Welch, J., "Experimental Determination of Material Properties for Inflatable Aeroshell Structures," American Institute of Aeronautics and Astronautics, 2009.

[27] Davids, W. G. and Clapp, J., "Behavior and Optimization of Hypersonic Inflatable Atmospheric Decelerator Devices for Spacecraft Re-Entry," Tech. rep., Oct. 2013.

[28] *Complete Textile Glossary*, Celanese Acetate LLC, 2001.

[29] Avallone, E. A., Baumeister III, T., and Sadegh, A. M., *Mark's Standard Handbook for Mechanical Engineers*, McGraw Hill, 2007.

[30] Hearle, J. W., *High Performance Fibres*, Elsevier, 2001.

[31] Cavallaro, P. V., Johnson, M. E., and Sadegh, A. M., "Mechanics Of Plain-Woven Fabrics For Inflated Structures," *Composite Structures*, Vol. 61, No. 4, Sept. 2003, pp. 375–393.

[32] Peirce, F. T., "The Geometry of Cloth Structure," *Journal of the Textile Institute Transactions*, Vol. 28, No. 3, 1937, pp. T45–T96.

[33] Hearle, J. W. S., Grosberg, P., and Backer, S., *Structural Mechanics Of Fibers, Yarns, And Fabrics*, Wiley-Interscience, 1969.

[34] Evans, J. T. and Gibson, A. G., "Composite Angle Ply Laminates And Netting Analysis," *Proceedings of the Royal Society A: Mathematical, Physical and Engineering Sciences*, Vol. 458, No. 2028, Dec. 2002, pp. 3079–3088.

[35] Brayley, K. E., "Structural Behavior of Externally Reinforced Inflated Fabric Arches and Beams," Tech. rep., June 2011.

[36] Bassett, R. J., Postle, R., and Pan, N., "Experimental methods for measuring fabric mechanical properties: A review and analysis," *Textile research journal*, Vol. 69, No. 11, 1999, pp. 866–875.

[37] Carr, W. W., Posey, J. E., and Tincher, W. C., "Frictional characteristics of apparel fabrics," *Textile research journal*, Vol. 58, No. 3, 1988, pp. 129–136.

[38] Asvadi, S. and Postle, R., "An analysis of fabric large strain shear behavior using linear viscoelasticity theory," *Textile research journal*, Vol. 64, No. 4, 1994, pp. 208–214.

[39] Murman, S. and Suresh, S., "Modeling Effective Stiffness Properties of IAD Fabrics," American Institute of Aeronautics and Astronautics, 2011.

[40] Welch, J. V., Wang, S., Blandino, J. R., and McEvoy, K., "Super Pressure Balloon Non-linear Structural Analysis and Correlation Using Photogrammetric Measurements," Aug. 2012, pp. 1–19.

[41] Farboodmanesh, S., Chen, J., Mead, J., and White, K., "Effect of Construction on Mechanical Behavior of Fabric Reinforced Rubber," *Rubber Chemistry and Technology*, Vol. 79, No. 2, 2006, pp. 199–216.

[42] Kilby, W. F., "Planar Stress-Strain Relationships in Woven Fabrics," *Journal of the Textile Institute Transactions*, Vol. 54, No. 1, 1963, pp. T9–T27.

[43] Kabche, J. P., Peterson, M. L., and Davids, W. G., "Effect of inflation pressure on the constitutive response of coated woven fabrics used in airbeams," *Composites Part B*, Vol. 42, No. 3, April 2011, pp. 526–537.

[44] Cavallaro, P. V., Sadegh, A. M., and Quigley, C. J., "Decrimping Behavior of Uncoated Plain-woven Fabrics Subjected to Combined Biaxial Tension and Shear Stresses," *Textile Research Journal*, Vol. 77, No. 6, June 2007, pp. 403–416.

[45] Peirce, F. T., "Geometrical Principles Applicable to the Design of Functional Fabrics," *Textile Research Journal*, Vol. 17, No. 3, March 1947, pp. 123–147.

[46] Grosberg, P., Leaf, G. A. V., and Park, B. J., "The Mechanical Properties of Woven Fabrics: Part VI: The Elastic Shear Modulus of Plain-Weave Fabrics ," *Textile Research Journal*, Vol. 38, No. 11, Nov. 1968, pp. 1085–1100.

[47] Choi, K.-J. and Ko, H.-S., "Research Problems in Clothing Simulation," *Comput. Aided Des.*, Vol. 37, No. 6, May 2005.

[48] Kawabata, S., Niwa, M., and Kawai, H., "The Finite-Deformation Theory Of Plain-Weave Fabrics Part I: The Biaxial-Deformation Theory," *Journal of the textile institute*, Vol. 64, No. 1, 1973, pp. 21–46.

[49] Kawabata, S., Niwa, M., and Kawai, H., "The Finite-Deformation Theory Of Plain-Weave Fabrics. Part II: The Uniaxial-Deformation Theory," *Journal of the textile institute*, Vol. 64, No. 2, 1973, pp. 47–61.

[50] Kawabata, S., Niwa, M., and Kawai, H., "The Finite-Deformation Theory Of Plain-Weave Fabrics. Part III: The Shear-Deformation Theory," *Journal of the textile institute*, Vol. 64, No. 2, 1973, pp. 62–85.

[51] Peng, X. Q. and Cao, J., "Numerical Determination Of Mechanical Elastic Constants Of Textile Composites," 2000, pp. 677–688.

[52] Komeili, M. and Milani, A. S., "Finite Element Modeling of Woven Fabric Composites at Meso-Level Under Combined Loading Modes," July 2011, pp. 1–14.

[53] Badel, P., Vidal-Sallé, E., and Boisse, P., "Computational Determination Of In-Plane Shear Mechanical Behaviour Of Textile Composite Reinforcements," *Computational Materials Science*, Vol. 40, No. 4, Oct. 2007, pp. 439–448.

[54] Komeili, M. and Milani, A. S., "The Effect Of Meso-Level Uncertainties On The Mechanical Response Of Woven Fabric Composites Under Axial Loading," *Computers and Structures*, Vol. 90-91, No. C, Jan. 2012, pp. 163–171.

[55] Breen, D. E., House, D. H., and Wozny, M. J., "A Particle-Based Model For Simulating The Draping Behavior Of Woven Cloth," *Textile Research Journal*, Vol. 64, No. 11, 1994, pp. 663–685.

[56] Boubaker, B. B., Haussy, B., and Ganghoffer, J.-F., "Consideration Of The Yarn - Yarn Interactions In Meso / Macro Discrete Model Of Fabric. Part I: Single Yarn Behaviour," *Mechanics Research Communications*, Vol. 34, No. 4, 2007, pp. 359–370.

[57] Boubaker, B. B., Haussy, B., and Ganghoffer, J.-F., "Consideration Of The Yarn - Yarn Interactions In Meso / Macro Discrete Model Of Fabric: Part II: Woven Fabric Under Uniaxial And Biaxial Extension," *Mechanics Research Communications*, Vol. 34, No. 4, 2007, pp. 371–378.

[58] Boubaker, B. B., Haussy, B., and Ganghoffer, J. F., "Discrete Models Of Woven Structures. Macroscopic Approach," *Composites Part B: Engineering*, Vol. 38, No. 4, 2007, pp. 498–505.

[59] Zhou, C., Jin, X., and Wang, C. C., "Shear Buckling And Dynamic Bending In Cloth Simulation," *Computer Animation and Virtual Worlds*, Vol. 19, No. 34, 2008, pp. 493–503.

[60] Peng, X. Q. and Cao, J., "A Continuum Mechanics-Based Non-Orthogonal Constitutive Model For Woven Composite Fabrics," *Composites Part A: Applied Science and Manufacturing*, Vol. 36, No. 6, June 2005, pp. 859–874.

[61] Ruíz, M. J. G. and González, L. Y. S., "Comparison Of Hyperelastic Material Models In The Analysis Of Fabrics," *International Journal of Clothing Science and Technology*, Vol. 18, No. 5, 2006, pp. 314–325.

[62] King, M. J., Jearanaisilawong, P., and Socrate, S., "A Continuum Constitutive Model For The Mechanical Behavior Of Woven Fabrics," *International Journal of Solids and Structures*, Vol. 42, No. 13, June 2005, pp. 3867–3896.

[63] Nadler, B., Papadopoulos, P., and Steigmann, D. J., "Multiscale Constitutive Modeling And Numerical Simulation Of Fabric Material," *International Journal of Solids and Structures*, Vol. 43, No. 2, 2006, pp. 206–221.

[64] Tabiei, A. and Ivanov, I., "Computational Micro-Mechanical Model Of Flexible Woven Fabric For Finite Element Impact Simulation," July 2002, pp. 1–26.

[65] Stander, N., Roux, W., Goel, T., Eggleston, T., Craig, K., and Basudhar, A., *LS-OPT User's manual*, June 2014.

[66] Hallquist, J. O., *LS-DYNA Theory Manual*, March 2006.

[67] Montgomery, D. C., *Design And Analysis Of Experiments*, John Wiley & Sons, 2008.

[68] Lenth, R. V., "Quick And Easy Analysis Of Unreplicated Factorials," *Technometrics*, Vol. 31, No. 4, 1989, pp. 469–473.

[69] Yao, L. and Sethares, W. A., "Nonlinear Parameter Estimation Via The Genetic Algorithm," *IEEE Transactions on signal processing*, Vol. 42, No. 4, 1994, pp. 927–935.

[70] Seibert, T., Lehn, J., Schwan, S., and Kollmann, F. G., "Identification Of Material Parameters For Inelastic Constitutive Models: Stochastic Simulations For The Analysis Of Deviations," *Continuum Mechanics and Thermodynamics*, Vol. 12, No. 2, 2000, pp. 95–120.

[71] Li, J. and Roberts, J. B., "Stochastic Structural System Identification: Part 1 - Mean Parameter Estimation," *Computational mechanics*, Vol. 24, No. 3, 1999, pp. 206–210.

[72] Li, J. and Roberts, J. B., "Stochastic Structural System Identification: Part 2 - Variance Parameter Estimation," *Computational mechanics*, Vol. 24, No. 3, 1999, pp. 211–215.

[73] Rikards, R. and Chate, A., "Identification Of Elastic Properties Of Composites By Method Of Planning Of Experiments," *Composite structures*, Vol. 42, No. 3, 1998, pp. 257–263.

[74] Rikards, R., Chate, A., Steinchen, W., Kessler, A., and Bledzki, A. K., "Method For Identification Of Elastic Properties Of Laminates Based On Experiment Design," *Composites Part B: Engineering*, Vol. 30, No. 3, 1999, pp. 279–289.

[75] Rikards, R., Chate, A., and Gailis, G., "Identification Of Elastic Properties Of Laminates Based On Experiment Design," *International Journal of Solids and Structures*, Vol. 38, No. 30, 2001, pp. 5097–5115.

[76] Kok, S., Beaudoin, A. J., and Tortorelli, D. A., "Parameter Estimation of Polycrystal Model through Identification Studies," 2000, pp. 210–219.

[77] Müllerschön, H., Franz, U., Münz, T., and Stander, N., "The Identification Of Rate-Dependent Material Properties In Foams Using Ls-Opt," 2001.

[78] Stander, N., Reichert, R., and Frank, T., "Optimization of Nonlinear Dynamical Problems Using Successive Linear Approximations in LS-OPT," 2000, p. 4798.

[79] Witowski, K. and Stander, N., "Parameter Identification of Hysteretic Models Using Partial Curve Mapping," 2012, p. 5580.

[80] Williams, R. W., "Measuring and modeling the anisotropic, nonlinear and hysteretic behavior of woven fabrics," June 2011, pp. 1–210.

[81] Karayaka, M. and Kurath, P., "Deformation and Failure Behavior of Woven Composite Laminates," Nov. 2007, pp. 1–11.

[82] De Borst, R., Crisfield, M. A., Remmers, J. J., and Verhoosel, C. V., *Nonlinear Finite Element Analysis Of Solids And Structures*, John Wiley & Sons, 2012.

[83] Taha, I., Abdin, Y., and Ebeid, S., "Comparison Of Picture Frame And Bias-Extension Tests For The Characterization Of Shear Behaviour In Natural Fibre Woven Fabrics," *Fibers and Polymers*, Vol. 14, No. 2, 2013, pp. 338–344.

[84] Data, M. M. P., "Overview of Silicone Rubber Materials," 0.

[85] McBride, T. and Chen, J., "Unit Cell Geometry in Plain Weave Fabrics During Shear Deformations," *Composites Science and Technology*, Vol. 57, 1997, pp. 345–351.

[86] Lin, H., Brown, L. P., and Long, A. C., "Modelling and Simulating Textile Structures Using TexGen," *Advanced Materials Research*, Vol. 331, Sept. 2011, pp. 44–47.

[87] Xia, Z., Zhou, C., Yong, Q., and Wang, X., "On Selection Of Repeated Unit Cell Model And Application Of Unified Periodic Boundary Conditions In Micro-Mechanical Analysis Of Composites," *International Journal of Solids and Structures*, Vol. 43, No. 2, Jan. 2006, pp. 266–278.

[88] Eschenauer, H., Koski, J., and Osyczka, A., *Multicriteria Design Optimization*, Springer Berlin Heidelberg, 1990.

[89] Vanderplaats, G. N., *Multidiscipline Design Optimization: Textbook*, Vanderplaats Research & Development, Incorporated, 2007.

[90] Kamat, M. P., "Structural Optimization: Status And Promise," *NASA STI/Recon Technical Report A*, Vol. 93, 1993, pp. 30075.

[91] Box, G. E. and Draper, N. R., *Empirical Model-Building And Response Surfaces*, Vol. 424, Wiley New York, 1987.

[92] Hajela, P. and Berke, L., "Neurobiological Computational Models In Structural Analysis And Design," *Computers & Structures*, Vol. 41, No. 4, 1991, pp. 657–667.

[93] Box, G. E. P. and Wilson, K. B., "On the Experimental Attainment of Optimum Conditions," *Journal of the Royal Statistical Society. Series B (Methodological)*, Vol. 13, No. 1, 1951, pp. 1–45.

[94] Myers, R. H., Montgomery, D. C., and Anderson-Cook, C. M., *Response Surface Methodology: Process And Product Optimization Using Designed Experiments*, Vol. 705, John Wiley & Sons, 2009.

[95] Stander, N. and Craig, K., "Response Surface And Sensitivity-Based Optimization In Ls-Opt: A Benchmark Study," 2002.

[96] Kurtaran, H., Eskandarian, A., Marzougui, D., and Bedewi, N. E., "Crash-worthiness Design Optimization Using Successive Response Surface Approximations," *Computational mechanics*, Vol. 29, No. 4-5, 2002, pp. 409–421.

[97] Roux, W. J., *Structural Optimization Using Response Surface Methodology*, Ph.D. thesis, May 1997.

[98] Roux, W. J., Stander, N., and Haftka, R. T., "Response Surface Approximations For Structural Optimization," *International Journal for Numerical Methods in Engineering*, Vol. 42, No. 3, 1998, pp. 517–534.

[99] Barthelemy, J. F. M. and Haftka, R. T., "Approximation concepts for optimum structural design — a review," *Structural optimization*, Vol. 5, No. 3, 0, pp. 129–144.

[100] Stander, N. and Craig, K. J., "On The Robustness Of A Simple Domain Reduction Scheme For SimulationBased Optimization," *Engineering Computations*, Vol. 19, No. 4, 2002, pp. 431–450.

[101] Lin, W. and Renaud, J. E., "A Comparative Study Of Trust Region Managed Approximate Optimization," *AIAAA paper*, Vol. 1499, 2001.

[102] Pérez, V. M., Renaud, J. E., and Gano, S. E., "Constructing Variable Fidelity Response Surface Approximations In The Usable Feasible Region," 2000, pp. 6–8.

[103] Alexandrov, N. M., Dennis Jr, J. E., Lewis, R. M., and Torczon, V., "A Trust-Region Framework For Managing The Use Of Approximation Models In Optimization," *Structural Optimization*, Vol. 15, No. 1, 1998, pp. 16–23.